DIGITAL PLASMONICS:
From concept to microscopy

DIGITAL PLASMONICS:
From concept to microscopy

ACADEMISCH PROEFSCHRIFT

ter verkrijging van de graad van doctor
aan de Universiteit van Amsterdam
op gezag van de Rector Magnificus
prof. dr. D. C. van den Boom
ten overstaan van een door het college voor promoties
ingestelde commissie,
in het openbaar te verdedigen in de Agnietenkapel
op 4 juli 2012, te 10.00 uur

door

Bergin Gjonaj

geboren te Tirana, Albanië

Promotiecommissie:

Promotor	Prof. Dr. A. Lagendijk
Promotor	Prof. Dr. L. Kuipers
Co-promotor	Dr. P. M. Johnson
Overige leden	Prof. Dr. C. Dainty
	Prof. Dr. A. P. Mosk
	Prof. Dr. A. Polman
	Prof. Dr. D. Bonn
	Prof. Dr. J. T. M. Walraven

Faculteit der Natuurwetenschappen, Wiskunde en Informatica

The work described in this thesis is part of the research program of the "Stichting Fundamenteel Onderzoek der Materie (FOM)", which is financially supported by the "Nederlandse Organisatie voor Wetenschappelijk Onderzoek (NWO)".

This work was carried out at the
FOM Institute for Atomic and Molecular Physics
Science Park 104, 1098 XG, Amsterdam,The Netherlands,
where a limited number of copies of this thesis is available
ISBN 9789077209622

Për tim at, sime më dhe sime motër,
përëndia ju bekoftë!

Paranimfen:
Ronald Ulbricht,
Eralda Tirana.

Ku rafsha mos u vrafsha

Qentë le të lehin, karvani të ecë përpara

CONTENTS

CHAPTER 1

INTRODUCTION

Controlling short wavelength plasmon waves via wavefront shaping techniques towards a plasmonic microscope is the goal of this thesis. In this chapter we will introduce the basic concepts underlying the work in this PhD thesis. We will introduce (1) Surface Plasmon Polaritons quasi-particles, the state of art in the field of plasmonics, as well as advantages and disadvantages these surface waves have to offer for high confinement of electromagnetic fields. We will also describe (2) wavefront shaping techniques used to achieve flexible and active control of the plasmonic fields. Finally, (3) microscopy techniques, which can benefit in resolution from a combination with plasmonics, will be introduced.

1.1 General Introduction

Since antiquity, controlling light has attracted the attention of the most brilliant minds of the time, from Archimedes [1] to Newton [2]. Even nowadays, controlling light at small length scales is one of the major research directions in physics and beyond [3, 4]. Due to the wave nature, the ability to control light is intrinsically limited by the diffraction limit which introduces a length scale limitation of the order of the wavelength of light. Below this length scale the spatial variations of the light field are not controllable with conventional optics such as mirrors, prisms,and lenses. Light is a powerful investigative tool in many areas of physics, biology, chemistry, medicine and so forth; but limited control of light fields inhibits investigation below the diffraction length scale. Controlling light beyond the diffraction limit is the essence of nanophotonics and an active area of research with large potential for applications.

With the development of Focused Ion Beam and Electron Beam Lithography, samples with features as small as the electron (or ion) wavelength became available. Typically the electron wavelength is orders of magnitude shorter than that of light, thus samples fabricated via electron lithography can have nanometer features: These nanostructured samples have features smaller than the diffraction limit of light. The availability of these nano-shaped samples gave rise to the field of "nanophotonics". The main goal of this expanding field is to control light beyond the diffraction limit using nano structured samples.

The field of nanophotonics can be divided in three main research areas very related to each other: (1) photonic crystals, (2) metamaterials, and (3) plasmonics. Spectacular results have been shown for photonic crystals [5, 6] as means of controlling the life times of molecules [7] and quantum dots [8, 9], or as optical-waveguide [10] circuitry with potential for lab-on-chip [11] and optical computation [12]. The field of metamaterials [13] introduced new fundamental concepts, such as perfect lenses [14, 15] using negative refraction [16, 17, 18, 19]. The potentiality of an invisibility cloak [20] using transformation optics [21, 22] and metamaterials [23] is being developed both theoretically and experimentally.

1.1.1 The field of plasmonics

One of the most active fields in nanophotonics is the control of light via Surface Plasmons [24, 25, 26]. Surface plasmons [27] are optically excited

oscillations of the free electrons at the surface of a metal. Because the electromagnetic field confinement achieved with these surface oscillations is tighter than the optical confinement, plasmonics offer control [28] of the electromagnetic radiation beyond the optical diffraction limit. The booming field of plasmonics allows for the excitation and the manipulation of surface plasmons via complex metallic nanostructures [29, 30]. With plasmonics, optical excitations are confined in nanoscale volumes which can be orders of magnitudes smaller than the standard optical confinement [31]. The effective light-matter interaction in these plasmonically confined volumes is strongly enhanced with profound implications in imaging, microscopy, sensing, nonlinear optics and lithography.

High confinement via plasmonics is achieved in two principal approaches: using localized surface plasmons, and using propagating surface plasmons.

Large research in plasmonics is directed towards the study of localized surface plasmons [32] in individual metal nanoparticles and particle assemblies [33]. The plasmonic harvesting of the optical energy within arrays of metal nanoparticles can lead to the formation of nanoscale hot spots [34] in which the intensity of light from an incident beam can be orders of magnitude more concentrated than by diffraction limited optics. This tight optical confinement has lead to a large improvement in techniques that use optical fields, such as surface enhanced Raman spectroscopy [35] where the Raman signal varies as the fourth power of the electric field. This improvement in Raman spectroscopy holds potential for applications in medical diagnostics. Similarly, metallic nanoparticles designed to selectively bond only to tumorous cells offer new hopes for cancer treatment [36]. When sick mice or human bodies infiltrated with these nanoparticles are exposed to light, the light energy will be strongly confined into the nanoparticles. The highly confined energy in the nanoparticles heats up the particles which will than burn the neighboring tumorous cells. Nonlinear processes, such as extreme-ultraviolet light from pulsed-laser high harmonic generation [37], also largely benefit from the field confinement offered by plasmonic nanoparticle arrays. The use of plasmonic nanoparticle arrays as efficient directional antennas for harvesting light, is giving rise to a new generation of thin film solar cells [38].

In the context of this thesis, propagating surface plasmons [39, 40] will be mainly discussed. When light couples to the electron oscillations on the surface of metallic films, propagating polariton waves are excited. These waves are the Surface Plasmon Polaritons (SPP). SPP waves propagating along metallic samples of precisely controlled material and geometry allow

for nanoscale wave guiding properties that cannot be realized with regular dielectrics. To be specific, extremely short wavelengths of the propagating plasmons can be achieved at optical frequencies. For example, it has been shown that for metal-insulator-metal waveguides [41], the wavelength of SPPs excited from visible light was reduced below 100 nm [42, 43, 44]. Thus for a fixed light frequency, the plasmonic wavelength can be up to an order of magnitude shorter than the optical wavelength. Provided a high degree of control of these SPP waves, their short wavelengths hold large potential for biomedical imaging [45], lithography [46] and optical data storage [47]. The short wavelengths of SPPs also enables new miniaturization prospectives in optical computation, for example by using plasmonic waveguides and nanowires for creating optical circuits [30] or the more complex optical transistor [48, 49]. Surface plasmons coupled to single photon sources provide new developing tools for quantum optics [50] and related applications. One of the latest proposed entries in propagating plasmonics is the substitution of the metal by graphene [51].

In the following sections we will provide a formalism for understanding propagating Surface Plasmon Polaritons on metal-dielectric interfaces. These propagating waves will be derived starting from the Maxwell's equation for a few interesting geometries, like single interface plasmons or double interface plasmons.

1.2 Single interface Surface Plasmon Polaritons

In this section we introduce surface plasmon polaritons propagating in a single metal-dielectric interface. The SPP wave propagates along the interface and its amplitude decays exponentially with the distance form the interface. We calculate here the propagation and decay constants of these waves for gold and silver films on two typical dielectric materials (air and glass).

1.2.1 Electromagnetic waves from Maxwell's equations

Surface plasmon polaritons are electromagnetic waves thus we will start with describing electromagnetic waves in the formalism of Maxwell's equations

and in absence of sources and currents.

$$\nabla \cdot \mathbf{B} = 0, \tag{1.1a}$$
$$\nabla \cdot \mathbf{E} = 0, \tag{1.1b}$$
$$\nabla \times \mathbf{B} = \varepsilon(\omega)\varepsilon_0\mu_0\frac{\partial \mathbf{E}}{\partial t}; \qquad \varepsilon_0\mu_0 \equiv \frac{1}{c^2}, \tag{1.1c}$$
$$\nabla \times \mathbf{E} = -\frac{\partial \mathbf{B}}{\partial t}. \tag{1.1d}$$

The speed of light is c while $\varepsilon(\omega)$ is the dielectric constant of the material under consideration relative to the vacuum. For the frequencies and structures we are interested in, the relative magnetic permeability is equal to unity and thus has been removed from the equations.

The above Maxwell's equations are partial differential equations in space and time. We can separate the variables and find the wave equation. The time dependency of the electric and magnetic fields is found to be $e^{i\omega t}$. We will thus look only to the spatial dependency of the fields

$$\nabla^2\mathbf{B}(\mathbf{r}) = \varepsilon(\omega){k_0}^2\mathbf{B}(\mathbf{r}), \tag{1.2a}$$
$$\mathbf{E}(\mathbf{r}) = \frac{-c^2}{i\omega\varepsilon(\omega)}\nabla \times \mathbf{B}(\mathbf{r}), \tag{1.2b}$$
$$\texttt{with:} \qquad k_0 \equiv \omega/c, \tag{1.2c}$$
$$\texttt{and:} \qquad \varepsilon(\omega) \equiv \varepsilon'(\omega) + i\varepsilon''(\omega) \equiv n^2(\omega). \tag{1.2d}$$

These equation are in their most general form with no boundary conditions imposed. We have imposed no constrictions on the dielectric constant or the refractive index n. To find the SPP fields we have to impose the structure of the dielectric constant and impose boundary conditions.

1.2.2 Piecewise dielectric function for the single interface

Surface Plasmon Polaritons are Transverse Magnetic (TM) waves at a metal-dielectric interface. In order to describe them we need to add this geometry to the wave equation described by Maxwell's equations. We divide the three-dimensional space into two regions separated by the plane of the interface, $z = 0$. For this single interface we consider a piecewise homogeneous dielectric function

$$\varepsilon(\omega) = \begin{cases} \varepsilon_1(\omega), & z \geq 0 \\ \varepsilon_2(\omega), & z < 0. \end{cases} \tag{1.3}$$

We can solve the wave equation separately for the to regions and later impose the continuity conditions for the electric and magnetic fields as well as momentum conservation in both regions.

1.2.3 SPPs as Transverse Magnetic waves

Here we will describe the solution for transverse magnetic (TM) waves which are bound to the interface $z = 0$ and exponentially decay with the distance from the interface in both regions. We assume the direction of propagation to be along the x axis. For TM waves this assumption implies that the magnetic field has a non-zero component only along the y axis. Because we are looking for waves confined to the plane of the interface, we require this magnetic field to decay exponentially with the distance from the interface in both regions. We can write

$$\mathbf{B}(\mathbf{r}) = \begin{cases} (0,1,0)N_1 \exp\left(ik_{x,1}x - k_{z,1}z\right), & z \geq 0 \\ \\ (0,1,0)N_2 \exp\left(ik_{x,2}x + k_{z,2}z\right), & z < 0. \end{cases} \tag{1.4}$$

Inserting this expression for the magnetic field into Maxwell's equation 1.2b yields the electric field

$$\mathbf{E}(\mathbf{r}) = \begin{cases} (k_{z,1}, 0, ik_{x,1})\frac{-c^2 N_1}{i\omega\varepsilon_1} \exp\left(ik_{x,1}x - k_{z,1}z\right), & z \geq 0 \\ \\ (-k_{z,2}, 0, ik_{x,2})\frac{-c^2 N_2}{i\omega\varepsilon_2} \exp\left(ik_{x,2}x + k_{z,2}z\right), & z < 0. \end{cases} \tag{1.5}$$

Thus the electric field has two components: E_x in the direction of the propagation and E_z in the decaying direction . The first component, E_x, is tangential to the interface and, apart from non-zero constants, we have $E_x \propto \varepsilon(\omega)^{-1}\partial B_y/\partial z$.

To determine the two normalization constants (N_1 and N_2), as well as the k-vectors along x and z, we use the continuity of the magnetic and electric fields along the interface (B_y and E_x). Regarding the normalization constants: the electric and magnetic fields are always determined except for a global normalization constant N. In specific cases it is possible to determine this global normalization constant, for example in experiments where a known light flux is incident (normalizing to the incident flux). In general the normalization problem can be very complicated, especially for continuous spectra [52].

From the equality of the tangential component of the magnetic field at the interface, $B_y(z = 0)$, we have

$$k_{x,1} = k_{x,2} \equiv K_S \equiv k_S + i/2L_S. \tag{1.6}$$

In the above equation we define the complex-valued SPP momentum K_S as well as its real part and imaginary parts. The real part of the SPP k-vector describes the plasmonic wave propagation and is related to the plasmon wavelength λ_S by $k_S = 2\pi/\lambda_S$. The imaginary part of the SPP k-vector describes losses in the metal as the wave propagates along the interface. The propagation length along z is exactly given by L_S.

Similarly to the magnetic field, we require also the equality of the tangential components of the electric field (E_x) in the two regions as they approach the plane of the interface. We find

$$\begin{cases} N_1 & = N_2 \\ -N_1 \dfrac{k_{z,1}}{\varepsilon_1} & = N_2 \dfrac{k_{z,2}}{\varepsilon_2}. \end{cases} \tag{1.7}$$

Or in matrix form

$$\begin{bmatrix} 1 & -1 \\ \dfrac{k_{z,1}}{\varepsilon_1} & \dfrac{k_{z,2}}{\varepsilon_2} \end{bmatrix} \begin{bmatrix} N_1 \\ N_2 \end{bmatrix} = \begin{bmatrix} 0 \\ 0 \end{bmatrix}. \tag{1.8}$$

This system of homogeneous equations has always the trivial solution ($N_i = 0; i = 1, 2$). Only when the determinant of the matrix is zero the system has a non trivial solution which corresponds to surface waves propagating along the interface

$$\frac{k_{z,1}}{\varepsilon_1} = -\frac{k_{z,2}}{\varepsilon_2}. \tag{1.9}$$

We interpret this equation based on the possible values of the two dielectric functions. To maintain realistic physical conditions, it is necessary to impose that $k_{z,i}$ is positive (real part), so as the wave decays exponentially in both regions. This condition is only satisfied in eq. (1.9) when the real part of dielectric constants for the two media have opposite signs. Such condition is satisfied for a metal-dielectric interface.

1.2.4 Dispersion relation for Single interface SPPs

To fully describe the surface plasmon propagation for a metal dielectric interface we have to determine the SPP wave vector K_S. We define the region $z > 0$, $z < 0$ as the metal and the dielectric, respectively, and substitute in the equations the index m, d for the upper region and the lower region, respectively. Finally we use the momentum conservation in both media to find the SPP k-vector.

$$\varepsilon_m k_0^2 = K_S^2 - k_{z,m}^2, \tag{1.10a}$$

$$\varepsilon_d k_0^2 = K_S^2 - k_{z,d}^2. \tag{1.10b}$$

The k-vector along y was taken to be zero, and the minus sign is due to the evanescent definition of the k-vector of k_z ($i^2 = -1$) By combining the above equations for the momentum conservation with eq. (1.9), we find the SPP dispersion relation

$$K_S(\omega) = k_0(\omega)\sqrt{\frac{\varepsilon_m(\omega)\varepsilon_d(\omega)}{\varepsilon_m(\omega) + \varepsilon_d(\omega)}}. \tag{1.11}$$

The dielectric constants of gold and silver, two metals that are commonly used in plasmonics, have been tabulated for different photon energies. We have used these tabulated values [53] to calculate the SPP dispersion relation for interfaces between gold and silver as metal combined with air ($n_a = 1$) and glass ($n_g = 1.5$) as dielectric. Results for these these two metal-dielectric interfaces are shown in Fig. 1.1.

Because we are interested in plasmonic microscopy, we also present the SPP dispersion relations as a function of the free space wavelength $\lambda_0 = 2\pi \cdot c/\omega$. These results, as well as the SPP propagation lengths, are shown in Fig. 1.2. From this figure, the beneficial properties of the plasmons for high field confinement can be quantitatively determined as the ratio between the SPP and the light wavelength (in vacuum and in the dielectric). The wavelength of silver-glass SPPs excited from blue light is as small as 200 nm: thus twice as small as the vacuum wavelength of light. Notice that as SPP wavelength decreases, so does their propagation length due to losses in the metal. A propagation length smaller than the SPP wavelength is unpractical for most applications.

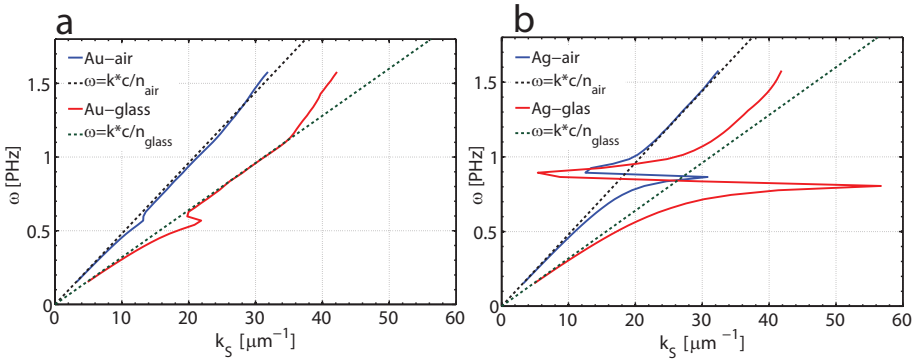

Figure 1.1: *SPP dispersion relations. (a) Dispersion relation for Au. (b) Dispersion relation for Ag. The dashed lines are the photon light lines, $\omega = n \cdot ck$. Refractive indices of Au and Ag taken from reference [53].*

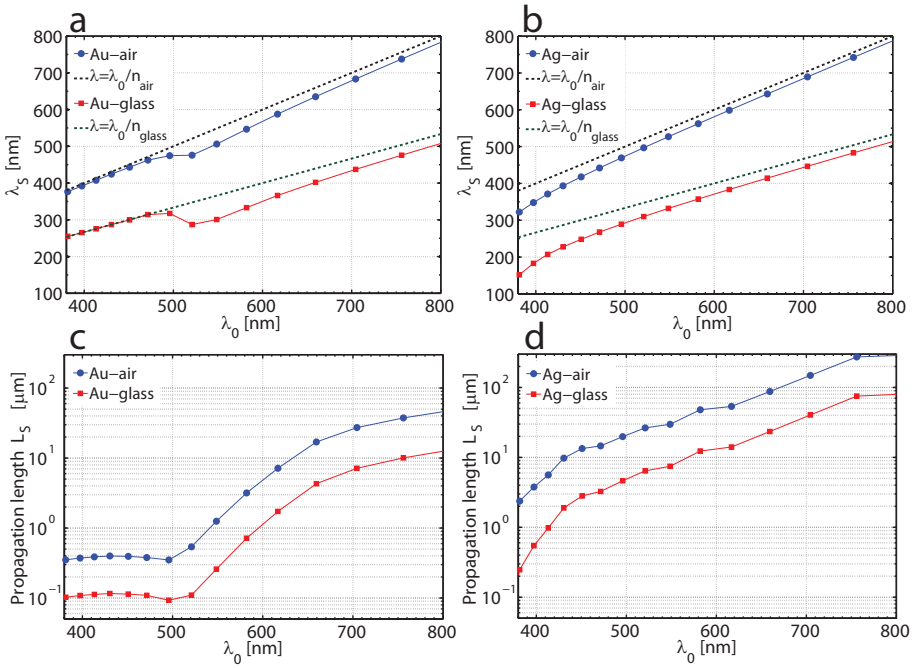

Figure 1.2: *Alternative presentation of the $\omega - k$ dispersion relations of Fig.1.1. The SPP wavelength plotted as function of the vacuum wavelength λ_0. (a)-(b) Dispersion relation of Au (a) and Ag (b). (c) and (d) Propagation length of SPPs for the two metals. Material properties for the metals taken from reference [53].*

1.2.5 Lack of Transverse Electric SPP waves

We have defined SPPs as transverse magnetic (TM) polarized waves bound to metal-dielectric interfaces. Here we prove the definition correct by demonstrating that no bound transverse electric (TE) waves can be excited. The calculation is very similar to the TM case, but the electric and magnetic field exchanged. The dielectric function in the two regions is given by Eq. (1.3), as for the TM case.

For a TE polarized wave that propagates in the interface, we suppose an in-plane electric field along the y axis. This electric field decays exponentially in both regions as a function of the distance from the interface.

$$\mathbf{E}(\mathbf{r}) = \begin{cases} (0,1,0)N_1 \exp\left(ik_{x,1}x - k_{z,1}z\right), & z \geq 0 \\ \\ (0,1,0)N_2 \exp\left(ik_{x,2}x + k_{z,2}z\right), & z < 0 \end{cases} \tag{1.12}$$

Similarly as for the TM waves, the magnetic field is determined using Maxwell's equations.

$$\mathbf{B}(\mathbf{r}) = \begin{cases} (k_{z,1}, 0, ik_{x,1})\frac{cN_1}{i\omega} \exp\left(ik_{x,1}x - k_{z,1}z\right), & z \geq 0 \\ \\ (-k_{z,2}, 0, ik_{x,2})\frac{cN_2}{i\omega} \exp\left(ik_{x,2}x + k_{z,2}z\right), & z < 0 \end{cases} \tag{1.13}$$

The crucial difference between the TM and TE polarized waves is the absence of the dielectric constant in equation eq. 1.13 (compared to eq. 1.5). This absence has major consequences when we apply the continuity condition to the electric and magnetic field and require realistic solutions (exponentially decaying with the distance from the interface).

The continuity of the magnetic field is equivalent to the continuity of $\partial E_y/\partial z$. From the continuity of the tangential components of the electric and magnetic fields, a set of homogeneous equations in the normalization constants (N_i) is derived.

$$\begin{bmatrix} 1 & -1 \\ k_{z,1} & k_{z,2} \end{bmatrix} \begin{bmatrix} N_1 \\ N_2 \end{bmatrix} = \begin{bmatrix} 0 \\ 0 \end{bmatrix} \tag{1.14}$$

As for the TM case, apart from the trivial solution of no fields $N_i = 0$, other solutions are possible when the determinant of the above matrix is zero. For the TE case this yields

$$k_{z,1} = -k_{z,2}. \tag{1.15}$$

By a direct comparison with the TM case of eq. (1.9) we notice that the dielectric functions in the two regions are not part of the TE equation. The TE solution of eq. (1.15) is physically unacceptable because the fields must decay exponentially with the distance from the interface, which dictates that both $k_{z,1}$ and $k_{z,2}$ must be positive; a condition that cannot be satisfied simultaneously with eq. (1.15). Thus the only acceptable solution is the trivial solution $N_i = 0$. Hence no bound TE SPP waves do exist.

1.3 Double interface Surface Plasmon Polaritons

In this section we show that a geometry with two metal-dielectric interfaces can achieve higher field confinement (shorter wavelength) than the single metal-dielectric interface. The dispersion relations are described for a general three layer structure . We will focus our attention on the Metal-Insulator-Metal (MIM) structures. Our starting point is the piecewise dielectric constant of the structure, with d the thickness of the insulator

$$\varepsilon(\omega) = \begin{cases} \varepsilon_1(\omega), & z \geq d \\ \varepsilon_2(\omega), & 0 < z < d \\ \varepsilon_3(\omega), & z \leq 0. \end{cases} \tag{1.16}$$

As for the single interface we are looking for evanescent (TM) solutions to the wave equation propagating along x. The magnetic field in the three regions is given by

$$\mathbf{B}(\mathbf{r}) = (0,1,0)e^{iK_S x} \begin{cases} N_1 \exp\left[-k_{z,1} \cdot (z-d)\right], & z \geq d \\ N_2 \exp\left(-k_{z,2} z\right) + N_3 \exp\left[k_{z,2} \cdot (z-d)\right], & 0 < z < d \\ N_4 \exp\left(k_{z,3} z\right), & z \leq 0. \end{cases} \tag{1.17}$$

The k-vectors are defined as for the single interface and we have assumed the propagation of a SPP wave with k-vector $K_S \equiv k_{x,i}$. We impose the continuity of the tangential components of the magnetic (H_y) and electric (E_x) fields at both interfaces ($z = 0$ and $z = d$). From the single interface we noticed that the continuity of the tangential electric filed was equivalent to the continuity of $\varepsilon^{-1}\partial H_y(z)/\partial z$. These conditions result in a system of four equations for the four unknown N_i's

$$\begin{cases} N_1 & = N_2 \exp(-k_{z,2}d) + N_3 \\ -N_1 \frac{k_{z,1}}{\varepsilon_1} & = -N_2 \frac{k_{z,2}}{\varepsilon_2} \exp(-k_{z,2}d) + N_3 \frac{k_{z,2}}{\varepsilon_2} \\ N_4 & = N_2 + N_3 \exp(-k_{z,2}d) \\ N_4 \frac{k_{z,3}}{\varepsilon_3} & = -N_2 \frac{k_{z,2}}{\varepsilon_2} + N_3 \frac{k_{z,2}}{\varepsilon_2} \exp(-k_{z,2}d). \end{cases} \tag{1.18}$$

The system has a non trivial solution ($N_i \neq 0$) only if the determinant of the associated matrix is zero. For simplicity we denoted $e^{-k_{z,2}d}$ with A

$$\det \begin{bmatrix} -1 & A & 1 & 0 \\ \frac{k_{z,1}}{\varepsilon_1} & -\frac{k_{z,2}}{\varepsilon_2}A & \frac{k_{z,2}}{\varepsilon_2} & 0 \\ 0 & 1 & A & -1 \\ 0 & -\frac{k_{z,2}}{\varepsilon_2} & \frac{k_{z,2}}{\varepsilon_2}A & -\frac{k_{z,3}}{\varepsilon_3} \end{bmatrix} = 0. \tag{1.19}$$

By calculating the determinant above we find the condition for the dual interface SPP waves. The value of the SPP k-vector (K_S) is included in the expressions for all the other k-vectors due to the momentum conservation ($k_{z,i}^2 = K_S^2 - \varepsilon_i k_0^2$) in the three different spatial regions.

$$\left(\frac{k_{z,1}}{\varepsilon_1} + \frac{k_{z,2}}{\varepsilon_2}\right)\left(\frac{k_{z,3}}{\varepsilon_3} + \frac{k_{z,2}}{\varepsilon_2}\right) = \left(\frac{k_{z,1}}{\varepsilon_1} - \frac{k_{z,2}}{\varepsilon_2}\right)\left(\frac{k_{z,3}}{\varepsilon_3} - \frac{k_{z,2}}{\varepsilon_2}\right) e^{-2k_{z,2}d}. \tag{1.20}$$

Eq. 1.20 is the dispersion relation for dual interface SPPs. The value of the SPP k-vector (K_S) is included in the expressions for all of the other k-vectors due to the momentum conservation ($k_{z,i}^2 = K_S^2 - \varepsilon_i k_0^2$) in the three different spatial regions. In contrast with the single interface case, the dual interface condition of eq. (1.20) cannot be solved analytically. Nevertheless, we immediately notice that for d tending to infinity the right part of eq. (1.20) becomes zero and we find two solutions given by the single interface dispersion relation. As a result, for large thicknesses there will be two SPP modes, one for each interface. When the thickness decreases these two modes will start to couple to each other and will hybridize into new SPP modes (MIM SPPs) of much shorter wavelength.

1.3.1 SPP dispersion relation for a MIM waveguide

We calculate the dispersion relations of surface plasmons propagating in a metal-insulator-metal (MIM) waveguide by solving eq. 1.20 graphically. We

use the same metal in the two periphery regions, and thus we substitute the index m in both regions. Similarly we use the index d for the dielectric core in the central region. We rewrite condition (1.20) for the MIM structure

$$\left(\frac{k_{z,m}}{\varepsilon_m}+\frac{k_{z,d}}{\varepsilon_d}\right)=\pm\left(\frac{k_{z,m}}{\varepsilon_m}-\frac{k_{z,d}}{\varepsilon_d}\right)e^{-k_{z,d}d}. \tag{1.21}$$

The +(-) solution due to the square root represent a symmetric (antisymmetric) magnetic field distribution relative to the plane $z = d/2$. With a bit of algebra and remembering that $\tanh(x/2) = \coth(x/2)^{-1} = \frac{e^x-1}{e^x+1}$ we write

$$\frac{k_{z,m}}{\varepsilon_m}\cdot\frac{k_{z,d}}{\varepsilon_d}=-\tanh\left(-\frac{1}{2}k_{z,d}d\right), \tag{1.22a}$$

$$\frac{k_{z,m}}{\varepsilon_m}\cdot\frac{k_{z,d}}{\varepsilon_d}=-\coth\left(-\frac{1}{2}k_{z,d}d\right). \tag{1.22b}$$

The equations can be solved graphically as a function of the propagating SPP k-vector K_S. Again, the propagating SPP k-vector is included implicitly in eq. (1.22a) via the momentum conservation in the various regions, $\varepsilon_i k_0^2 = K_S^2 - k_i^2$, where the index i indicates either metal (m) or dielectric (d).

For the MIM waveguide plasmons, only eq. (1.22a) has solutions. These solutions are shown in Fig. 1.3 for gold and silver at a double interface with a planar silicon nitrate dielectric core ($n = 2$). Alternatively, in Fig. 1.4, the same solutions are shown as a function of the SPP and vacuum wavelengths. The MIM waveguide provides shorter wavelengths (higher confinement) of the SPP waves as the dielectric thickness d decreases.

Compared to the single interface plasmons (infinite thickness data of Fig. 1.4), shorter SPP wavelengths can be achieved. For a fixed photon frequency and for reasonable propagation lengths of the plasmons, the MIM SPP wavelength is up to a factor three shorter than the wavelength of light in the dielectric (given by the light line in the dielectric). Therefore, MIM plasmons with a given dielectric middle layer could resolve microscopic objects with nearly triple the resolution of a solid immersion lens composed of the same dielectric.

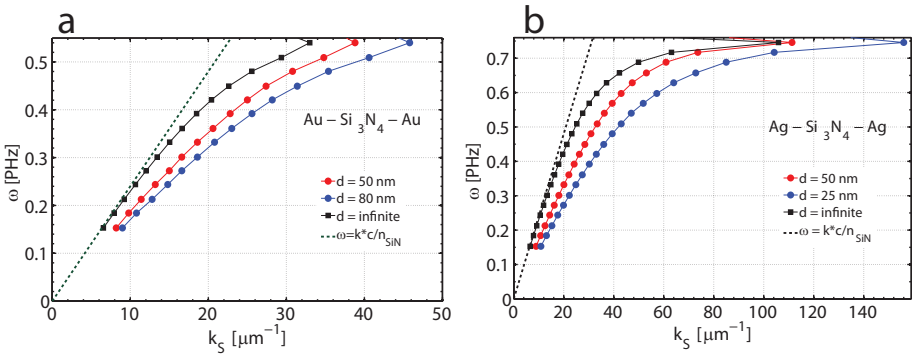

Figure 1.3: *MIM SPP dispersion relations. (a) Dispersion relation for Au. (b) Dispersion relation for Ag. Dashed lines are the photon light lines in Si_3N_4. Refractive indexes of Au and Ag taken from reference [53].*

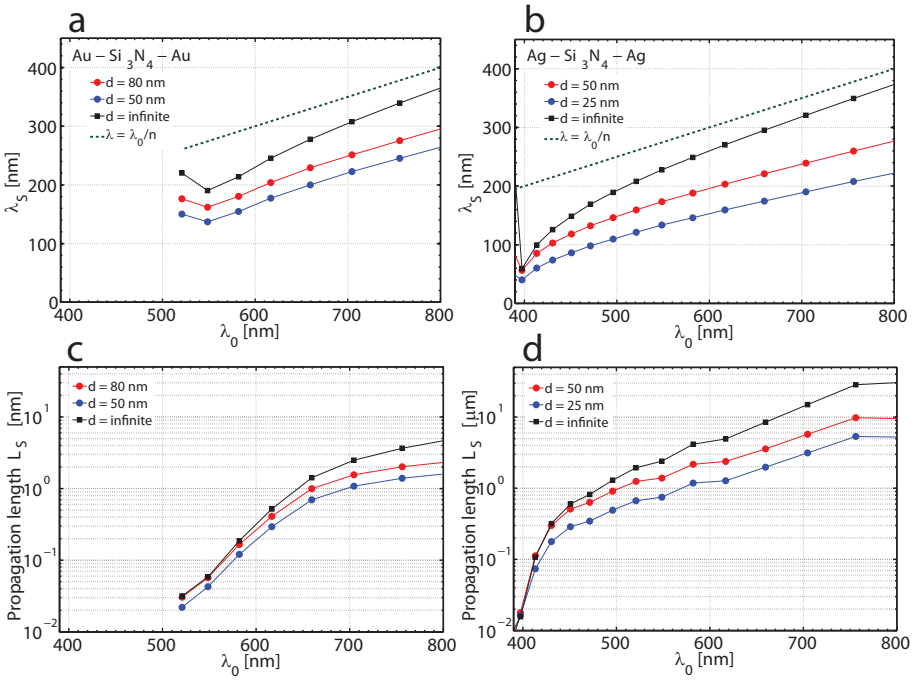

Figure 1.4: *Alternative presentation of the $\omega - k$ dispersion relations of Fig. 1.3. The SPPs wavelength is plotted as function of the vacuum wavelength λ_0. (a)-(b) Dispersion relation for a Au-SiN-Au (a) and Ag-SiN-Ag (b). (c) and (d) Propagation length of SPPs. Material properties for the metals taken from reference [53].*

1.4 Microscopy techniques benefiting from plasmonics

We have shown in the previous section the potential of plasmonics for high field confinement. The confinement is due to a much shorter SPP wavelength compared to either the free space wavelength or the wavelength in the dielectric. This short wavelength offers high potential for microscopy because the resolution of a microscope is inversely proportional to the wavelength. Here we briefly describe two microscopy techniques, widely used in biology, that could perform better with plasmonic illumination than with light.

1.4.1 Total internal reflection microscopy (TIRM)

For a variety of biological systems it is important to distinguish the surface information from the core. For living cells, for example, most of the interaction with the external environment is happening at the surface. The cell's dynamics are based on the information it receives from the surface. Total internal reflection microscopy is a widely used technique for surface-only investigation.

Total internal reflection microscopy (TIRM) is based on evanescent waves. These waves have a purely imaginary component of the k-vector, thus they decay exponentially along that direction. The standard method to generate these waves is via total internal reflection. When light impinges on the interface between two dielectrics with an angle above the critical angle, all light is reflected back (total reflection); except for an evanescent tail which decays exponentially with distance from the interface. If a scatterer or a fluorescent molecule is placed in the vicinity of the interface, then the scatterer will be exited only via the evanescent tail of the electric field. When the scatterer to interface distance is much larger than the decay constant of the evanescent wave, no electric field is present in proximity of the scatterer which therefore cannot be excited. Only scatterers very close to the surface will feel the presence of the evanescent field. This fact allows for surface investigation. The resolution along the direction of the evanescent decay (axial resolution) is provided not by the diffraction limit (wavelength dependent), but by the evanescent tail. Only a thin slice of the biological sample within the decay constant is imaged, as shown in Fig. 1.5a. Nevertheless, the lateral resolution along the surface is still determined by the diffraction limit.

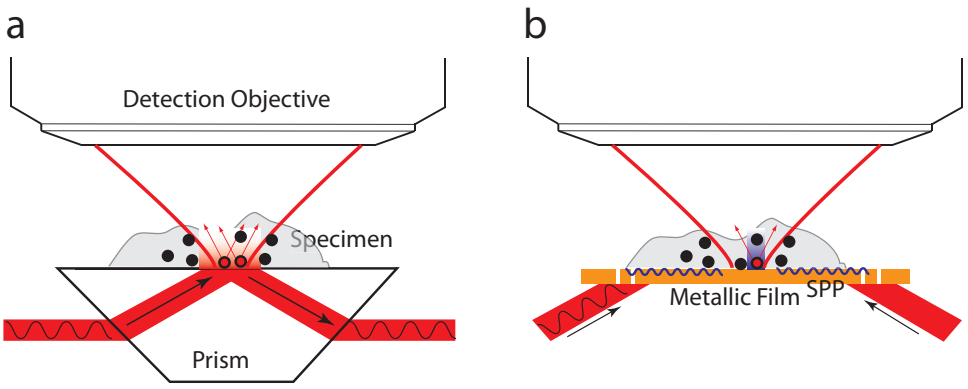

Figure 1.5: *Principle of total internal reflection microscopy (TIRM). (a) Optical TIRM. Light above the critical angle is totally reflected except for an evanescent wave. This evanescent wave is scattered only by particles next to the surface. The scattered light is collected by the objective. Because of the detection diffraction limit two nearby particles (red circles) are unresolved. (b) Plasmonic TIRM is achieved via focused plasmonic wave excitation. The in-plane resolution is determined by plasmonic diffraction limit of the excitation (shown in blue). Two nearby scatterers are resolved.*

1.4.2 Plasmonic contribution to TIRM

Plasmonic waves are surface waves that decay exponentially with the distance from a metal-dielectric (or more complicated multilayer) interfaces. On one hand, plasmonics offers the same evanescent axial resolution for TIRM as evanescent light waves (thus they can achieve surface only imaging). On the other hand, SPPs TIRM offers an additional advantage: an increased lateral resolution due to shorter SPP wavelengths compared to light in the dielectric.

The principle of plasmonic TIRM is shown in Fig. 1.5b where the focused evanescent plasmonic field exciting the scatterer is shown in blue. Compared to optical TIRM (Fig. 1.5a) in which two optically excited scatterers (in red) are indistinguishable because of the optical diffraction limit, plasmonic fields focused below optical diffraction can distinguishably excite each scatterer separately. The resolution is determined by the excitation (plasmonic diffraction limit) and not by the detection optics. Nevertheless, to achieve in-plane resolution enhancement, the plasmonic excitation must be tightly focused by using an SPP lens. The creation of such a plasmonic

lens will be one of the goals of this thesis.

1.4.3 Structured Illumination Microscopy (SIM)

We introduce the principles of structured illumination microscopy (SIM), a technique that achieves a resolution two times better than that given by the optical diffraction limit [54, 55]. The core ingredient of structured illumination microscopy is the structured illumination: instead of a wide field illumination a sinusoidal pattern is used. In k-vector space, this sinusoidal pattern will carry additional information. Let the sample spatial distribution be $s(\mathbf{r})$, with $\mathbf{r}$ a two-dimensional vector on the surface of the sample. In SIM such a sample is illuminated with a periodic intensity pattern $f(\mathbf{r})$ along $\mathbf{k}_f$ created by two counter propagating waves, of which the relative phase ϕ determines the positions of the maxima of intensity

$$f(\mathbf{r}) \equiv 1 + \cos(\mathbf{k}_f \cdot \mathbf{r} + \phi) = 1 + \frac{1}{2}\left[e^{i(\mathbf{k}_f \cdot \mathbf{r} + \phi)} + e^{-i(\mathbf{k}_f \cdot \mathbf{r} + \phi)}\right]. \tag{1.23}$$

When an image of the sample is taken with a lens of which point-spread function (psf) is $h(\mathbf{r})$, the measured spatial intensity $I(\mathbf{r})$ and its Fourier transform $\widetilde{I}(\mathbf{k})$ are

$$I(\mathbf{r}) = [f(\mathbf{r})s(\mathbf{r})] \otimes h(\mathbf{r}), \tag{1.24a}$$

$$\widetilde{I}(\mathbf{k}) = F\left[f(\mathbf{r})s(\mathbf{r})\right] \cdot \widetilde{h}(\mathbf{k}) = \tag{1.24b}$$

$$= \left[\widetilde{s}(\mathbf{k}) + \frac{e^{-i\phi}}{2}\widetilde{s}(\mathbf{k}+\mathbf{k}_f) + \frac{e^{i\phi}}{2}\widetilde{s}(\mathbf{k}-\mathbf{k}_f)\right] \cdot \widetilde{h}(\mathbf{k}). \tag{1.24c}$$

The Fourier transform F has been calculated using eq. (1.23) and by notating with $\widetilde{s}$ and $\widetilde{h}$ the transforms of s and h respectively. The psf (h) is assumed as a gaussian with FWHM equal to the diffraction limit resolution. Thus its Fourier transform $\widetilde{h}$ is also a gaussian with FWHM (k_h) which value is inversely proportional to the diffraction limited resolution. For simplicity we further assume that $\widetilde{h}$ is a circle with diameter k_h.

In the intensity spectrum of eq. (1.24c) we notice three contributions: a central one and two contributions shifted by $\pm\mathbf{k}_f$. The central one $[\widetilde{s}(\mathbf{k})\widetilde{h}(\mathbf{k})]$ is the sample spectra truncated to k_h because of the limited resolution. The two shifted contributions are the the sample spectrum shifted by $\pm\mathbf{k}_f$. Because of these shifts due to the sinusoidal illumination, part of the sample spectra above the limiting k_h fall now into the observable detection limit

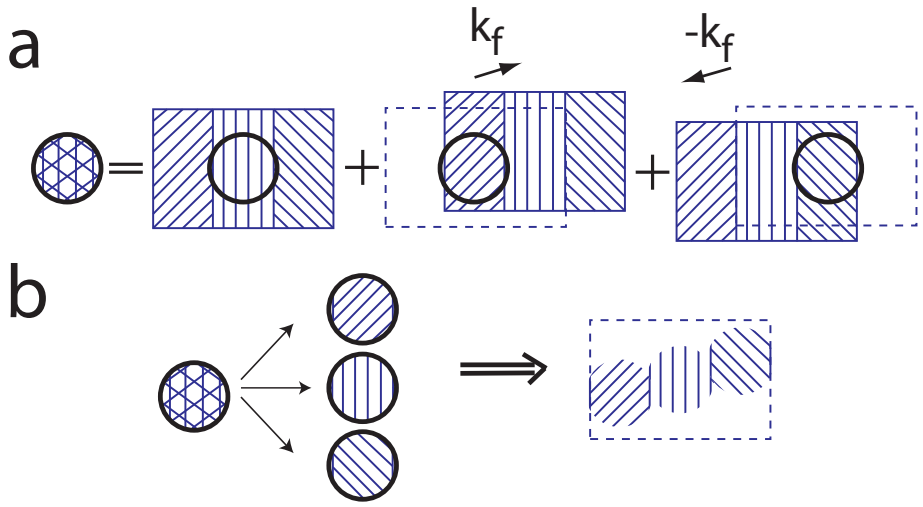

Figure 1.6: *Effect of the structured illumination in k-vector space. The rectangle represents the sample k-vectors. The sample separation in three areas is simply illustrative. (a) The small circles are the Fourier transform of the point spread function. Because of the sinusoidal illumination, the Fourier transform of the recorded intensity is the sum of three different components. Together with the wide-field information (vertical stripes), information from two more areas of the sample (diagonal stripes), is mixed in the recorded image. (b) If the three information components recorded in the image are properly separated, they can be used to increase the resolution.*

circle. In principle, if one combines the information contained in these three contributions, an imaging resolution can be obtained that is better than the diffraction limit. Nevertheless the three contributions are overlapped with each other in the measured image as shown in Fig. 1.6a. As a result a single image is not sufficient to separate the three contributions: three images are required. The location of the sinusoidal illumination (not the direction) can be changed by varying the phase ϕ. Taking pictures for three different phases of the structured illumination ϕ_1, ϕ_2, ϕ_3 we obtain

$$\begin{bmatrix} \widetilde{I}_1(\mathbf{k}) \\ \widetilde{I}_2(\mathbf{k}) \\ \widetilde{I}_3(\mathbf{k}) \end{bmatrix} = \frac{\widetilde{h}(\mathbf{k})}{2} \begin{bmatrix} 2 & e^{-i\phi_1} & e^{i\phi_1} \\ 2 & e^{-i\phi_2} & e^{i\phi_2} \\ 2 & e^{-i\phi_3} & e^{i\phi_3} \end{bmatrix} \cdot \begin{bmatrix} \widetilde{s}(\mathbf{k}) \\ \widetilde{s}(\mathbf{k}+\mathbf{k}_f) \\ \widetilde{s}(\mathbf{k}-\mathbf{k}_f) \end{bmatrix}. \tag{1.25}$$

By inverting the system and solving it we can separate the three contributions. Once the three contributions are separated, the two shifted contri-

butions have to be shifted back to their original position at $\pm\mathbf{k}_f$, respectively. To obtain an isotropically improved resolution, the above procedure is repeated for few other directions, for example by keeping the module of k_f constant but changing its direction. In general 12 images suffice: four directions, with three different phases for each direction. The improvement of the point-spread function in k-vector space is shown in Fig. 1.7a-b. The psf achieved via SIM, shown as the black circle in Fig. 1.7b, is larger than the original psf of Fig. 1.7a. In the real space ($\mathbf{r}$) this larger SIM psf yields improved resolution.

At best, the resolution can improve by a factor two: because the structured illumination is created by the same optics, the magnitude of k_f cannot be larger than $k_h/2$. In other words, the momentum of the fringes has to be within the circle given by the diffraction limit. The best configuration is achieved when the structured illumination pattern is created with the maximally allowed resolution by the optics we have that $k_f = k_h/2$. The new point spread function has now a diameter of $2k_h$, as shown in Fig. 1.7b. Thus by back Fourier transforming in real space, the resolution is two times better than the diffraction limit.

1.4.4 Plasmonic contribution to SIM

When the sinusoidal pattern is optically created, each fringe has to be resolved from the others (the minima yields zero intensity) for SIM to work. This criteria implies that the fringe periodicity cannot be made smaller than twice the diffraction limit. Alternatively in momentum space $k_f \leq k_h/2$ which for the limiting case the SIM resolution is twice as better as the original diffraction limit.

When the sinusoidal pattern is created from surface plasmons this limit can be bypassed. The plasmon fringes do not have to be created optically. The SPP fringes are created by two counter-propagating SPP waves on the surface of a metal-dielectric interface. The fringe periodicity is dependent on the SPP wavelength ($\lambda_S = 2\pi/k_S$) and not on the diffraction limit. Thus, for SPP structured illumination the fringe momentum is $k_f \equiv 2k_S \geq k_h/2$. Such fringes cannot be resolved optically but this fact has no relevance for SIM.

Because the fringe momentum of SPP is not limited by the optical diffraction limit but by the plasmonic one, the resolution enhancement of plasmonic SIM can be higher than the enhancement of standard optical SIM. Such enhancement is shown in Fig. 1.7. Compared to the optical diffraction limit

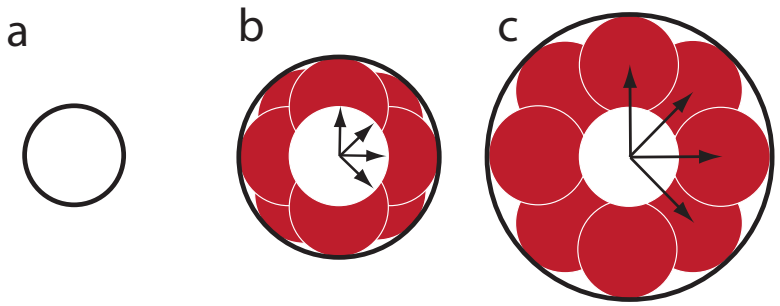

Figure 1.7: *Effect of the structured illumination. The black circles are the point spread functions in momentum space. The larger the circle the better the resolution. (a) Original point spread function of the lens without SIM. (b) Reconstructed point spread function via optical SIM for four directions (the arrows). Twelve images are acquired (three for each direction) to reproduce a high resolution one. The resolution can only be two times better than the diffraction limit because the illumination pattern has to be optically resolved (momentum of the fringes is within the white circle). (c) Reconstructed point spread function via Plasmonic SIM. The illumination fringes are created from counter propagating SPPs. These fringes are not optically resolved. For a continuous point spread function, plasmonic SIM achieves triple better imaging resolution as the diffraction limit.*

(Fig. 1.7a), optical SIM achieves double resolution (Fig. 1.7b), while plasmonic SIM achieves triple resolution (Fig. 1.7c). The Fourier Transform of the point spread function has to be a continuous function in momentum space (so as to provide information in real space over continuous length scales). To satisfy this continuity given by $k_f = k_h$, plasmonic SIM can only achieve triple resolution. Nevertheless, if a two step approach is used (first optical SIM with $k_f, 1 = \pm k_h/2$, followed by SPP SIM with $k_f, 2 = \pm 3k_h/2$), then the imaging resolution can be four times better the diffraction limit and the recinstructed point spread function is continuous.

An alternative way of using plasmonics for SIM microscopy is to use a nanohole grating. SPP waves propagating on the grating will become plasmonic Bloch modes. Because of different Bloch modes of the grating, multiple fringes will be created. Fringes from the counter-propagation of the $m-^{th}$ plasmonic Bloch mode have momentum $k_f \equiv 2(k_S \pm mk_g)$. The principal grating momentum, k_g, is inversely proportional to the hole periodicity of the array.

The consequences of these multiple fringe illumination for SIM microscopy

are easily understandable. Related to SIM microscopy, using multiple fringes is identical to using multiple values of k_f in parallel and not limited by the diffraction limit. In fact these values cover the entire inverse lattice of the grating. A similar technique has already been applied to optical SIM [56] by using nonlinearities: multiple k_f are created by the principal harmonic, the second one, and so on. Using plasmonic Bloch modes involves no nonlinearities.

1.5 Wavefront Shaping

We have seen in the previous section the potential of plasmonics for high resolution microscopy. To develop this potential a high degree of control of the propagating SPP waves is an absolute requirement. For example, to take advantage of the short wavelengths of these surface waves, we should be able to focus and redirect them at will and thus to create a plasmonic lens.

In this section we introduce an optical method that achieves high control over the optical wavefronts with the prospective of a possible extension of such over plasmonic wavefronts.

1.5.1 Principle of Wavefront Shaping (WS)

Wavefront Shaping was originally developed for multiple scattering media like: paper, paint, milk, sugar, biological tissue or the human brain. Light passing through this kind of media is scattered multiple times and the phase information is typically lost: we cannot see through paper. An even clearer example is glass: we can see through a glass window because the phase information is preserved, but we cannot see through glass powder because of the scattering from all the grains. Wavefront Shaping restores the phase information or at least part of it.

The principle of Wavefront Shaping is shown in Fig. 1.8. A plane wave from a laser source is sent to the multiply scattering sample. Such a sample can be described as an ensemble of optical channels or modes, with each channel introducing a specific path length. The spatial-intensity distribution in transmission is the interference pattern produced by the sum of all these channels. Because of the large distribution of path lengths, the phases of light transmitted via these channels are completely uncorrelated resulting in an interference pattern which is completely random. Such random interference pattern is the well-known laser speckle, as shown in Fig. 1.8a. The crucial idea behind Wavefront Shaping is to control the phase of sample channels to

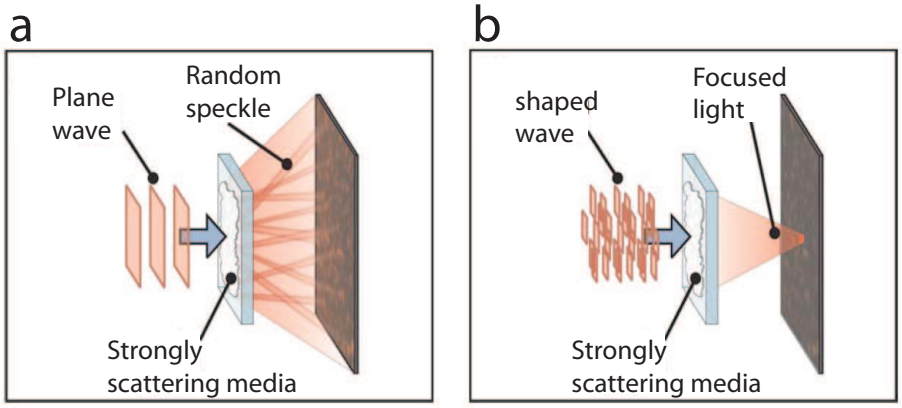

Figure 1.8: *Principle of Wavefront Shaping. (a) A plane wave incident on the multiply scattering sample is fully distorted giving rise to a speckle pattern in transmission. (b) When the incident wavefront is phase structured it becomes possible to spatially focus the transmitted light. The interference of all light channels at that particular point is constructive due to the structured wavefront. Picture taken from reference [57]*

change the speckle pattern. By shaping the phase of the incident wavefront it is possible to associate a different incident phase to each channel. When these incident phases compensate for the path length of the channel, then light from all channels will interfere constructively. This concept is shown in Fig. 1.8b. Due to the shaped wavefront, the constructive interference of a large number of channels at a given spot creates a focus in transmission.

An intuitive illustration of Wavefront Shaping is shown in Fig. 1.9. Before Wavefront Shaping (incident plane wave) the resultant electric field at a given spot is the sum of the electric fields from all the channels. These electric fields have random phases (directions of the arrows) thus the resultant electric field is also random. When Wavefront Shaping is applied, the electric fields from all channels have the same phase (aligned arrows) and the resultant electric field is the maximal.

1.5.2 Finding the right wavefront

Since its introduction in 2007, there have been many extensions to Wavefront Shaping. The major ones are focusing light inside random media [58], projecting a predesigned image through random media [59], focusing light

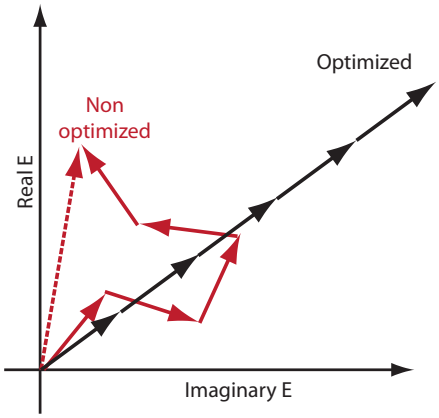

Figure 1.9: *Wavefront Shaping as constructive interference. For a non optimized wavefront, the electric fields (arrows) of different channels have random phases. The resultant (sum) electric field for an unstructured wavefront is also randomly oriented and has random amplitude. When the wavefront is optimized, the electric fields from different channels have the same phase. The amplitude of the resultant electric field is maximal for the optimized wavefront.*

pulses in space and time through random media [60, 61, 62], and use Wavefront Shaping for high resolution imaging [63, 64, 65]. The main problem that is solved in these interesting cases is: given a desired effect, how to determine the required wavefront?

The wavefront is phase and/or amplitude shaped using a pixelated spatial light modulator (SLM). The phase of each pixel can be independently controlled between 0 and 2π. In experiments typically 1000 to 10000 independent pixels are used, while the number of sample channels has to be larger to avoid redundancy. Finding the required wavefront for focusing (for example) among all the possible phase combinations of all pixels is certainly not a trivial problem. The problem of finding the fastest and most efficient algorithm to determine the wavefront is an active research topic. Various approaches have been proposed and demonstrated experimentally. We will introduce two widely used methods to determine the wavefront: (1) using a feedback approach, and (2) using a time-reversal approach. In most systems (samples) of interest these two approaches yield equivalent solutions.

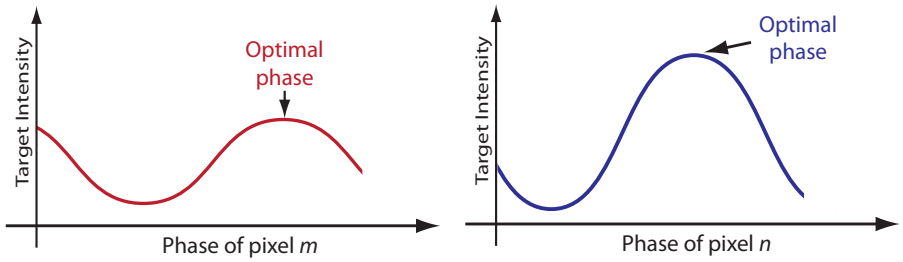

Figure 1.10: *Finding the optimal phases for two different SLM pixels. The intensity at the target as a function of the single pixel phase is a sinusoidal wave. The optimal phase of the pixel is the one that corresponds to the maxima of intensity. For a different pixel, an different interference pattern is observed, and thus a different optimal phase.*

1.5.3 Finding the wavefront via feedback loops

In the first investigations on Wavefront Shaping, the required phase front was determined via feedback loops. In this approach the sample is considered a black box with a large number of inputs and outputs. In transmission, among all possible outputs only one is chosen, for example creating a very bright spot (a focus). Such an output is very different from the normal speckle pattern because it shows a dramatic intensity increase at one point, the focus. To achieve the focused spot, the algorithm used optimizes the input (the incident wavefront) stepwise till achieving the desired output (focusing at a target spot). The input is optimized using as feedback parameter the intensity at the target. The feedback criteria is to maximize the intensity at the target.

Each input channel (pixel) is optimized independently from the others. The optimization principle is shown in Fig. 1.10. To determine the optimal phase of a pixel, the target intensity (the feedback parameter) is recorded as a function of the pixel's phase. This variation is provided by the interference with the constant background electric field. This background field is created by the light from all the other pixels, the phases of which is held fixed during the optimization step. A sinusoidal intensity at the target is observed as a function of the pixel phase. The phase for which the intensity is maximal is the optimal phase of the pixel, while the amplitude of the variation is related to the amplitude of the pixel's field.

This process is repeated for all pixels. When the phases of all pixels are determined the are all loaded together to create the desired focus. The full

cycle of the algorithm is repeated starting from the created focus till it converges (the focus does not get any brighter). The convergence is guaranteed by the linearity of the algorithm.

Variations to this algorithm and geometry have been shown. For example one may focus at many target points at the same time. Focusing at multiple targets is the first step towards creating an image in transmission. In other experiments, the same algorithm was used to focus inside scattering media using fluorescent particles as target points. These last experiments have implications for deep tissue imaging and medical laser therapy.

1.5.4 Finding the wavefront via optical Time Reversal

Another very efficient way of determining the required wavefront for focusing and beyond is the application of time reversal. This technique was originally developed for ultrasound waves, but was rapidly generalized to other waves like microwaves, seismic waves and finally light waves. The principle of Time Reversal (TR) is simple: the sample is described as matrix T with the element T_{ji} describing the complex-valued transfer between input channel i and output channel j. If this matrix is known, then any required wavefront for any desired output is fully determined by the time reversed matrix T^{-1}.

Let V be the vectorial space of all possible inputs and W be the vectorial space of all possible outputs. For simplicity we assume that both vectorial spaces have the same dimension N. The V space comprises all the possible linear combinations of an orthonormal set $\{v_i\}$, for example the independent pixels of the SLM. Similarly, W is formed by all the possible linear combinations of an orthonormal set $\{w_j\}$, for example the pixels of a CCD detector after the sample. We write

$$V \equiv \left\{ \mathbf{v} = \sum_{i=1:N} a_i \mathbf{v}_i \,\middle|\, a_i \in \mathbb{C} \right\}, \tag{1.26a}$$

$$W \equiv \left\{ \mathbf{w} = \sum_{j}^{N} b_j \mathbf{w}_j \,\middle|\, b_j \in \mathbb{C} \right\}, \tag{1.26b}$$

$$\mathbf{w} = T \cdot \mathbf{v}. \tag{1.26c}$$

The transfer function of the sample, T, has to be determined experimentally. It is sufficient to determine it only for basis vectors, v_i. As for feedback algorithms, to determine the element T_{ji} an interferometric measurement is needed. The transmitted electric field from the single SLM pixel ($\mathbf{v} = \mathbf{v}_i$)

interferes with a constant background field. The interference pattern at the CCD fully determines the amplitude and phase of the transmitted electric field from this SLM pixel to all the CCD pixels.

Once the matrix is determined, it is in principle straight forward to find the required incident wavefront $\mathbf{v}_d$ for any desired output $\mathbf{w}_d$. In fact

$$\mathbf{w}_d = T\mathbf{v}_d \qquad \Rightarrow \qquad \mathbf{v}_d = T^{-1}\mathbf{w}_d. \tag{1.27}$$

The last step involves the inversion of the sample matrix to determine the desired wavefront. Matrix inversion is an exponential algorithm and thus the inversion of a 10000 by 10000 matrix is not realistic. Fortunately, when the sample is not absorbing, the matrix is unitarian and the matrix inversion becomes much simpler. The inverse of an unitarian matrix is its conjugated transpose: $T^{-1}_{ji} = T^*_{ij}$. Such "flipping" of the matrix elements can be quickly processed. For these unitarian cases Time Reversal experiments have elegantly demonstrated the ability to create a variety of outputs, like focusing or even the creation of a programmed image.

1.5.5 Comparison between feedback algorithms and Time Reversal

We have previously described two main ways to retrieve the derided optical wavefront: feedback Wavefront Shaping and Time Reversal mirror. Now we compare advantages and disadvantages of these two techniques. Wavefront Shaping and optical Time Reversal yield the same results for the largest majorities of the cases, so these algorithms share more similarities than differences. The few differences are the convergence speed, signal quality and range of outputs.

Time Reversal is a full matrix approach while Wavefront Shaping is a projective approach. With TR the sample matrix has to be measured only once and the desired wavefront for any given output is than quickly calculated from the sample. With Wavefront Shaping algorithms, for any desired output, the retrieval of the wavefront is a new experimental measurement. Thus, with TR, switching between different outputs is faster than with WS. Nevertheless, because Wavefront Shaping algorithms are based on output optimization, the output quality is higher. Applying the feedback algorithm twice, generally improves the quality of the desired output by up to a factor three. For example, theory predicts that Wavefront Shaping of 256 independent segments yields a maximal focus enhancement of 201 times: optimization algorithms [57] report a focus enhancement of nearly 150 times, while

Time Reversal algorithms [66] report an enhancement of 54 times.

Whenever choosing one algorithm or the other depends on the desired application. For fixed samples (no internal motion) and with no absorbtion centers, TR might be preferred. For dynamic samples or samples with absorbing centers, WS feedback algorithms perform better.

1.5.6 Wavefront Shaping of plasmonic channels

Wavefront Shaping tunes the constructive interference of different sample channels. For multiply scattering samples, these channels are typically transmission or reflection channels. For metallic nanostructures, these channels could very well be plasmonic channels. Thus using Wavefront Shaping it might be possible to control plasmonic channels at will, for example to create a plasmonic lens. The shape of the lens is deformable because it's shape is determined by the incident optical wavefront. The creation and the application of this deformable plasmonic lens for microscopy will be the central theme of this thesis work.

CHAPTER 2

ACTIVE CONTROL OF PLASMONIC FIELDS

We control the wavefronts of Surface Plasmon Polaritons (SPP) on nanohole arrays using a digital spatial light modulator. Optimizing the plasmonic phases via feedback we focus SPPs at a freely pre-chosen point on the surface of the array with high resolution. Digital addressing of SPPs without mechanical motion will enable novel interdisciplinary applications of advanced plasmonic devices in cell microscopy, optical data storage and sensing.

2.1 Introduction

Positioning and focusing waves in transparent media requires fine tuning of the phase profile so that waves converge and constructively interfere at a point. A conventional lens uses refraction to redirect the waves to the focus and a well-designed lens shape to align the phase vectors of these waves. Due to the fixed geometric shape of the lens, the position of the focus can only be controlled by mechanically moving the lens or changing the angle of incidence of the incident beam. Focusing and controlling the position where waves constructively interfere in complex structures require new methods that are more versatile [67]. Optical wavefront shaping has become a popular method that allows to focus light even inside completely disordered materials [58, 68].

The field of plasmonics [25] offers a complementary route to control light fields with metallic nanostructures through the excitation of Surface Plasmon Polaritons (SPP's) [69, 70]. These surface waves, bound to a metal dielectric interface, tightly confine electromagnetic energy [71]. Plasmonics has applications in sensing [33], photovoltaics [72], quantum communication [73, 74], nano circuitry [29, 30], metamaterials [75, 76] and super-resolution microscopy [77].

Positioning and focusing SPP waves in a controlled way is important for nanophotonic applications. To date plasmonics offers only limited flexibility in the control of light fields: as with the conventional lens the geometry is typically fixed, so for a given optical frequency the locations of optical field enhancement are also fixed. Recently, some breakthroughs have been made on active control in which the intensity of the light fields is influenced in time, either through pump-probe [49, 78, 79, 80] or through coherent control [81]. Only in specific cases does this control also lead to spatial selectivity [82, 83, 84]. However, in these experiments the spatial selectivity is limited to a few modes predefined by the sample structure.

2.1.1 Our contribution

We demonstrate here a new level of control of SPP wavefronts. This control allows us to tune any SPP interference phenomenon with unprecedented flexibility. Specifically, we show that we can generate and focus SPPs at any location on a nanohole array with an electronically controlled spatial light modulator and standard helium neon laser. Because the light-to-SPP conversion process is coherent, the structured optical wavefront is projected onto

the SPP wavefront. This conversion gives us full phase control of the SPPs, allowing us to shape the SPP wavefronts digitally. Because we use optimization loops to determine the necessary wavefront, our method is applicable to any plasmonic structure. Such flexible and digital control of SPPs is a large step forward towards interdisciplinary applications of advanced plasmonics.

2.2 Experimental configuration

2.2.1 The nanohole array(s)

The sample is a metallic nanohole array with a rich electromagnetic behavior [85]. Subwavelength gratings offer potential for super-resolution either for dielectric [86] or metal-dielectric [87] configuration. Our sample is composed of a 200 nm of gold film deposited on top of 1 mm BK7 glass substrate. The array covers an area of 30 x 30 μm^2 and the hole period (a_0) is 450 nm. Square holes were milled (focused ion beam) with sides of 177 nm. Other arrays with different hole periods will also be used.

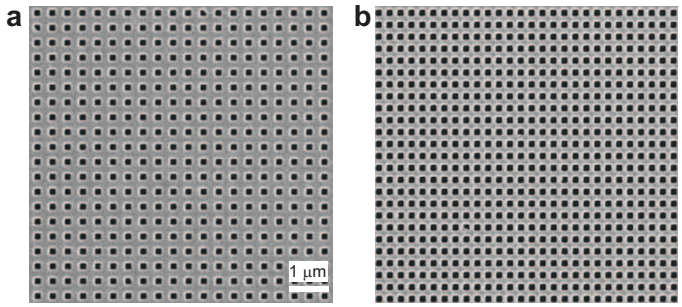

Figure 2.1: *SEM image of the sample: a nanohole array on gold. The hole period is 450 nm while the hole side is 177 nm*

The electromagnetic behavior close to subwavelength corrugations on metal films is very rich and can be described in terms of a hybrid wave [88] arising from SPPs and quasi-cylindrical waves [89]. The same description also holds for nanohole arrays. Nevertheless, it is generally well accepted that for optical frequencies SPPs are very efficiently excited on hole arrays due to their resonant nature and thus dominate the electromagnetic field.

The SPP wavelength at the gold-air interface from incident radiation of $\lambda_0 = 633$ nm is given by

$$\lambda_S = \lambda_0 \mathrm{Re}\sqrt{\frac{\varepsilon_\mathrm{m} + \varepsilon_\mathrm{d}}{\varepsilon_\mathrm{m}\varepsilon_\mathrm{d}}}, \tag{2.1}$$

with ε_m and ε_d the dielectric constants of gold and air, respectively. Using tabulated bulk values for ε_m [53] we found $\lambda_S = 600$ nm.

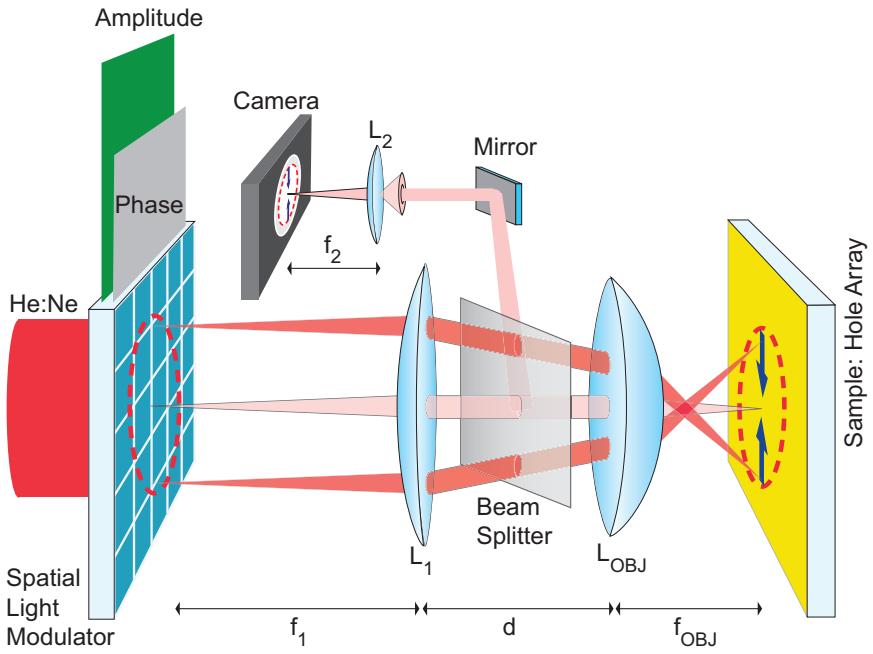

Figure 2.2: *Experimental Setup. The Spatial Light Modulator (SLM) is projected onto the sample via the two-lens imaging system L_1 and L_{OBJ}. The demagnification is 650 times. Every image point on the sample is formed with a different average angle of incidence (shown for three pixels). The amplitude and phase of each pixel of the SLM are independently controlled with a computer. The sample is a nanohole grating engraved on a gold film. The blue arrows illustrate the propagation of Surface Plasmon Polaritons (SPP) launched from two pixels of the SLM. The amplitudes and phases of the SPPs are effectively clamped to those of the launching pixels. The surface of the sample is imaged onto the camera via L_{OBJ} and L_2.*

2.2.2 The setup

Our aim is to digitally control the amplitude and phase of SPPs locally on the surface of the sample. This control is achieved by imaging a Spatial Light Modulator (SLM) onto the surface of the sample thus mapping each unit cell (pixel) of the SLM to a corresponding area on the sample. Amplitude and phase control of the SLM is achieved by grouping pixels into superpixels. We independently control amplitude and phase of 32 x 32 superpixels. The image of each superpixel locally excites surface waves [90] (to which SPPs are the dominant contribution).

A diagram of the setup is given in Fig. 2.2. Based on SPP momentum conservation we designed the imaging system such that plasmons are launched toward the center. The light reflected from the sample is imaged on the detector. This light includes both the direct reflection of the illuminating beam and the scattered light from SPPs. Thus the resulting image is a combination of both the SLM amplitude pattern and the generated SPPs.

2.3 SPP amplitude experiments

2.3.1 Preparation of the SPP arena

To separate plasmonic from optical effects we spatially design the amplitude of the incident light to define four bright plasmon launching areas and one central dark arena. Any intensity detected inside the arena is purely plasmonic. The designed amplitude profile for focusing experiments is a four-block pattern of fully "on" (A=1) superpixels on an "off" (A=0) background. The resulting illuminated areas on a bare gold substrate are visible in Fig. 2.3a. The overall phase is constant. Each "on" block is 10 x 8 superpixels in size. Because no SPPs are launched on bare gold due to momentum mismatch, the image of Fig. 2.3a is used as a background reference and measure of contrast ratio between the "on" and "off" areas. The observed contrast is nearly three orders of magnitude, confirming that no photons enter the SPP arena.

2.3.2 SPP propagation in the arena

When the designed amplitude profile is projected onto the hole array, SPPs propagate into the central dark arena. The nanohole array has a dual role: it is used to launch SPPs (bright rectangles in Figs. 2.3b-2.3d) and to visualize the launched SPP's through their out-of-plane scattering in the central arena.

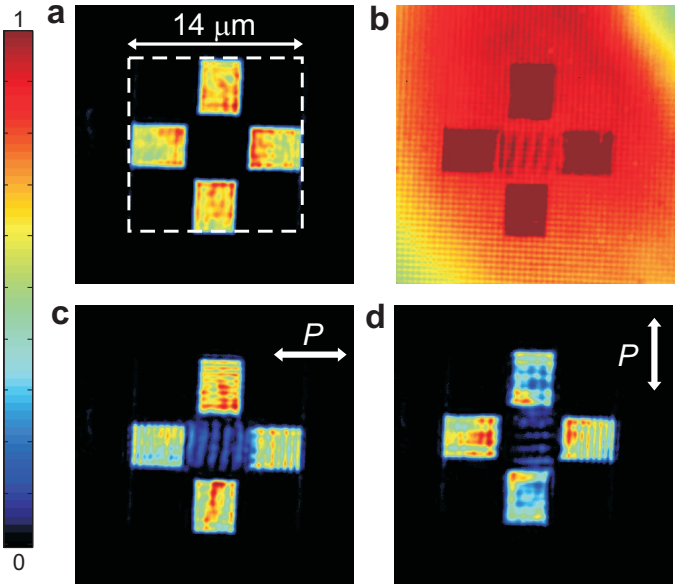

Figure 2.3: *The SLM projection and the resulting surface plasmons for uniform phase profile (no optimization). In each image the bright rectangle(s) are the illuminated (amplitude=1) SPP launching areas. The SPPs are observed in the dark (amplitude=0) central arena. (a) Bare gold reference (no SPPs launched). The dashed lines demarcate the SLM area. (b)-(d) SLM projected on the 450 nm hole array. (b) SLM image plus white light illumination to observe the hole array. (c) SPPs launched toward the central arena. (d) Vertical polarization of incident light (horizontal polarization for the other images).*

The SPPs are launched only along the direction of the incident polarization as seen in Figs. 2.3c and 2.3d, consistent with expectations [91, 92]. In Fig. 2.3b, the sample is illuminated both by the structured amplitude profile and an additional white light source, revealing both the hole array grating itself (the fast amplitude modulation) and the laser light. This figure also demonstrates the optical resolution of the setup: sufficient to resolve the presence of the hole array pattern but not the shape of holes.

2.3.3 Formation of the SPP standing pattern

In Fig. 2.4a and 2.4b a SPP plane wave with exponentially decaying amplitude is launched from a single bright area towards the SPP arena. The measured propagation length is $\ell_S = 3.4 \pm 0.1$ μm and the observed direc-

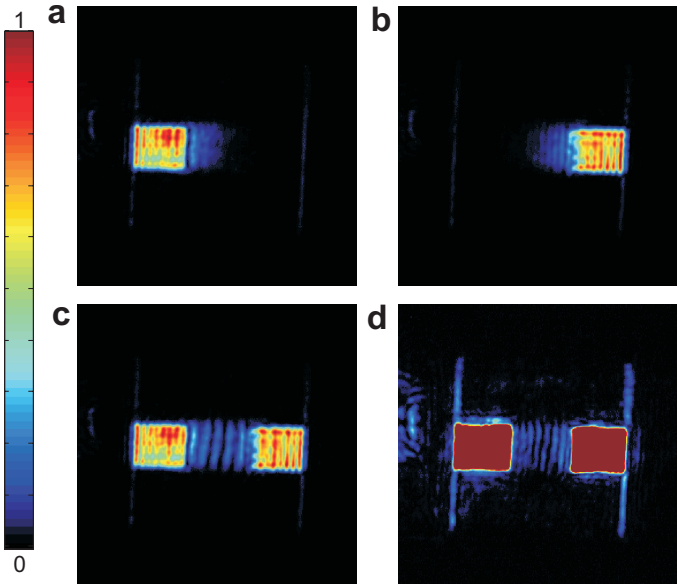

Figure 2.4: *(a)-(b) Exponentially decaying SPP plane waves launched in opposing directions. (c) SPP fringe formation via counter propagating waves. (d) SLM projected on the 400 nm hole array results in a different fringe pattern.*

tionality is consistent with our oblique illumination scheme.

When two counter propagating SPP waves interfere, a standing wave pattern of intensity is created. The observed period of the fringe pattern is clearly not half the SPP wavelength, as is expected for SPPs propagating on an ideally smooth and non-corrugated sample. Actually, the fringe period of Fig. 2.4d is found to be sample dependent. We measured fringe periods of 1 ± 0.05 μm, 0.85 ± 0.05 μm and 0.7 ± 0.05 μm for grating pitches of 450 nm, 425 nm, and 400 nm respectively. The standing pattern detected on the 400 nm grid is presented in (Fig. 2.4d). We attribute the fringe patterns to a Moiré effect between the true standing SPP wave and the periodicity of the arrays.

2.4 SPP phase experiments

Now we present experiments of SPP focusing with digital phase control. These experiments are performed on the nanohole array with 450 nm grating

pitch. The achieved SPP focusing is shown in (Fig. 2.5). We use a phase optimization loop [93] to focus SPPs at a pre-chosen target. This loop yields

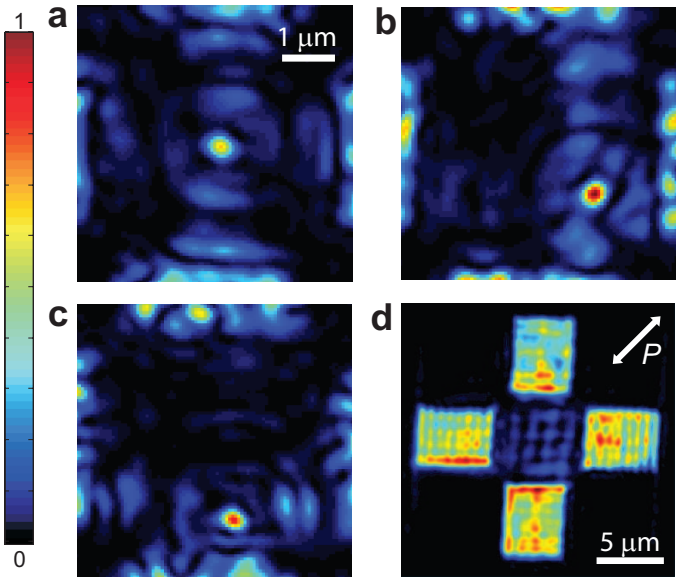

Figure 2.5: *Digital focusing of SPPs. (a) The relative phases of the superpixels are optimized to focus SPPs in the center of the SPP arena. The intensity in the target spot is purely plasmonic and 20 times higher than the average background of an unstructured plasmonic wavefront. The focus size is diffraction limited by the detecting optics. (b) and (c) Demonstration of SPP focusing on freely chosen targets in the SPP arena. (d) Background reference of an unstructured SPP wavefront (uniform phase profile).*

the optimal phase ($\widetilde{\phi}$) for each superpixel as well as the relative contribution (C) to focus. The amplitude profile is the same as for the bare gold case with four launching areas and a central dark arena where only SPPs can propagate. The incident polarization is diagonal with the grating lines so that all bright superpixels contribute to the focus, thereby maximizing the NA and resolution.

2.4.1 SPP focusing and scanning

Successful focusing at the center of the SPP arena is shown in Fig. 2.5a. The structured SPP wavefront produces an intensity in the designated target that is at least 20 times higher than the average SPP background of an

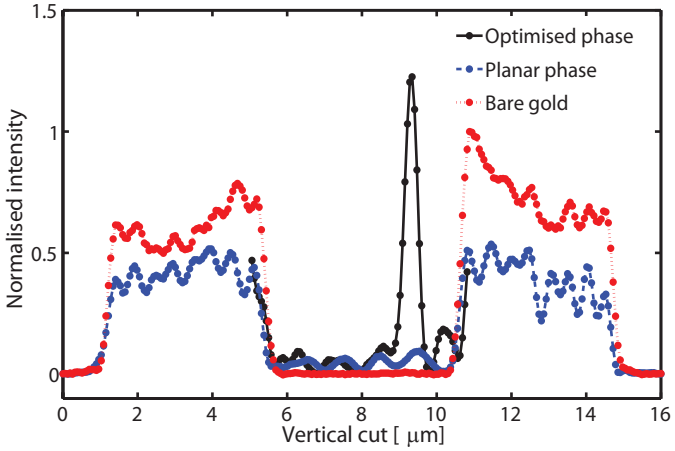

Figure 2.6: *Quantitative analysis of the SPP focusing showing vertical cuts of Figs.2.5b and 2.5d. These cuts are normalized to the peak intensity of the bare gold case, also included in the graph.*

unstructured wavefront. The measured size of the plasmonic focus is 410 nm, consistent with the diffraction limit of our optics. The flexibility of the method is demonstrated in Fig. 2.5b and Fig. 2.5c which show the SPP focus relocated without mechanical motion to controlled positions in the plasmonic arena.

2.4.2 Interpretation and consequences

We interpret SPP focusing in terms of Green's functions connecting the electric fields at any two points. We idealize every "on" superpixel n with a light source positioned at $\mathbf{r}_n$ and with phase $\phi(\mathbf{r}_n)$ and strength $A(\mathbf{r}_n) = 1$. The amplitude of the electric field (normalized to the incident field) at the target $\mathbf{r}_0$ due to these sources is

$$E\left(\mathbf{r}_0, \{\phi(\mathbf{r}_n)\}\right) = \sum_n^N g\left(\mathbf{r}_0, \mathbf{r}_n\right) \exp\left[i\phi(\mathbf{r}_n)\right], \tag{2.2}$$

where $g\left(\mathbf{r}_0, \mathbf{r}_n\right)$ is the Green's function connecting each source to the target, and the sum runs over all the "on" superpixels of the amplitude profile. The target field is maximal when all source contributions are in phase. The optimal phase for superpixel n is $\widetilde{\phi}(\mathbf{r}_n, \mathbf{r}_0) = -\arg\left[g\left(\mathbf{r}_0, \mathbf{r}_n\right)\right]$. Assigning this phase to the superpixel yields an intensity increase of $C(\mathbf{r}_n, \mathbf{r}_0) = \left|g\left(\mathbf{r}_0, \mathbf{r}_n\right)\right|$.

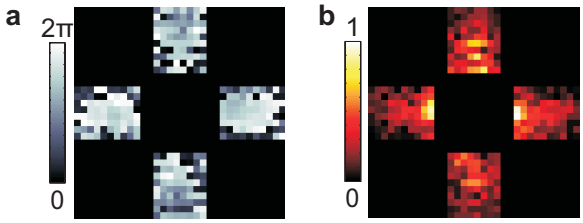

Figure 2.7: *Green's function. In achieving the focus of Figs.2.5a we recorded the map of optimal phases (a) and of relative contributions (b) of the superpixels, respectively. Due to reciprocity these maps coincide with the phase and amplitude Green's function of a SPP source at the target. The amplitude map shows the decaying nature of the SPPs.*

Combining together the amplitude and phase of the Green"s function,we have

$$g\left(\mathbf{r}_n, \mathbf{r}_0\right) = C(\mathbf{r}_n, \mathbf{r}_0) \exp\left[i\widetilde{\phi}(\mathbf{r}_n, \mathbf{r}_0)\right]. \tag{2.3}$$

Equation (2.3) implies that when a focus is achieved in the SPP arena, the recorded optimal phases and relative contributions of the superpixels Fig.2.7 give the Green's function for a plasmonic source located at that exact focus point. Thus the superpixels of the SLM effectively behave as amplitude and phase sensitive detectors. These results are valid for any Green's function or nanostructure and can be extended to the time domain [94] and the transfer matrix approach [66].

For a perfectly smooth sample with no corrugations the SPP Green's function is simply a cylindrical wave in two dimensions (the Hankel function $H_0^{(1)}(Kr)$ with K the complex-valued SPP momentum). Our digitally measured Green's function includes the light-to-SPP coupling and therefore presents much more complexity.

2.5 The phase optimization routine

In this section we will show how the optimal phase of each superpixel is measured [93]. We idealize every "on" superpixel n with a light source positioned at $\mathbf{r}_n$ and with phase $\phi(\mathbf{r}_n)$ and strength $A(\mathbf{r}_n) = 1$. The amplitude of the electric field (normalized to the incident field) at the target $\mathbf{r}_0$ due to these sources, already shown in Eq. (2.2), is

$$E\left(\mathbf{r}_0, \{\phi(\mathbf{r}_n)\}\right) = \sum_n^N g\left(\mathbf{r}_0, \mathbf{r}_n\right) \exp\left[i\phi(\mathbf{r}_n)\right], \tag{2.4}$$

where $g\left(\mathbf{r}_0, \mathbf{r}_n\right)$ is the Green's function connecting each source to the target, and the sum runs over all the "on" superpixels of the amplitude profile. We use an optimization loop to focus at a chosen target: the phase of one single superpixel is varied from 0 to 2π causing an intensity oscillation at the target location due to interference with the static field of the other superpixels (all other superpixels have zero phase). The field at the target as a function of the phase of the single superpixel n is:

$$E\left[\mathbf{r}_0, \phi(\mathbf{r}_n)\right] = \sum_{m\neq n}^N g\left(\mathbf{r}_0, \mathbf{r}_m\right) + g\left(\mathbf{r}_0, \mathbf{r}_n\right) \exp\left[i\phi(\mathbf{r}_n)\right] \equiv S_n + g_{0,n} \exp\left(i\phi_n\right), \tag{2.5}$$

where S_n is defined as the static background of all other superpixels and we exchanged in the formula the spatial dependence $(\mathbf{r}_n)$ with a matrix index n. The measured intensity oscillation due to the field of Eq. (2.4) is

$$I_0(\phi_n) = |S_n|^2 + |g_{0,n}|^2 + 2|S_n||g_{0,n}| \cos\left[\arg(S_n) - \arg(g_{0,n}) - \phi_n\right]. \tag{2.6}$$

The amplitude of the intensity oscillation is $C_n = 2|S_n||g_{0,n}|$ and the optimal phase of the superpixel is $\widetilde{\phi}_n = \arg(S_n) - \arg(g_{0,n})$. One iteration is completed by repeating the procedure for all other superpixels. Finally we make the assumption that the contribution of a single superpixel is small compared to the sum of all other superpixels. Under this assumption we can consider S_n as a constant independent of the index n and thus we set its phase to zero. This yields the desired result

$$g\left(\mathbf{r}_n, \mathbf{r}_0\right) = constant * C(\mathbf{r}_n, \mathbf{r}_0) \exp\left[i\widetilde{\phi}(\mathbf{r}_n, \mathbf{r}_0)\right]. \tag{2.7}$$

Equation (2.7) confirms that via our algorithm we are effectively measuring the plasmonic Green's function as intuitively expected from eq. (2.3). In conclusion, through achieving SPP focusing, our optimization algorithm measures the amplitude and phase Green function for a source in the exact focal spot.

2.6 Conclusions

With digital plasmonics we demonstrate the first plasmonic system that operates as a "*black-box*", requiring the user only to input the desired location of the nanoscale plasmonic focus which is the system's output. Specifically, we focus SPPs on hole arrays and locally scan the focus freely over a field-of-view (SPP arena) without any mechanical translation. In achieving such dynamic focusing we recorded amplitude and phase Green's functions. These digital records, which contain the full complexity of the Green's function, are used as self-calibrated inputs. The method can be extended to the time domain and to any plasmonic structure, thus focusing light pulses in time and space for any given nanostructure. By proper tailoring the nanostructure of the SPP arena will be possible to confine and manipulate the achieved focus beyond the diffraction limit. This digital plasmonic workbench is anticipated to enable interdisciplinary applications in microscopy, optical data storage and in bio-sensing.

2.7 Acknowledgments

We thank Elbert van Putten and Jean Cesario for stimulating and helpful discussions. For sample fabrication we thank Hans Zeijlermaker. This work is part of the research program of the "Stichting voor Fundamenteel Onderzoek der Materie", which is Financially supported by the "Nederlandse Organisatie voor Wetenschappelijk Onderzoek".

CHAPTER 3

CONTROLLING PLASMONIC BLOCH MODES

We study and actively control the coherent properties of Surface Plasmon Polaritons (SPPs) optically excited on a nano-hole array. Amplitude and phase of the optical excitation are externally controlled via a digital spatial light modulator (SLM) and SPP interference fringe patterns are designed and observed with high contrast. Our interferometric observations reveal SPPs dressed with the Bloch modes of the periodic nano-structure. The momentum associated with these Dressed Plasmons (DP) is highly dependent on the grating period and fully matches our theoretical predictions. We show that the momentum of DP waves can in principle exceed the SPP momentum. Actively controlling DP waves via programmable phase patterns offers the potential for high field confinement applicable in lithography, Surface Enhanced Raman Scattering and plasmonic structured illumination microscopy.

3.1 Introduction

Important systems such as biological cells, single molecules, and nanodevices, strongly interact with visible light on sub-wavelength scales. Yet standard microscopy and related applications in lithography, sensing and imaging are diffraction limited. Plasmonics [25] offers an alternative route to control light with sub-wavelength precision through the excitation of Surface Plasmon Polaritons (SPPs) [69, 70] . These surface waves, bound to a metal dielectric interface, are a hybrid mode of photons and electronic change-density oscillations. The intrinsic momentum associated with these evanescent waves is higher than that of free propagating photons. Thus, for a fixed light frequency, SPPs have a higher effective refractive index and tighter confinement of electromagnetic energy [71] .

Achieving the full promise of SPPs in applications requires two types of innovation, 1) subwavelength confinement and 2) flexible control. Confinement has been achieved via tailored samples that allow plasmonic waves to be coupled into the topological modes of a fabricated structure. This mode can be referred to as a dressed plasmon (DP) because the propagation is determined by the nanostructure. Successful confining geometries include coupled nanoantennas [95, 96, 97] that fully localize modes in the gap between neighboring antennas, and V-grooved [98, 31] and nanowire [99, 100] waveguides that support 1D propagating modes deeply confined inside the waveguide. The field confinement in such geometries exceeds that of freely propagating SPPs by an order of magnitude. Flexible control has been partially achieved in several very recent experiments [101, 102, 103] . These and similar experiments achieve control of propagating SPPs via a single parameter such as the polarization state, the angle or the wavelength.

Theoretical works have shown that it is possible to take confinement and flexible control much further. For example, it has been theoretically suggested to use nanostructures [104, 105] , such as well designed gratings [106] , to support extended DP waves to obtain both high confinement (and thus resolution) and flexible control over a large field of view [86, 87] . Experimental implementation of this kind of flexible approach would open the door to appplications such as plasmon based Saturated Structured Illumination Microscopy (SSIM) [56] and related applications in imaging [107, 108] , sensing [109] and lithography [110].

3.2 Our contribution

In these experiments we are not only able to generate Bloch mode dressed plasmons supported by periodic nanostructures but also obtain full flexible optical control over these modes via plasmonic phase imprint [111, 112] . Using a Spatial Light Modulator we shape the amplitude and phase profile of the incident laser beam over a large 2D field of view. The SLM is imaged onto the surface of the sample thus addressing each pixel of the SLM (the control parameters) to a corresponding area on the sample. We use the amplitude control to measure with high contrast fringe patterns generated from two counter propagating SPP waves. The momentum associated with the standing waves shows strong dependence on the lattice period of the grating and reveals the Bloch-mode dressing of the surface plasmons. Furthermore, we use the phase control to shape the interference pattern at will. As an example of such phase control we chose to deterministically scan and tilt the fringe pattern of the dressed plasmons as required for a plasmonic analogue of structured illumination microscopy.

3.3 Experimental configuration

A diagram of the setup is given in Fig.3.1. The SLM is imaged on the sample via a lens (L1) and the objective, referred to hereafter together as the imaging system. The SLM is at the focal plane of lens L_1 (focal length 130 cm). The image at infinity created by L_1 is projected onto the sample at the focal plane of the objective. Our SLM (Holoeye LC-R 720) is a reflective display based on Twisted Nematic Liquid Crystal on Silicon technology. The display has a total of 1280 x 768 pixels operating at 60 Hz with a response time of 3 ms. Each pixel is 20 μm in size and addressed with a 8-bit voltage. The objective (Nikon LU PLAN FLUOR P 100X) is infinity corrected and metallurgic (no coverslip compensation) with a Numerical Aperture (NA) of 0.9 and a magnification of 100 times (defined for a tube lens of 20 cm focal length). The focal length of L_1 is 6.5 times larger than that of the standard tube lens yielding a corresponding 650 times demagnification of the image. The distance between L_1 and the objective is 1 m i.e. smaller than the focal length of L_1 (non-telecentric imaging system). In this configuration the average angle of illumination is position dependent, which is an important condition for the SPPs launching.

The light emitted in reflection from the sample is imaged on the CCD (AVT Dolphin F145 B) using lens L_C as tube lens. This light includes

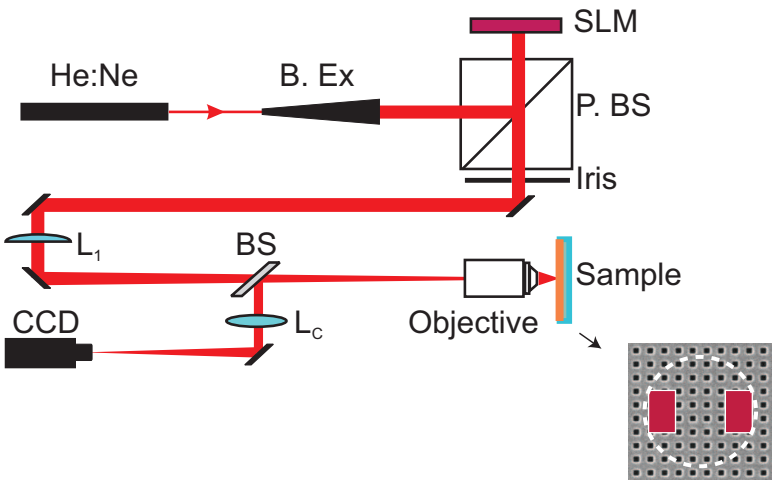

Figure 3.1: *Experimental Setup. Linearly polarized light from a HeNe laser is first expanded by a beam expander (B. Ex) and sent to the the Spatial Light Modulator (SLM). A polarizing beam splitter (P. BS) filters only the cross-polarized component of the SLM's reflection. The SLM is imaged point to point onto the sample (a nano perforated gold film on glass) via the imaging system (lens L_1, objective). The sample is in the objective's focal plane of the with the gold side towards it (where the SLM image is created). The reflection from the sample is imaged point to point onto the CCD camera (objective, lens L_C). Inset: Sample illuminated with structured amplitude from the SLM. The white dashed ring indicates the SLM perimeter while the red rectangles indicate SLM segments set to non-zero amplitude.*

both the direct reflection of the illuminating beam and the scattered light from SPPs. Thus the resulting image is a combination of both the SLM amplitude pattern and the generated SPP pattern. To distinguish between the two we choose illumination patterns that allow SPP observation in a non-illuminated area. The amplitude and phase of the excitation pattern is controlled by applying the 4-pixel technique [113] to the SLM. Four adjacent pixels are grouped into a superpixel by selecting a first diffractive order with the neighbor-pixel fields being $\pi/4$ out of phase. In this work we use 32 x 32 superpixels. Every SLM superpixel is imaged on a sample area of 440 x 440 nm^2 containing nearly one unit cell of the grating. Such a superpixel grouping provides continuous modulation over full amplitude ($A \in [0, 1]$) and phase ($\Phi \in [0, 2\pi]$) ranges with a cross modulation of less than 1%.

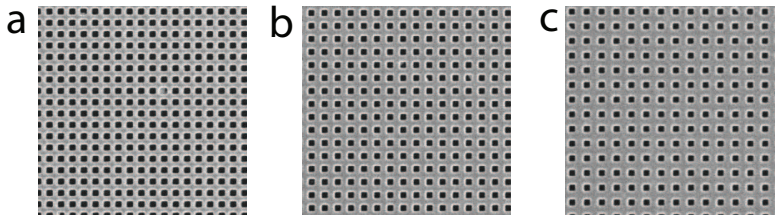

Figure 3.2: *Samples. SEM fragments of the hole arrays with grating period of (a) 350 nm, (b) 400 nm and (c) 450 nm.*

3.3.1 Samples

Our samples, nanohole arrays similar to those used typically for Enhanced Optical Transmission experiments [24], were fabricated using focused ion beam milling. A 200 nm gold film was deposited on top of 1 mm BK7 glass substrate with a 2 nm chromium adhesion layer. Square holes were milled with sides of 177 nm. The hole array covers an area of 30 x 30 μm^2. Five samples were fabricated with array periods (a_0) varying from 350 nm to 450 nm. The sample was placed with the gold side towards the objective to observe SPP waves from the gold-air interface.

3.3.2 Momentum conservation

We calculate the SPP momentum for incident radiation of $\lambda_0 = 633$ nm ($k_0 = 2\pi/\lambda_0$) using tabulated values [53] of the dielectric constants of gold ε_m and air ε_d

$$k_S = k_0 \mathrm{Re}\sqrt{\frac{\varepsilon_\mathrm{m}\varepsilon_\mathrm{d}}{\varepsilon_\mathrm{m}+\varepsilon_\mathrm{d}}} = (m,n)k_G + k_0 \sin\theta, \tag{3.1}$$

where the last equality expresses the fact that the SPP momentum is a vectorial sum of the $(m,n)k_G$ grating orders ($k_G = 2\pi/a_0$) and the in-plane component of the incident light. With our oblique illumination scheme, the average angle of incidence θ is not uniform but position dependent.

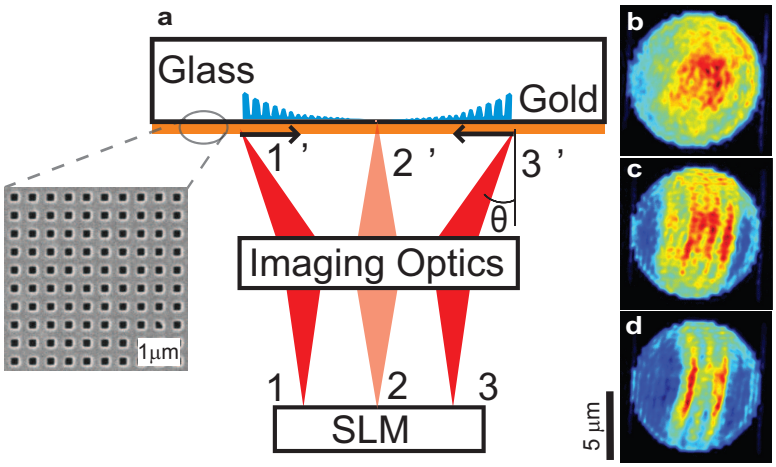

Figure 3.3: *(a) Sketch of the sample illumination. Each SLM point is imaged on the surface of the sample with a different average angle of incidence θ. (b-d) Reflection from different samples illuminated with a uniform amplitude and phase profile. (b) On the bare gold sample the reflection is also uniform since no SPPs are launched. Deviations from a truncated gaussian profile are due to surface roughness. (c) The dark areas of low reflection from the 400 nm hole array indicate the angular (spatial) bands for SPP launching. (d) These bands are sample dependent as shown for the 425 nm hole array. Inset: SEM image of the samples.*

3.4 The oblique illumination scheme

This illumination scheme and its role on how SPPs are launched is illustrated in Fig. 3.3. Each SLM's superpixel is projected onto the sample with a different average angle of incidence (Fig. 3.3a) and thus with a different in-plane component of the incident light. The momentum conservation described in Eq. (3.1) will be satisfied only within specific angular bands which are position dependent. In Fig. 3.3b-d we show the surface of three different samples illuminated with a uniform amplitude profile across the SLM with horizontal polarization.

For the reference bare gold film and a uniform SLM amplitude and phase profile, the reflected image is identical to incident beam profile since no SPP can be launched (Fig. 3.3b). Corrugations on the bare metal film (due to polycrystalline gold) give rise to a speckle pattern on top of the truncated (80%) gaussian profile. When the same uniform amplitude and phase profile

is projected onto a nanohole array, dark and bright areas are clearly distinguishable as shown in Fig. 3.3c-d. Dark areas correspond to suppressed reflection from the sample. We interpret these dark areas as the spatial (angular) bands that satisfy Eq. (3.1) and thus where plasmons are efficiently excited from the incident light. The location of these bands strongly depends on the array momentum. Even a 25 nm variation of the array period from $a_0 = 425$ nm (Fig. 3.3c) to $a_0 = 400$ nm (Fig. 3.3d) yields a spatial band shift of nearly 2 μm.

SPPs waves launched in the momentum matched bands propagate towards each other and interfere (Fig. 3.3). Yet this interference pattern is observed on a high background due to the direct reflection of the incident light.

3.5 Amplitude Experiments

Here we show experiments with amplitude shaping. The phases of all superpixels are set to zero.

3.5.1 Background-free observation of SPP fringes

To remove the background and enhance the contrast of the SPP interference pattern we spatially design the incident amplitude profile with "on" areas of amplitude A = 1 and an "off" background of A = 0. Each "on" area is composed of 10 x 8 superpixels and is located in the vicinity of the two symmetric angular bands. The SPP interference patterns are then observed in the central non-illuminated area which is our SPP field

Results from this designed amplitude profile are shown in Fig. 3.4. When the two counter propagating SPP waves launched in the "on" areas interfere, a standing wave pattern of intensity is created. For SPPs propagating on an ideally smooth and non-corrugated sample we expect the period of the fringe pattern to be half the SPP wavelength ($\lambda_S = 2\pi/k_S = 590nm$). Instead, the measured fringe period is found to be sample dependent (Fig. 3.4a-d). We measured fringe periods P of 1 ± 0.05 μm, 0.85 ± 0.05 μm, 0.65 ± 0.05 μm, 0.50 ± 0.05 μm and 0.45 ± 0.05 μm for grating pitches of 450 nm, 425 nm, 400 nm, 375 nm and 350 nm respectively. The different filling fractions of our samples, that perturb the SPP wavelength within few a percent, can not explain the large deviations we observe.

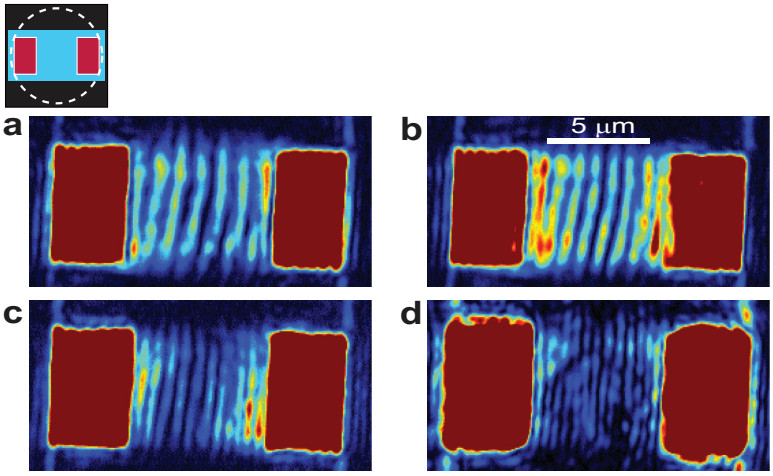

Figure 3.4: *SPP fringe formation via counter propagating waves. The inset shows the image geometry and the incident amplitude profile. The polarization of the incident light is horizontal. (a-d) we observe different SPP fringe patterns for array periods of 375 nm (a), 400 nm (b), 425 nm (c) and 450 nm (d). Clearly the fringe spacing is dependent on the array period.*

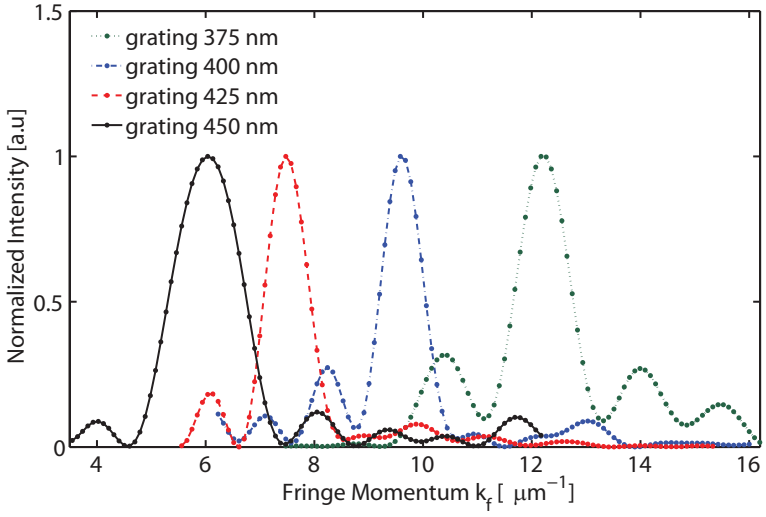

Figure 3.5: *Line Fourier transforms of the fringe patterns observed in Fig. 3.4.*

3.6 Interpreting the fringes

We attribute the fringe patterns to a mixing of the original SPP wave with the hole array [114]. We can analyze the results using a one dimensional model because for all our samples we observe only horizontal propagation. Theoretically there are two ways to mix SPPs with the hole array: intensity mixing (expected for incoherent forms of scattering such as fluorescence) and field convolution (expected for coherent scattering processes). We will discuss both ways even though the experimental observations confirm only the field convolution.

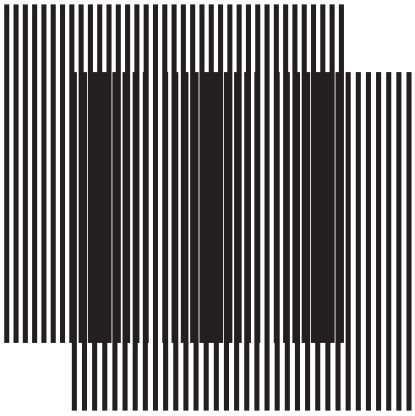

Figure 3.6: *Moire pattern. The superposition of two gratings having a small difference in their periodicity results in the formation of a third grating (the Moire grating).*

3.6.1 Option 1: Moire SPP fringe patterns

We first consider intensity convolution: a SPP standing intensity pattern with momentum $2k_S$ is formed, but since we observe the pattern through the scattering of a periodic structure with momentum k_G, the fringe momentum appears to be $2k_S \pm k_G$. This intensity convolution does not match the experimental observations.

An example of Moire pattern is shown in Fig. 3.6. By overlapping two distinct gratings having slightly different period a Moire pattern appears with a typical larger period.

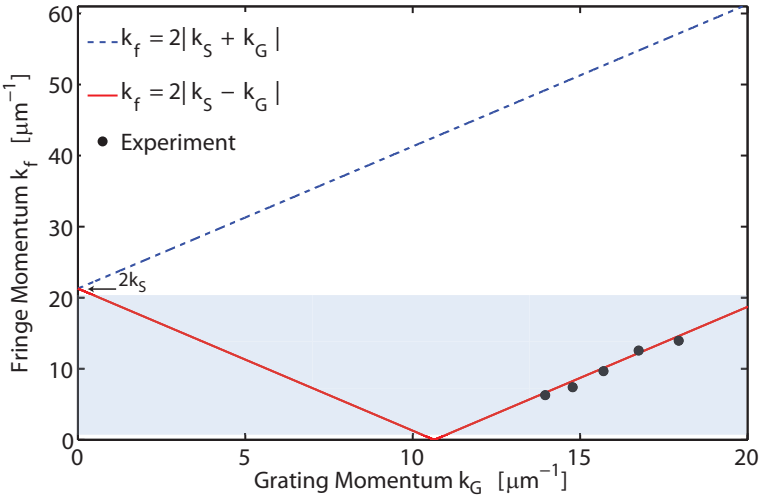

Figure 3.7: *SSP fringe momentum versus the grating momentum. The experimental data shows SPPs convoluted with the $m = -1$ Bloch mode of the arrays. The other Bloch modes can not be resolved due to limited detection bandwidth (light blue square).*

3.6.2 Option 2: Counter propagating Bloch modes

The situation is completely different for the field convolution: the hybridization of the bare SPPs with the Bloch modes of the array results in dressed plasmonic (DP) waves of momentum $k_S + m \cdot k_G$ (m integer). These DP waves then result in standing intensity patterns of momentum $2(k_S + m \cdot k_G)$.

A comparison between experiment and the amplitude convolution approach for these DP waves is shown in Fig. 3.7. The modulus of the fringe momentum (k_f) is plotted against the modulus of the grating momentum (k_G). The two lines are the theoretical predictions for SPPs convolved with the first positive ($m = 1$) and the first negative ($m = -1$) grating orders. without adjustable parameters, the experimental data perfectly follow only the $m = -1$ curve. The first positive order is not observed in our far field measurement due to its evanescent non-radiative nature and the limited resolution of our setup. The distribution of fringe momenta can be expressed except for a normalization factor as

$$P_f(k) = B(k) \sum_{m \in \mathbb{Z}} \eta_m \cdot \delta\left(k - 2\,|k_S + m k_G|\right), \tag{3.2}$$

where every delta represents the standing pattern from one of the m orders

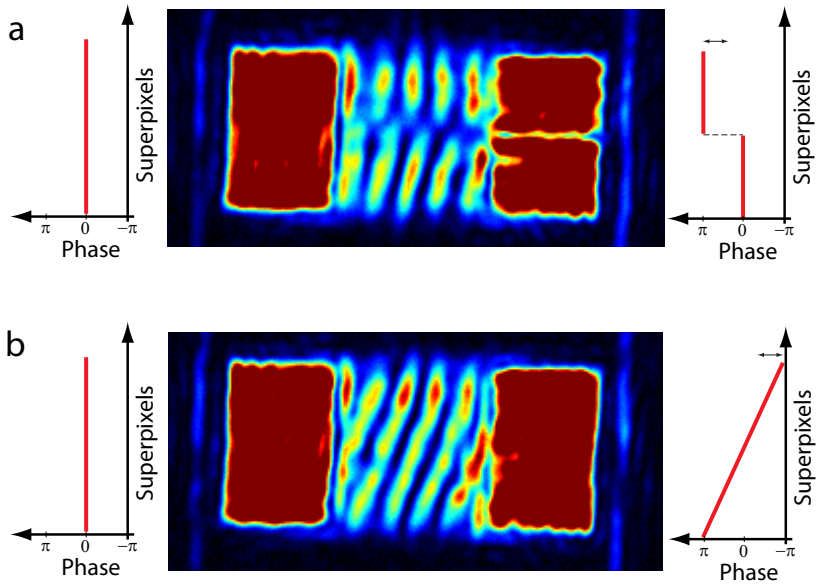

Figure 3.8: *Scanning the fringes by phase tuning. (a) The phase of the left "on" area is kept constant while the phase of the right "on" area has a step jump between the lower and upper part as shown in the wings of the figure. The resulting fringe pattern in the upper part is shifted compared to the lower one. (b) The fringes are rotated due to a linearly incrementing phase on the right "on" area.*

of the array, η_m represents the coupling efficiency of SPPs into this m^{-th} order and $B(k)$ is the momentum bandwidth of our detection optics. Our bandwidth is shown as the light blue rectangle in Fig. 3.7 and we approximate it with a step function limited by the optical diffraction limit and the SPP field of view (the distance between the two "on" areas). Upon inserting this bandwidth in Eq. (3.2) only SPP hybridization with the $m = -1$ term survives because all other DP modes have fringe momentum that exceeds the diffraction limit.

3.7 Amplitude and phase control

Finally in Fig. 3.8 we show phase control of the propagating Bloch-mode dressed SPPs. As an important example we chose to scan and tilt the fringe pattern in a deterministic approach as required for a plasmonic analog of structured illumination microscopy. Furthermore in this analogy, the pre-

dicted high momentum Bloch modes will act as the nonlinear terms of Saturated Structured Illumination Microscopy [56].

We can scan the fringe pattern across the sample by varying the phase delay between the two "on" areas and thus introducing an optical retardation that will translate the DP fringes. We experimentally prove this phase scanning principle for the $m = -1$ DP modes as shown in Fig. 3.8a where the upper half of the right"on" area is out of phase with the rest of the illuminated areas. The different phase delays result in a translated fringe pattern in the upper part. The line scan resolution (fringe translation) is given by our digital phase control: 256 steps from 0 to 2π phase delay. In alternative, by applying a linear phase difference between the two "on" areas, the standing pattern will result in tilted plasmonic fringes (angular scan) as shown in Fig. 3.8b.

The predicted presence of the $m = 1$ DP mode, which represents a sub 100 nm period intensity beating on top of the observed fringe pattern, combined with our ability to scan the pattern across the sample, suggest interesting prospects for subwavelength imaging. Due to the very weak signal of the mode (relative to $m = -1$) and to the diffraction limit we can not resolve this fast beating in the current experimental configuration. However, it should be possible, using near field imaging and optimizing the sample for a maximal value of $\eta_{m=1}$, to calibrate this sub 100 nm intensity pattern for different fringe patterns (line and angular scans). Once calibrated, the sample surface could be used to image sub 100 nm objects with only far field probing and image correlations.

3.8 Conclusion

We have shown here the observation of Bloch-mode dressed surface plasmon polaritons (DP) propagating on nanohole arrays of different subwavelength periodicities. We recorded the standing intensity pattern of two counter propagating DP waves. The dependence of the measured fringe period on the period of the nano structure is perfectly described by a simple model of plasmonic Bloch mode interference. By actively imposing well programmed phase relations to these plasmonic Bloch modes we achieved full and all optical control of their interference patterns. Bloch dressed SPPs are 2D propagating waves that can achieve high momentum and thus actively controlling their interference patterns has potential for lithography, super-resolution biosensing and imaging applications.

3.9 Acknowledgments

We thank Hans Zeijlermaker and Dimitry Lamers for sample fabrication. This work is part of the research program of the “Stichting voor Fundamenteel Onderzoek der Materie”, which is Financially supported by the “Nederlandse Organisatie voor Wetenschappelijk Onderzoek”.

CHAPTER 4

SCANNING PLASMONIC MICROSCOPY

Here we demonstrate a novel Surface Plasmon Polariton (SPP) microscope which is capable of imaging below the optical diffraction limit. A plasmonic lens, generated through phase structured illumination, focusses SPP's down to the their diffraction limit and scans the focus with steps as small as 10 nm. This plasmonic lens is implemented on a metallic nanostructure consisting of alternated hole array gratings and bare metal arenas. The nanostructure has two uses: its hole gratings provide the light-to-SPP coupling while the bare metal arenas provide the focusing/scanning area of the plasmons. The resolution is determined with scattering holes on the bare metal arenas. Because the propagation of SPPs on bare gold is non radiative, only light from the scattering holes is recorded thus allowing us to determine their relative location on the nanostructure. The resolution is determined by the scanning SPP focus, independent of the detection optics. This novel technique has potential for biomedical imaging microscopy, surface biology and functionalization chemistry.

4.1 Introduction

Optical microscopy provides images of a specimen via its interaction with light. The smallest features resolved with conventional microscopy are at best in the range of the optical wavelength λ and subject to the diffraction limit of the optics. To reveal the underlying information inside λ^3 volumes, a number of techniques have been proposed [115, 116]. Near-field microscopy employs scanning nanoprobes either in collection or scattering mode to achieve better resolution [3, 117, 118]. In [119] fluorescence microscopy the improvement exploits special qualities of the labels like fluorescence saturation [120, 121] or stochastic emission [122, 123]. Because most of the interactions and exchanges between living cells and the surrounding environment happen at the surface, surface specific microscopy is of crucial importance for biology and medicine as well as for nanotechnology. Total internal reflection microscopy (TIRFM) is a widely used technique that uses evanescent waves to achieve surface-only imaging [124].

Plasmonic microscopy is a novel concept of microscopy [77, 108, 109] via the excitation of evanescent waves on metallic nanostructures. Surface Plasmon Polaritons (SPP) are surface waves bound to metal-dielectric interfaces. The major advantage of SPPs is that, for a fixed light frequency, the wavelength of these waves is shorter than that of free propagating photons in the same dielectric [41, 44, 43]. Thus, plasmonic microscopy offers not only evanescent out-of-plane resolution (similarly to TIRFM), but also offers large potential for in-plane super resolution.

The main barrier for plasmonic microscopy is the impossibility to use plasmon optics [125] for detection: the read out is always optical. Wide-field plasmonic excitation from a SPP plane wave yields an image that is limited in resolution by the detection optics.

Super resolution is achievable provided that plasmon optics are used to provide tightly confined excitation (e.g. SPP diffraction limited focus) in a scannable way. Advances in nanofabrication allow for the use of nanostructures to manipulate SPPs [82, 83, 84]. But these methods have tiny fields of view, and are thus more suitable for sensing than for microscopy. Recent theoretical [104, 105, 87] and experimental [111, 112] developments have shown the potential of plasmonic phase structuring for 2D surface microscopy. Nevertheless, due to intrinsic problems of these techniques (resolution, field of view or speed), super resolution plasmonic microscopy still has to be implemented.

4.1.1 Our contribution

We demonstrate here the first plasmonic microscope performing at the SPP diffraction limit by imaging scatterers on top of a metallic microscope slide. Specifically, we show that by using phase-structured illumination from a spatial light modulator (SLM) we can both focus and scan SPP's below the optical diffraction limit. The size of the SPP focus is given by the plasmonic diffraction limit which, for a fixed photon frequency, is smaller than the optical diffraction limit. The combined system of the nanostructure with the phase-structured illumination can be thought of as a deformable plasmonic lens. Due to the simplicity of our metallic microscope slide we can calculate the required phase profile for focusing of our plasmonic lens without the necessity of feedback loops. This deterministic approach allows for fast scanning with steps as small as 10 nanometers, and thus microscopy. The imaging resolution is determined by the SPP wavelength supported by our metallic microscope slide. Upgrading the microscope slide, for example by using a multilayered metal-insulator-metal film, opens up potential for a new range of high resolution imaging. Furthermore, because fast SLM devices with megapixels have recently become available, parallel processing of multiple foci might be achievable at video rate and without any resolution loss.

4.2 The working principle

The requirements for a SPP microscope are: (1) to control the amplitude and phase of SPPs locally on the surface of the sample, (2) to create and 2D raster scan a plasmonic focus without feedback, and (3) to provide a consistent and reproducible image of the sample surface.

4.2.1 Experimental configuration

To satisfy our first goal we image a Spatial Light Modulator (SLM) onto the surface of the sample thus mapping each unit cell (pixel) of the SLM to a corresponding area on the sample. The imaging system and its design have already been reported in chapter 2. Amplitude and phase control of the SLM is achieved by grouping pixels into superpixels. We independently control amplitude and phase of 32×32 superpixels. The image of each superpixel (nearly 450 nm with a 650 times demagnifying imaging system) locally excites surface plasmon waves due to periodic corrugations on the

sample [126]. These waves propagate along the surface of the sample and emit photons when encountering scatterers (like nanoparticles or fluorescent molecules). Finally, the surface of the sample is imaged onto the sensor of a CCD camera revealing these ejected photons.

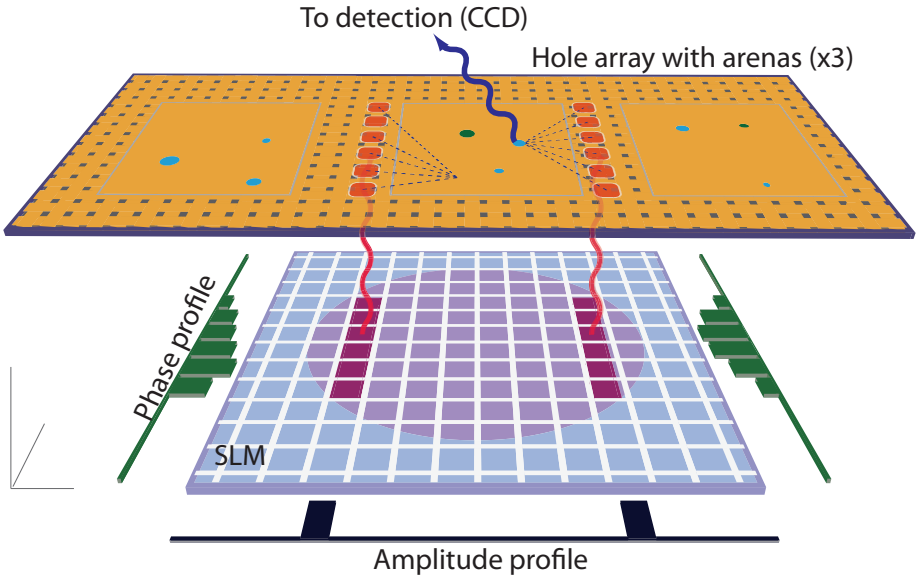

Figure 4.1: *Working principle of the SPP microscope. The Spatial Light Modulator (SLM) is illuminated with a large laser beam (the translucent red circle) and is imaged onto the surface of a nanostructure metallic film. The nanostructure, imaged onto a CCD, is a hole array grating with arenas. The arenas consist of bare metal with few scatterers (the circles). Only two pixel lines of the SLM have nonzero amplitude (amplitude profile). These bright pixels, when imaged onto the grating lines adjacent to the arena, locally generate SPPs that propagate into the middle arena. The arena's flatness allows us to predict the phase profile for SPP focusing (dashed lines) without the necessity of a feedback loop. Photons are detected only when the SPP hit a scatterer, thus locating the scatterer. A raster scan (2D) of the focus provides a full SPP resolution image of scatterers.*

4.2.2 Deterministic SPP focusing and scanning

To achieve SPP focusing at a chosen location we combined our ability to structure the incident illumination (in this case a He:Ne laser was used)

with a specially designed nanostructure. This configuration is schematically depicted in Fig. 4.1. Two parallel lines of bright pixels (non zero amplitude) are imaged on a specially designed nanohole array to launch SPP waves. These lines, each comprised of 13 superpixels, are our SPP sources. The area between the source lines, which we will call the arena, is free of the grating: it is bare metal with a few scatterers to test the properties of the microscope. The SPP waves inside the arena in which they propagate freely in two dimensions can be described by the well known Hankel function (the equivalent of a spherical wave in 2D). The analytical expression of the Hankel function is known. This knowledge allows us to determine the phases for SPP focusing at any target point inside the arena by evaluating the relative distances target-sources. Furthermore, these SPP waves cannot couple to the far field; only when a scatterer is encountered photons are emitted thus imaging the scatterers. More lines of sources can be used to create multiple foci for parallel imaging of many arenas without any increase in the acquisition time, thus allowing multiplexing.

4.2.3 Hole array with structured arenas

The nanostructure is a metallic nanohole array with a rich electromagnetic behavior [85]. Subwavelength gratings offer potential for super-resolution either for dielectric [86] or metal-dielectric [87, 91] configuration. On the grating, the electromagnetic behavior can be described in terms of a hybrid wave [88] arising from SPPs (majority) and quasi-cylindrical waves [89] (minority). The propagation of quasi-cylindrical waves on bare metal is very short(wavelength). Our samples have been designed so that only SPP waves are observed.

Our substrate is composed of a 200 nm of gold film deposited on top of 1 mm BK7 glass substrate. The array covers an area of 30 $\times$ 30 μm^2 and the hole period (a_0) is 450 nm. Square holes were milled using a focused ion beam with sides of 177 nm. The nanostructure includes four square arenas (5 μm $\times$ 5 μm), each different from the other and all surrounded by the hole array, as shown in Fig. 4.2.

The SPP wavelength at the gold-air interface from incident radiation of $\lambda_0 = 633$ nm is given by

$$\lambda_S = \lambda_0 \mathrm{Re}\sqrt{\frac{\varepsilon_\mathrm{m} + \varepsilon_\mathrm{d}}{\varepsilon_\mathrm{m}\varepsilon_\mathrm{d}}}, \tag{4.1}$$

with ε_m and ε_d the dielectric constants of gold and air, respectively. Using tabulated bulk values for ε_m[53] we found $\lambda_S = 590$ nm (for $\lambda_0 = 633nm$).

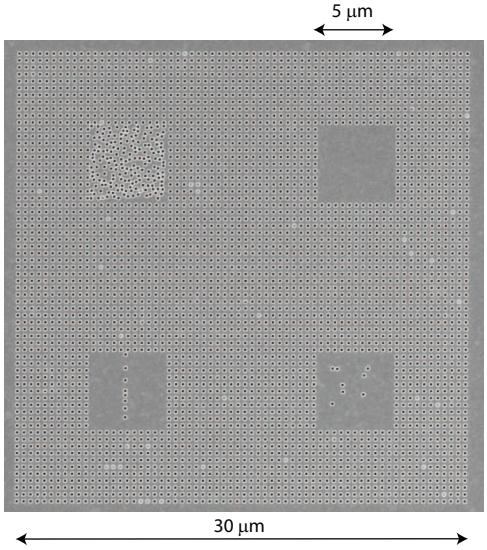

Figure 4.2: *SEM of the nanostructure used in the experiments. The structure (30 μm × 30 μm) is hole array with four square arenas (5 μm × 5 μm). The holes are squares (177 nm × 177 nm) and their period is 450 nm.*

SPP waves are launched from the hole array grating and propagate on the arena. Each arena will be used separately.

4.2.4 Test samples

To test our microscope's imaging ability, two arenas with known structures were prepared. Each arena includes eight scatterers which are nanoholes identical to the ones of the hole array. SEM images of these arenas are shown in Fig. 4.3a-b. The arena of Fig. 4.3a includes randomly positioned holes to test our 2D scanning ability.

The line arena of Fig. 4.3b consists of bare gold with a line of holes. The profile of the line is shown in Fig. 4.3c. The spacing between the holes, defined as the width of the metal stripe between them, is

$$l_{\mathrm{i}} = i \cdot \ 100\ nm, \qquad \forall i\ \epsilon\ 1...7. \tag{4.2}$$

We will use the varying hole spacing in the line arena to determine the resolution of our microscope: if we focus in the space between the holes and if the SPP focus is smaller than the hole spacing, then no photons should be detected.

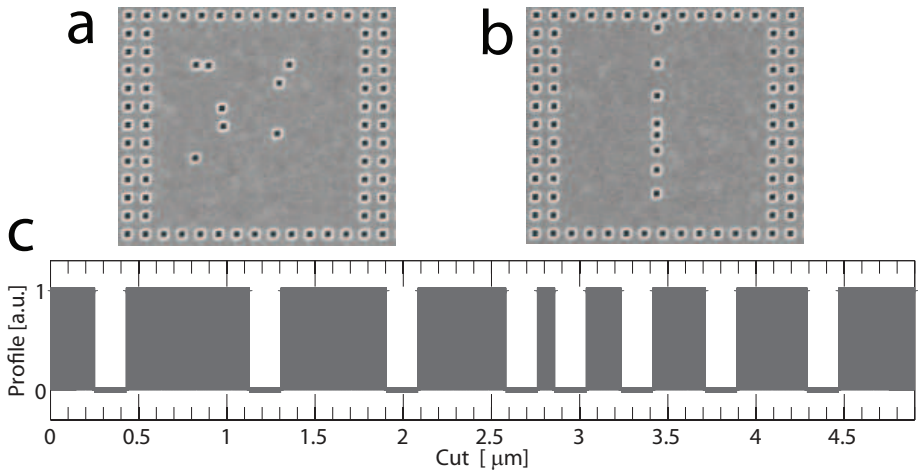

Figure 4.3: *SEM fragment of the arenas to be imaged. (a) Arena with 8 holes located at random positions. This arena will be used to test our ability to scan and image in 2D. (b) Arena with a line of eight holes with linearly increasing separation (metal in between them). (c) Depth profile of the mask used by the focussed ion beam to mill the line of holes of (b). Holes have zero depth.*

Both arenas have a large margin of bare gold between the scatterers and the grating so that only SPP waves are observed (no quasi-cylindrical waves).

4.3 Calibration and implementation

Here we will present reference experiments obtained from a wide field plasmonic microscopy (plane wave SPP illumination). We will show that, because we are using plane wave SPP illumination (no focusing), the imaging resolution is still photon-like diffraction limited. Finally we will conduce preparations for implementing our deformable plasmonic lens, like initializing the SPP sources and calculating their phase for focusing.

4.3.1 Plasmonic plane wave microscopy

Here we image the structure of the line arena using a plane wave SPP illumination. The phase of all superpixels are set to the same value yielding a SPP wave propagating on the arena. The scatterers are excited from this SPP plane wave (wide field illumination). The scattered light is recorded on

a single CCD image (single-shot) determining the location of the scatterers. Results from this wide field SPP illumination (which will be later used as a reference)are shown in Fig. 4.4. Two lines of SPP sources with flat phase are

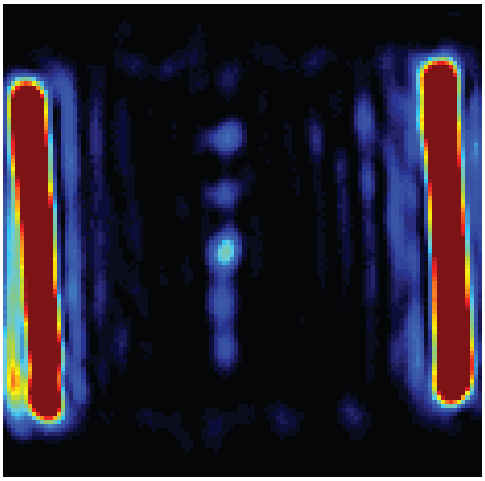

Figure 4.4: *Imaging the line arena without SPP focussing. Two illumination lines are located next to the borders of the line arena of Fig.4.3a. The phase is constant (line wave illumination). SPPs propagate into the arena but photons are ejected only when a scatterer (hole) is encountered. The resolution of this image is completely independent of the SPP wavelength due to the lack of plasmonic optics.*

placed on the opposite sides of the arena. The SPP plane wave propagating inside the arena is invisible (it cannot radiate) except for when it is scattered by the holes. In such a way the single-shot image of the holes, Fig. 4.4, is taken. The imaging resolution of this wide field SPP microscope is still photon-like diffraction limited: because the SPP illumination is not focused the resolution of such an image is fully determined by the detection optics and the photon wavelength. In principle the image remains unchanged for any given SPP wavelength, no matter how small. The resolution can improve depending on the SPP wavelength only by using plasmon optics, thus by creating and scanning a focus.

4.3.2 Initializing the SPP sources

To calculate the required phases for focusing at a chosen target point, the distance of all sources from the target must be known. In order to find

these distances we define a coordination system based on the CCD's pixels coordinates. Because of the magnification of our detecting system, each pixel corresponds to 64 nm on the sample. To determine the location of the sources we load them (turn them "on") one by one, as illustrated in Fig. 4.5a-c for three sources. For this figure, extra white light illumination is used to observe the arena (but not for the initialization process).

Once a single source (S_n) is loaded, we associate its position with the maxima of the CCD image: the source location, $\mathbf{r}_\mathrm{n}$, is the maxima's position. We iterate this initialization procedure for all the 26 sources (2 lines of 13) of the amplitude mask.

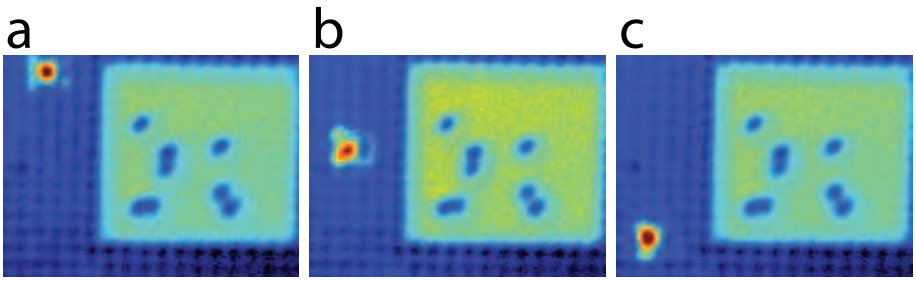

Figure 4.5: *Determination of source's positions. Each source is loaded separately in absence of the other ones. The maxima of the picture (it's position) locates the source. (a)-(c) Three sources loaded in series. For showing the relative position of the sources in respect to the arena, the arena is also illuminated with white light.*

4.3.3 Calculation of the phases for focusing

After the initialization procedure, we have located all sources at positions (CCD coordinates)

$$\mathbf{r}_\mathrm{n} = (x_\mathrm{n}, y_\mathrm{n}) \qquad \forall n \,\epsilon\, 1...26. \tag{4.3}$$

With these source positions we calculate the required phases $\widetilde{\phi}(\mathbf{r}_\mathrm{n}, \mathbf{r}_0)$ for focusing the SPPs at an arbitrary target point at position $\mathbf{r}_0 = (x_0, y_0)$. The Green's function connecting the source to the target, $g(\mathbf{r}_0, \mathbf{r}_\mathrm{n})$, is given by the Hankel function $H_0^{(1)}(K_S r)$ with K_S ($K_S = k_S + i2/L_S$) the complex valued SPP momentum

$$g(\mathbf{r}_0, \mathbf{r}_\mathrm{n}) = H_0^{(1)}(K_S r_{0,n}) \approx \sqrt{\frac{2}{\pi r_{0,n}}} \exp\left[i(K_S r_{0,n} - \pi/4)\right],$$
$$r_{0,n} \equiv |\mathbf{r}_0 - \mathbf{r}_n| = \sqrt{(x_0 - x_\mathrm{n})^2 + (y_0 - y_\mathrm{n})^2}. \tag{4.4}$$

This Green's function is fully determined once the source-target distance ($R_{0,n}$) is known. For focusing, the fields from different sources have to be in phase with each other at the target location. To achieve this phase alignment, the loaded phase (via the SLM) of any source must compensate the phase delay introduced by the relative Green's function

$$\widetilde{\phi}(\mathbf{r}_\mathrm{n}, \mathbf{r}_0) = -\arg\left[g(\mathbf{r}_0, \mathbf{r}_\mathrm{n})\right] = -k_S r_{0,n} = -\frac{2\pi}{\lambda_S} r_{0,n}. \tag{4.5}$$

The phase $-\pi/4$ in the exponent of the right side of eq. 4.4, constant for all sources, is removed from Eq. (4.5) as part of a global phase offset (only phase differences are relevant).

4.4 SPP microscopy via focusing and scanning

To implement the scanning of the focus (required for imaging) we repeat the calculation for a 2D grid of target point. A typical grid of 100 $\times$ 100 target points, while covering the entire 5 μm $\times$ 5 μm arena, provides a step-scan resolution of 50 nm. This series of simple calculations allows us to separately focus SPPs at points which are up to few nanometers far from each other.

4.4.1 2D imaging of the random arena

Our main result, two dimensional imaging using the new scanning plasmon microscope, is shown in Fig. 4.6a. A single point of the image is acquired by focussing SPP at the target point having coordinates (x_0, y_0) and reading out only the CCD intensity of the pixel corresponding to the same coordinates. The full image is acquired by raster scanning the focus: the fast axis along the focal line (focal plane in 3D). The scan step is 16 nm. For comparison, an image of the same structure obtained with white light illumination is shown in Fig. 4.6b. At first glance it is already clear that the plasmonic image of the structure is sharper and better resolved than the white light one.

The overlap between the SEM image (transparent) of the structure and the plasmonic image is shown in Fig. 4.6c: the two images match correctly.

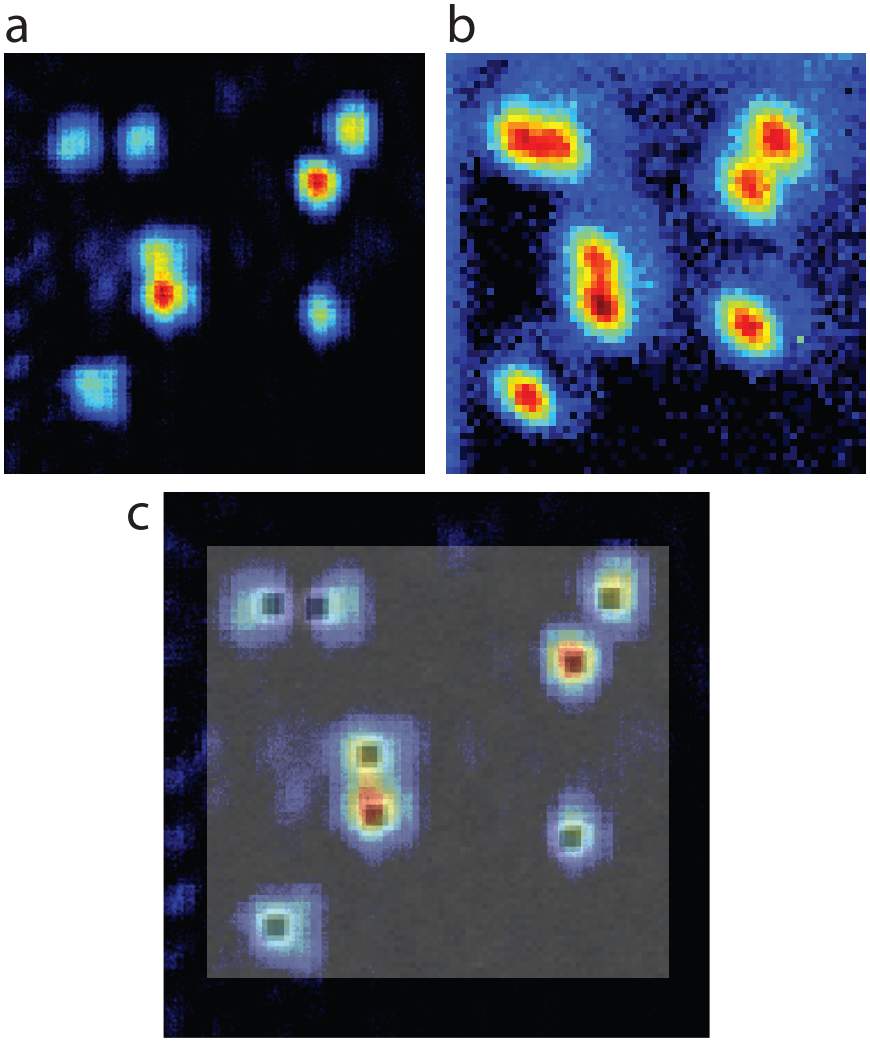

Figure 4.6: *Imaging the nanostructured arena. (a) Accumulative 2D image of the arena achieved via scanning the SPP focus. Only when the SPP focus encounters a scatterer photons are detected. (b) Arena imaged with white light illumination. (c) Comparison between (a) and the SEM image of the structure (Fig. 4.3a).*

There are few deviations (upper left corner). One reason for deviations is that two nearby scatterers screen each other from the plasmon sources (left and right of the image). Nevertheless, those two scatterers are better resolved than in the white light image. To estimate the focal size of the

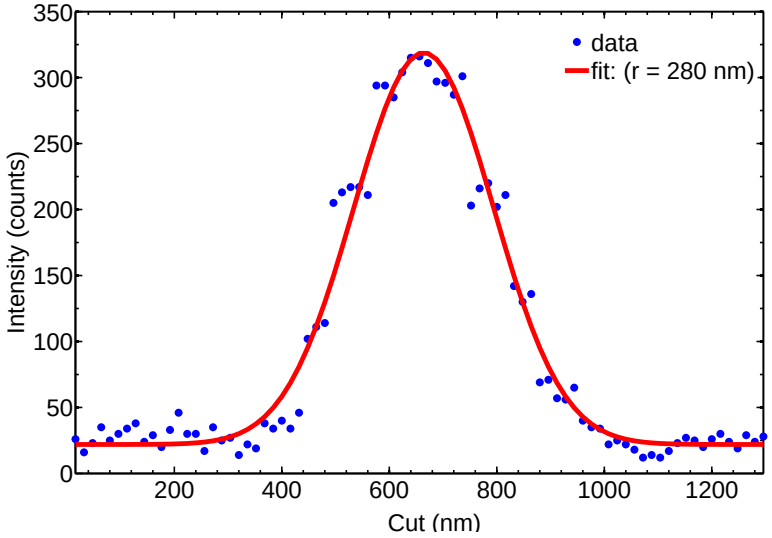

Figure 4.7: *Evaluation of the SPP focus size. The data are a cut of Fig. 4.6a restricted to a single hole. This observation is the convolution of a gaussian SPP focus with the hole profile (known by design). We fitted the data with a fixed hole profile to determine the SPP gaussian spot (FWHM of 280 nm)*

SPP spot we fitted a gaussian to the line cut of the collected intensity of best resolved holes (Fig. 4.7). The geometrical size of the hole is known from the SEM image. The optical profile (lateral cut) is the result of a convolution of the geometrical profile of the hole with our gaussian SPP focus. From the fit we determined for the SPP focus a FWHM (full width at half maximum) of 280 ± 30 nm, in agreement with the SPP diffraction limit ($\lambda_S/2$). The optical diffraction limit of our objective lens is 430 nm for the HeNe wavelength ($\lambda_0 = 633$ nm). In principle the SPP numerical aperture can be improved to include all possible angles by using four lines of sources in square geometry.

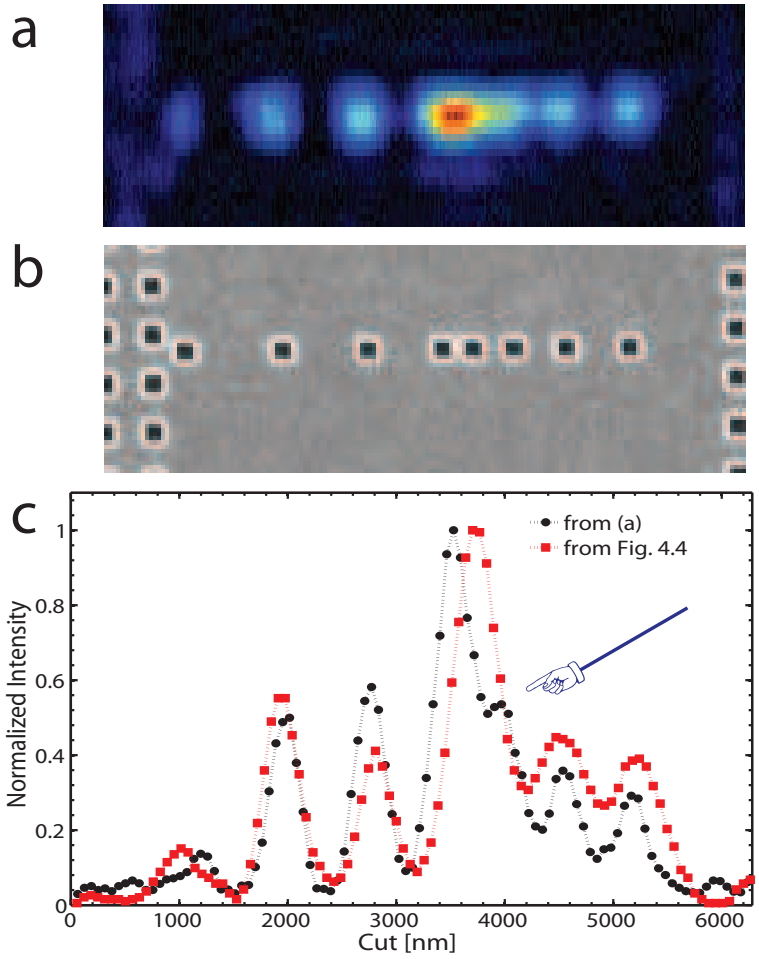

Figure 4.8: *2D imaging of the line arena. (a) Image aquired with our new method. (b) SEM fragment of the arena shows that all scatters are resolved except for the two closest ones. (c) Cut of image (a) and comparison with a cut achieved without SPP focusing (Fig.4.4). The holes separated by 100 nm gold are unresolved, while the shoulder next to the high peak resolves the ones separated by 200 nm gold (only for the focussing and scanning image). This shoulder is indicated by the pointer.*

4.4.2 Imaging the line arena

To better characterize the resolving power of our plasmonic scanning microscope we imaged with a 64 nm step scan (corresponding to one CCD pixel) the structure of the line arena. Because for this arena the line of scatterers is parallel to the source lines, two nearby scatterers cannot screen each other. In other words: SPPs propagating along the lines that connect the sources to a scatterer do not encounter any other scatterer. Thus, for this arena, screening or shadowing among scatterers is avoided.

Results for this structure are shown in Fig. 4.8. The 2D SPP focusing image, shown in Fig. 4.8a, perfectly matches the structure of the arena. In Fig. 4.8b we show for comparison the SEM image of the same structure. Our focusing and scanning image is sharper than the image obtained with plane wave plasmon illumination (Fig. 4.4). The fundamental difference between these two images is that, even though both of them are detected with the same optics, Fig. 4.4 is photon-like diffraction limited and Fig. 4.8a is plasmon-like diffraction limited.

For quantitative comparison of these two images we plot in Fig. 4.8b one dimensional line cuts along the line of holes. Because the SPP wavelength ($\lambda_S = 590\ nm$) is only few percent shorter than the vacuum wavelength ($\lambda_0 = 633\ nm$), the cuts seem similar at first glance. The two holes separated by 100 nm gold are unresolved with both methods, as seen by the high central peak. A separation of 200 nm is still not fully resolved. However, the shoulder right of the main peak is a clear indication of the higher resolving power of our novel microscope. Such shoulder is unresolved by the Rayleigh criterion (standard diffraction limit) but is considered resolved by the Sparrow criterion which requires a local minima.

4.5 Interpretation and discussions

Now we will show calculations related to the point spread function (psf) of our 2D imaging technique and how this psf depends on the read out method. Different readout methods will be compared theoretically and our experimental readout method will be justified as the best method. Finally we will calculate the intensity distribution in the arena and will test the robustness and consistency of the microscope.

4.5.1 Point spread function (psf)

A microscope's resolution is fully characterized by its point spread function. The psf is the image created by an ideal point source. For a standard objective lens the psf at the focal plane $h(\mathbf{r})$ is an Airy disk, which can be approximated by a 2D gaussian profile. The FWHM is determined by the optical numerical aperture of the lens. Our detection objective has a NA=0.9 yielding a diffraction limit of 430 nm ($\lambda_0 = 633nm$).

For the SPP microscope the psf, $h_S(\mathbf{r})$, is a combination of the SPP excitation $f(\mathbf{r})$ and detection $h(\mathbf{r})$ point spread functions. A point source $\delta(\mathbf{r})$ in the origin of the coordinates is illuminated with SPP excitation $f(\mathbf{r}\text{-}\mathbf{r}_0)$ focused at $\mathbf{r}_0$. Optical detection yields for the full CCD intensity

$$I^0_{CCD}(\mathbf{r}) = [f(\mathbf{r}\text{-}\mathbf{r}_0)\delta(\mathbf{r})] \otimes h(\mathbf{r}) = f(\text{-}\mathbf{r}_0)h(\mathbf{r}). \tag{4.6}$$

Here we consider three relevant experimental means of plasmon illumination and optical detection. Each of these combinations gives different values for the SPP microscope point spread function $h_S(\mathbf{r})$ and thus the resolution. These three are (1) wide field plasmon illumination with single shot optical imaging, (2) scanning focused plasmon illumination with integrated intensity optical collection, and (3) scanning focused plasmon illumination with optical collection at the expected focus. We will call these readouts: single shot (1), integrated intensity (2), and pixel intensity at the SPP focus (3). The experiments shown before were performed using the pixel intensity at the SPP focus.

The psf for single shot imaging is given by Eqs. (4.7a-b). The psf of this single shot read out is the detection psf which is independent of the plasmonic illumination wavelength. This read out does not improve the resolution beyond the detection optics as was shown experimentally in Fig. 4.4.

$$I_{S,1}(\mathbf{r}) \equiv I^0_{CCD}(\mathbf{r}) = f(\text{-}\mathbf{r}_0)h(\mathbf{r}); \qquad \forall \mathbf{r}, \tag{4.7a}$$

$$\Rightarrow \quad h_{S,1} = h. \tag{4.7b}$$

The integrated intensity read out is described in Eqs. (4.8a-b). For every position of the focus we integrate the full CCD intensity. The psf of this read out is the plasmonic psf, $f(\mathbf{r})$, which gives improved resolution along the SPP focal line.

$$I_{S,2}(\mathbf{r}_0) \equiv \int I^0_{CCD}(\mathbf{r})d\mathbf{r} = f(\text{-}\mathbf{r}_0) \int h(\mathbf{r})d\mathbf{r}; \qquad \forall \mathbf{r}_0, \tag{4.8a}$$

$$\Rightarrow \quad h_{S,2} = f. \tag{4.8b}$$

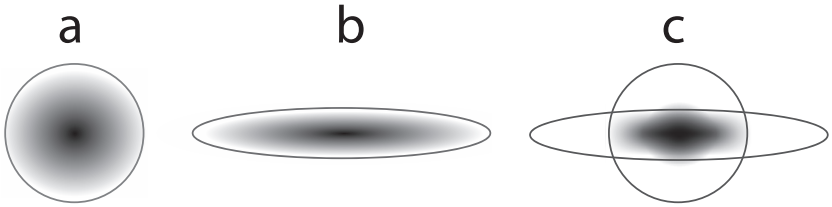

Figure 4.9: *Point spread functions for different read outs. (a) The single shot read out yields the same psf as the detection optics. (b) The integrated intensity read out yields a psf given by the shape of the SPP focus (assumed here to be an ellipse as for a single line of sources). (c) The pixel intensity at the SPP focus yields the optimal read out. The psf is the product of detection and excitation ones.*

The optimal read out method is the pixel intensity at the SPP focus. The psf of this read out is the product of the excitation and detection point spread functions. This psf is the smallest possible.

$$I_{S,3}(\mathbf{r}_0) \equiv I^0_{CCD}(\mathbf{r}_0) = f(\text{-}\mathbf{r}_0)h(\mathbf{r}_0); \qquad \forall \mathbf{r}_0, \tag{4.9a}$$

$$\Rightarrow \quad h_{S,3} = f \cdot h. \tag{4.9b}$$

A cartoon describing the differences of the read out methods is shown in Fig. 4.9. For any given detection and excitation point spread functions, the best achievable combination is the product. For our SPP microscope, such combination is provided via the pixel intensity at the SPP focus read out.

4.5.2 Consistency test with a different intensity read out

The pixel intensity at the SPP focus method was used to obtain (via scanning) the images of the arenas as presented in Figs. 4.6 and 4.8. To form these images, we focused SPPs at one target and acquired only the target pixel intensity ($I_{CCD}(x_0, y_0)$). From every CCD picture only one pixel value was acquired. Thus the imaging quality of the technique strongly depends on creating the focus exactly at the target.

Here we test if the focus is exactly created at the target location. The principle behind this test is the fact that the plasmonic intensity is maximal at the exact focus location. Thus to run the test we will compare the maximal intensity value (only along the focal line) with the intensity value at the presumed focus. If these two values are equal than the test is successful

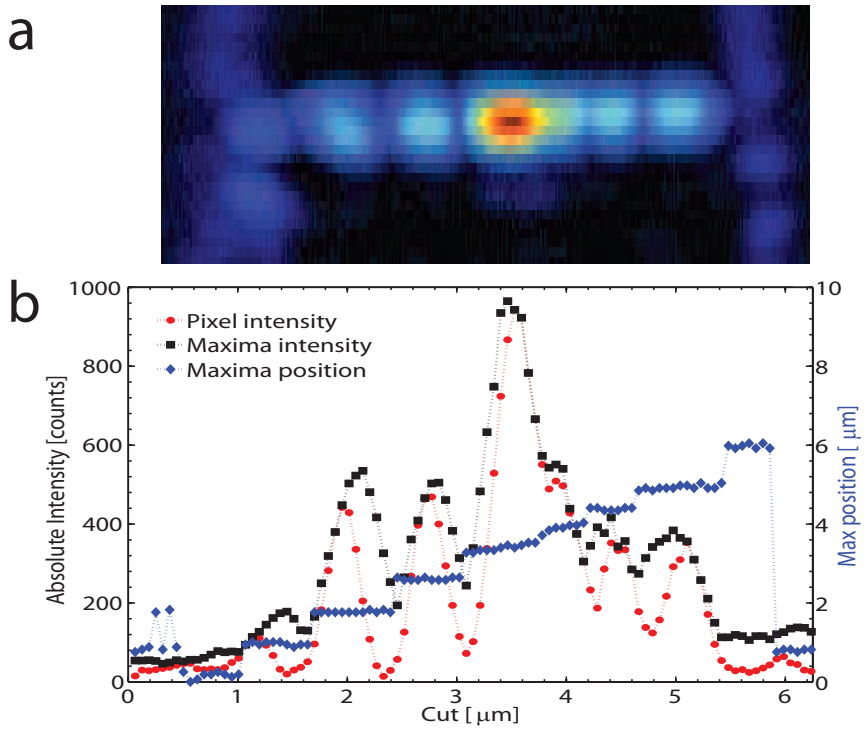

Figure 4.10: *Line arena imaged with the maxima read out. (a) The image is acquired by focusing at a target and reading the maximal intensity along the focal line. (b) Cuts from the maxima read out (black line) and the pixel read out (red line). The pixel read out provides sharper and more correct imaging. The blue line is the location of the maxima: the plateaus are the scatterers.*

meaning that the presumed location and the real location of the focus coincide. Otherwise, phase offsets have to be used to compensate for deviations of the focus location.

The test is experimentally run by acquiring an image of the line arena with a new read out, the maximal intensity read out. When focusing at $\mathbf{r}_0 = (x_0, y_0)$ with the sources along the x axis, the new read out associates to the point $\mathbf{r}_0$ the maxima of intensity along the focal line ($y = y_0$). Mathematically, this maximal intensity read out $I_S(\mathbf{r}_0)$ is

$$I_S(x_0, y_0) \equiv \max \{I_{CCD}(x, y)\}\big|_{y=y_0}. \tag{4.10}$$

Results from this readout are shown in Fig. 4.10a. With this read out

we can test if the calculated focus is really focusing at the target location. In Fig. 4.10b we compare the absolute intensities (cuts) of the maximal read out with the pixel intensity at the focus read out. These cuts nearly coincide in their highest absolute intensity. Thus the test is successful and confirms that, at least for the central holes, focusing is happening at the target location with very high precision.

For holes close to the arena border there are deviations. These deviations are possible border effects due to the structure of the scatterers. The borders of the hole scatter more than the center and thus the maxima always coincides with a border even though the center of the focus might well be on bare gold. The deviations are up to the hole size.

For clarity, the pixel read out is the one that maps the structure with correct dimensions.

4.5.3 Calculated intensity distribution in the arena

Here we will numerically calculate the theoretical intensity distribution in the arena when focusing, thus the SPP point-spread-function. We will use the fact that each source emits spherical waves and the phases of these waves are set to focus at a random point of the arena. Finally, other source geometries that can improve the focusing will be discussed.

The intensity distribution for focusing with the real experimental parameters (two lines of sources) is shown in Fig. 4.11a. As expected, a standing pattern of roughly circular fringes is created with $\lambda_S/2$ spacing. Cuts for the created focus are shown in Fig. 4.11c. The axial resolution is as expected $\lambda_S/4 = 150\ nm$, or half the fringe spacing. The lateral resolution is nearly $\lambda_S/2 = 300\ nm$. This lateral resolution depends on the numerical aperture used to create the focus.

Better focusing can be achieved if we increase the numerical aperture (NA) by adding more sources. For example, in Fig. 4.11b we simulate focusing with four lines of sources in a square geometry. This configuration provides the sharpest focus possible with both axial and lateral resolutions equal to $\lambda_S/4$. By choosing the pixel readout, it is possible to isolate the central peak from the side lobes.

To test the robustness of the focusing procedure, we added phase noise to the intensity distribution Fig. 4.11d. We add a large amount of random noise, $\pm 20\% \cdot 2\pi$, to the ideal phase. The distortions are well contained (comparison with Fig. 4.11a) and the aberrations are minimal confirming that the imaging technique is robust against errors.

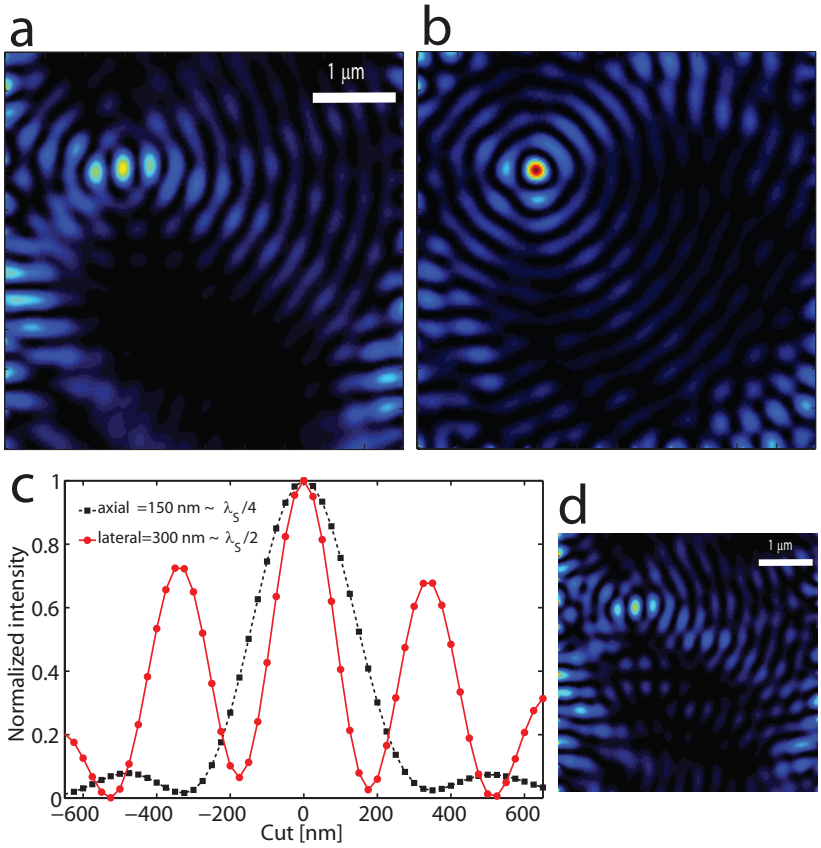

Figure 4.11: *The images are calculated intensity distributions inside an empty arena. The source lines are next to the arena. (a) Two vertical lines of sources create a focus. The lateral and axial resolutions are different. (b) Focusing with four lines of sources results in a sharper focus. The better focussing (FWHM=150 nm; lateral and axial) is due to a maximized numerical aperture (2π). (c) Axial (along x) and lateral cuts of the focus created with two lines of sources (figure a). The axial (lateral) FWHM is 150 (300) nm. (d) In repeating the two line focusing, random phase noise was added (up to 30% of 2π). The focusing is barely distorted yielding that the method is very robust.*

4.6 Conclusions

We show the first imaging technique based on surface plasmon polaritons that provides resolution beyond optical diffraction without near field probing. The technique, demonstrated on single-interface SPPs, is implementable to metal-insulator-metal SPPs that achieve wavelengths ten times shorter than the vacuum one

The novelty of the method is the use of deformable plasmon optics for 2D imaging, which in contrast to previous attempts on SPP microscopy with far field detection, provides resolution dependent on the SPP wavelength. To create the plasmonic lens we use phase structured illumination from a spatial light modulator (SLM) and deterministic (without feedback) calculation of the phases for focussing and step scanning with nanometer precision. Because we use a megapixel SLM, parallel processing of multiple foci is possible.

This new technique offers the potential to revolutionize microscopy, surface biology, and in-vivo medical imaging: Extending the technique with fast spatial light modulators (100 KHz) and short wavelength MIM plasmons enables video rate imaging of millimetric samples with nanoscale resolution.

4.7 Acknowledgments

We thank Hans Zeijlermaker, Dimitry Lamers and Gijs Vollenbrook for sample fabrication. We greatly appreciated discussions and suggestions from Nir Rotenberg and Rutger Meijer Timmerman Thijssen. This work is part of the research program of the “Stichting voor Fundamenteel Onderzoek der Materie”, which is Financially supported by the “Nederlandse Organisatie voor Wetenschappelijk Onderzoek”.

CHAPTER 5

SUMMARY AND CONCLUSIONS

This concluding chapter summarizes all of the results presented in this thesis. We will remind the reader of the principle of our new method to optically control plasmonic fields in metallic nanostructures, as well as its consequences. We will also remind applications of this broad technique to a more specific contest like plasmonic microscopy.

We started this thesis by introducing Surface Plasmon Polaritons (SPP) as surface waves propagating on metal-dielectric interfaces and by describing the main characteristics of these waves. The goal of this thesis was to introduce a new prospective on controlling at will surface plasmons by tuning the incident optical wavefront via a spatial light modulator (SLM).

The concept of this work for successful control of the SPP waves consisted of four main ingredients : (1) Using the pixels of SLM as secondary plasmonic sources, (2) Actively controlling the amplitude and phase of these secondary plasmonic sources, (3) Smart amplitude distribution of the SPP sources to create a plasmonic arena in which optical effects are separated from the plasmonic ones, and (4) Use of the phase of the plasmon sources to, far from the sources, tune the interference pattern of the propagating SPPs. These four points have been satisfied in all the experiments presented in this thesis. In **chapter** 2 we started introducing the new concept of plasmonic control in broad context, while in **chapter** 3 and **chapter** 4 we applied the concept to experiments specifically oriented toward SPP-sample interaction and plasmonic microscopy, respectively.

In **chapter** 2 we introduced this new concept in a relatively large context. The main goal of the experiments in this chapter was to tune the interference pattern of the propagating SPP waves on a nanostructured sample to create a plasmonic focus. The sample used was a nanohole array on a gold film. The hole array was used both for coupling the incident light into SPP sources and for detecting the propagating plasmons via their scattering from the grating. Thus the sample had no particular advantage except for providing the in/out coupling of the plasmons. By tuning the phases of the SLM pixels, we tuned the relative phases of the plasmonic sources. The required phase front to maximize the plasmon intensity in one target spot was determined via a feedback loop. This phase front held important information about the SPP propagation. By focusing at a target, the plasmonic Green's Functions between that target point and the plasmon sources was determined. Such Green's Functions could not be calculated analytically. This focusing (at any given point) and Green's Function retrieval via feedback is a general result valid for any kind of sample. Because the large range of samples where the concept can be applied the results presented in **chapter** 2 are important in a large context.

In **chapter** 3 feedback loops are not used anymore. The plasmonic interference pattern is tuned using only predictable phase patterns. Instead of focusing at will, in this chapter the fringes from counter propagating SPP waves are controlled. Thus, in this chapter, SPP focusing is given up for

simpler and faster control of plasmonic fringes. The main results were the observation of plasmonic Bloch modes due to the mixture of free space (bare gold film) SPP waves with modes of the sample. The samples were nanohole arrays with different hole periodicity. Because of the periodic corrugations of the sample, SPPs were dressed with the Bloch modes of the structure. The momentum of these waves, measured from the standing intensity pattern of two counter propagating Bloch SPPs, perfectly matched our predictions without any fitting parameter. By tuning the phase front it was possible to shift and/or rotate these fringes with relevant consequences for Structured Illumination Microscopy. A new principle was introduced (but not proven): using high momentum Bloch SPP fringes for high resolution structured illumination microscopy.

In **chapter** 4 the best featured of the previous experiments are used to demonstrate the principle of a novel plasmon microscope. In this chapter we achieve again plasmonic focusing and scanning (as in **chapter** 2), but using predictable phase patterns (no feedback used as in **chapter** 3). To combine the best of the two previous experiments we used a specially designed nanostructure consisting of bare gold regions (arenas) surrounded by nanohole arrays. The hole grating provides the light-to-SPP coupling, while the SPP propagation on a bare gold arena is theoretically predictable (free space). SPPs propagating on bare gold are optically invisible because they do not couple out into light. A few nano scatterers were placed in the arena. Using calculated phase values we scanned the SPP focus on the arena to image the scatterers. Because the SPP wavelength is shorter than the optical one, the SPP focus is sharper than the optical focus and the imaging resolution of this plasmon microscope is better than the diffraction limit.

To conclude, in the first part we described in a broad sense (any metallic nanostructure) the principle of optical control of plasmonic channels by focusing and scanning SPPs via feedback loops. Later, in **chapter** 3, we naturally built a bridge between the fundamental results of the first part and the fully application oriented results of the last experiment. A new microscope based on SPP waves was demonstrated.

CHAPTER 6

OUTLOOK AND VALORIZATION

In this chapter we do not provide new experiments or theory. In this chapter we discuss possible application of the results already presented in the previous chapters. We will describe the potential for the plasmonic microscope along with some other potential applications. Part of the information in this chapter has been filed for a patent.

6.1 Introduction

In this chapter we describe ideas for applications based on amplitude and phase structured plasmonic waves. This chapter is divided into two section: (1) description of plasmonic microscopy via SPP structured illumination and via raster scanning of a tight plasmonic focus, and (2) description of general concepts and ideas for new plasmonic applications based on the experiments shown in the previous chapters.

6.2 Plasmonic microscopy

Optical microscopes are powerful investigative tools which are widely spread in hospitals, research labs, and industry. One of the most important specifications of an optical microscope is the resolution. The resolution is determined by the diffraction limit of the optical element (the objective lens). We propose here a plasmonic upgrade to an already existing optical microscope. The core of the upgrade is a nanostructured microscope slide which also acts as a plasmonic lens. Because the wavelength of the plasmons is shorter than the wavelength of the plasmon-exciting light, the plasmonic diffraction limit is smaller than the optical one.

A conventional transmission optical microscope is shown in Fig. 6.1a. In any optical microscope we can distinguish: (1) the light source or illumination part, (2) the sample compartment, (3) the optical element or the objective lens, and (4) the detection part. The sample to be imaged is placed on a microscope slide (a flat glass slab with a standard thickness of 180 μm). The glass slide holding the sample is positioned in the sample compartment of the microscope. The sample compartment contains a diaphragm which allows for the illumination of the sample from below (inset of Fig. 6.1a). The scattered light (or the fluorescence) from the sample is collected with an objective lens. Finally the collected light is recorded on a CCD detector.

Since the invention of the microscope, most of its components have been improved to increase the resolution. Improved illumination has resulted in Structured Illumination Microscopy; improved labeling of the samples has resulted in Fluorescence Microscopy; improved objectives have resulted in high numerical aperture immersion microscopy; improved detection has resulted in confocal and multiphoton microscopy. However, there is one component, the microscope slide, which has remained the same since the microscope creation.

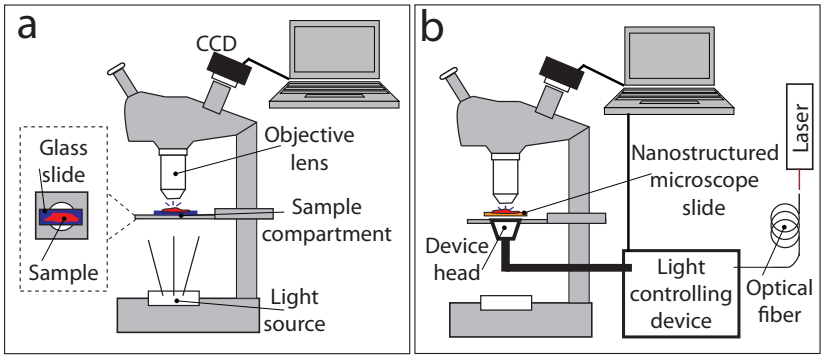

Figure 6.1: *Conventional microscope and plasmonically upgraded microscope. (a) A conventional transmission optical microscope includes the illumination source, the sample compartment where the microscope slide (in blue) containing the sample (in red) is placed, the collection objective, and the detector. The imaging resolution is given by the diffraction limit of the objective lens. The inset shows a top view of the the sample compartment. (b) The plasmonically upgraded microscope includes a light controlling device to shape the wavefront of a coherent laser source. The optical output of the device, the head, is placed in the sample compartment. The 'golden' microscope slide is a metallic nanostructure and is positioned on top of the device's head. Upon properly controlled illumination the 'golden' slides becomes a deformable plasmonic lens (the plasmonic condenser) which achieves tight excitation of the sample and thus high imaging resolution.*

6.2.1 The slide is the lens

We propose an improvement to the microscope slide based on metallic nanostructures (for example Metal-Insulator-Metal planar waveguides) and plasmonics. This 'golden' microscope slide is both the sample holder and a plasmonic lens if properly illuminated. The implementation of this 'golden' microscope slide within a conventional microscope is shown in Fig. 6.1b. The head ending of a light controlling device (which contains a Spatial Light Modulator) is fixed on the sample compartment. The nanostructured sample holder (orange slide in the figure) is positioned on top of the device head. The nanostructure supports plasmonic waves which are controlled or focused by the light controlling device. The combined system consisting of the device and of the 'golden' microscope slide is the plasmonic lens. The working principle of the plasmonic lens has been presented in **chapter** 4. By comparison with the original optical microscope which contains only one lens

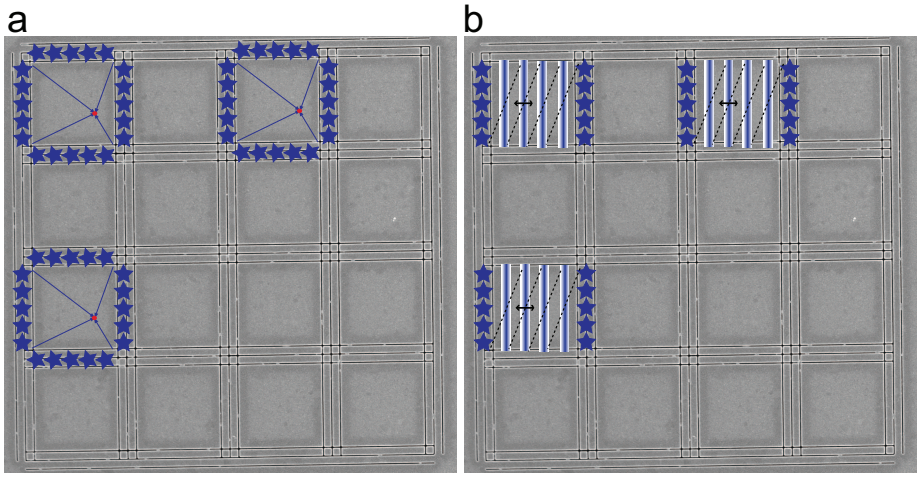

Figure 6.2: *Two modalities of the plasmonic upgrade. The multiplexed nanostructure (SEM image) is a golden film with groves to provide the light to SPP coupling and empty arenas. The sample is placed on top of the structure. (a) Multiplexed focusing and scanning. Four lines of SPP sources (the blue stars) create a plasmonic focus with FWHM equal to $\lambda_S/4$. Multiplexing is achieved by the parallel creation on one focus for each arena (only three foci are shown). The image is acquired by scanning the foci. (b) Plamonic fringe illumination. The sample is illuminated with the standing pattern created from two counter propagating SPP waves. The final image is build by processing many images taken with shifted and tilted fringe patterns. The resolution is proportional to the fringe spacing which is equal to $\lambda_S/2$. Multiplexing of different arenas is possible (shown for three). Both modalities achieve an imaging resolution which is dependent on the plasmonic wavelength.*

(the objective), the plasmonic microscope consist of two lenses (the objective and the plasmonic lens). The performance of an Metal-Insulator-Metal plasmonic lens should be better than that of any objective lens.

6.2.2 Working modalities: (1) focusing and (2) plasmonic fringes

The plasmonic upgrade kit can be operated in two modalities: (1) plasmonic focusing and scanning, and (2) plasmonic structured illumination. Switching between modalities is done via the computer without any mechanical motion. Both modalities are shown in Fig. 6.2 and include a multiplexed configuration

supported by the nanostructured microscope slide.

In the first modality, the sample is excited via a tight plasmonic focus which is raster scanned in 2D. The resolution of the microscope is determined by the size of the SPP focus. For a plasmonic lens created from four lines of SPP sources (maximal NA), as shown in Fig. 6.2a, the FWHM of the focus is a quarter of the plasmonic wavelength. The resolution improvement is due two two factors: the short SPP wavelength and the high NA of the plasmonic lens. The plasmonic upgrade kit also includes a feedback approach to focusing in order to compensate for aberrations.

In the second modality, the sample is excited via standing intensity pattern created from two counter propagating SPP waves, as shown in Fig. 6.2b. The final image is achieved, as for optical Structured Illumination Microscope, by processing multiple images taken with shifted and tilted fringe illumination. The resolution is determined by the fringe periodicity which is half the plasmonic wavelength.

6.3 General ideas for applications

Here we provide qualitative descriptions of these other potential applications. The ideas presented here are based on the results of **chapter** 2 which are are valid for any plasmonic nanostructure because feedback is used to create the desired effect.

6.3.1 Maskless plasmonic lithography

The fabrication of a microchip involves many steps. Lithography is one of these steps and is used for patterning the surface of the chip. The bulk silicon wafer of the chip is coated with a photoresist layer. When the photoresist material is locally exposed to light of short wavelength, typically UV light, the chemical properties of the exposed areas of the photoresist are changed. A chemical bath which specifically binds only to the UV exposed photoresist material, is used to wash away the exposed photoresist from the chip. The empty spaces left after the chemical bath are filled with a new material. The pattern of photoresist exposed to light is controlled by a designed metallic mask, as shown in Fig. 6.3a. The resolution of the pattern is dependent on the wavelength of light: excimer laser at wavelengths of 193 nm are the standard in current technology.

We suggest to use a focused plasmonic beam to imprint the desired pattern in the photoresist with improved resolution. The wafer covered with

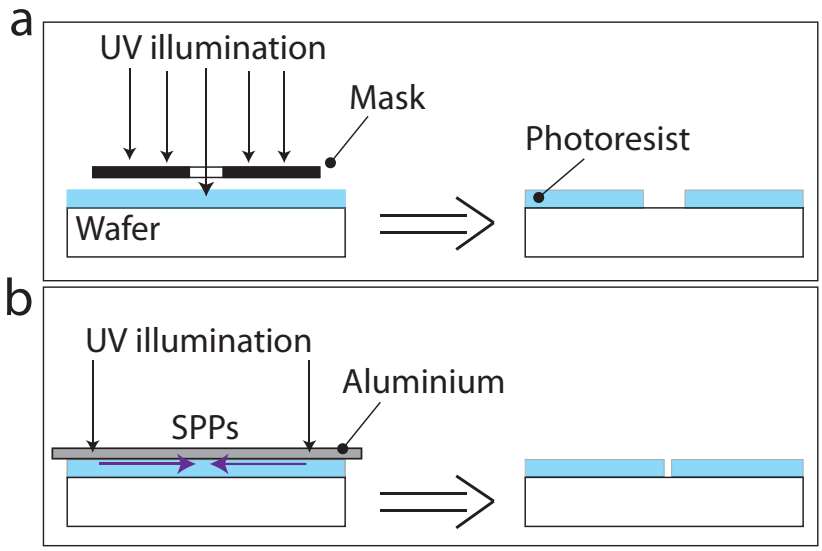

Figure 6.3: *Standard lithography and plasmonic lithography principles. (a) The waver is covered with a photoresist layer. Using a metallic mask, only a portion of the photoresist is illuminated with UV light. After developing the resist with a chemical bath, the exposed portion is washed out. The size of the removed portion is proportional to the UV wavelength. (b) The covered wafer is positioned on top of an aluminium film. UV light incident on the film will launch SPP waves of shorter wavelength than the original UV light. A sharp SPP focus is impressed in the photoresist yielding higher resolution than the direct UV lithography.*

the photoresist is placed on top of metallic film with the metal in photoresist side towards the metal. To use the same UV light (wavelength = 193 nm), metals with very high plasma frequency (short plasma wavelength) have to be used, for example aluminium (Al). The wavelength of Surface Plasmons at the interface between aluminium and the photoresist (n=1.5) excited from UV light (wavelength = 193 nm) is nearly 90 nm, thus four times shorter than the incident wavelength. The resolution of the pattern imprinted in the photoresist with a focused SPP wave of such short wavelength is higher than by the standard UV lithography, as illustrated in Fig. 6.3b.

6.3.2 Focused plasmons for electron-source generation

Using electron beams to generate Surface Plasmons is a well established technique. These electron generated SPPs propagate and radiate light when encountering scatterers or gratings. Thus electrons generate plasmons which generate light. We propose the inverse configuration: high power light pulses couples into SPPs pulses which, if tightly focused in space and time, will locally generate electrons via the photoelectric effect. This inverse configuration is described in Fig. 6.4a.

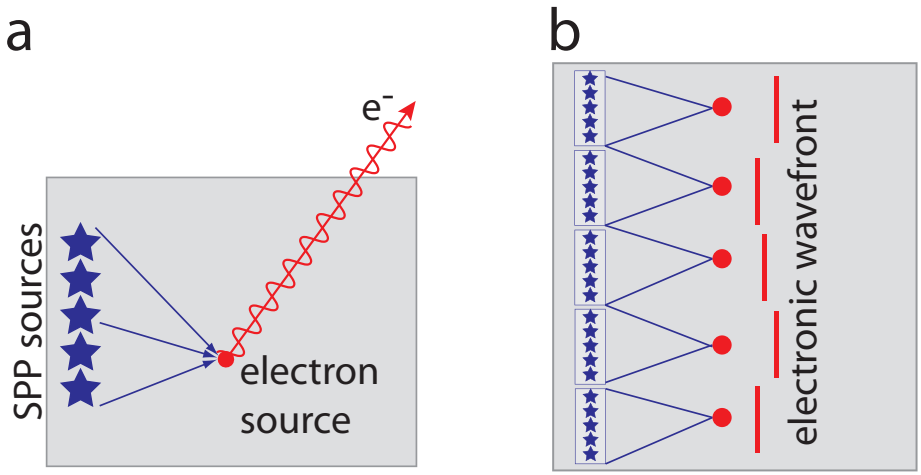

Figure 6.4: *Electron generation from focused SPP waves. (a) Light incident on a metallic nanostructure (grey rectangle) will locally generate SPP waves (the five blue stars) of controllable wavefront. Tightly focused SPP will generate electrons (red circle) at the excamb focus position. (b) Creating multiple SPP foci (from more SPP sources) will result in multiple electron sources. We assume that these are coherent sources. The wavefront of all these electron emitters is controlled via the SPP wavefront which is in turn controlled by the incident optical wavefront. Electron focusing via wavefront shaping is an interesting consequence.*

Because we can focus SPPs at any desired point, we can locate an electron source at any desired point. The size of this electron source is the size of our SPP focus, thus smaller than the size of a focused light beam of the same wavelength. The principle of an electron source via focused SPPs can be extended to multiple sources (from multiple SPP foci) yielding the possibility of electronic Wavefront Shaping, as shown in Fig. 6.4b, if the electron emission is a coherent process.

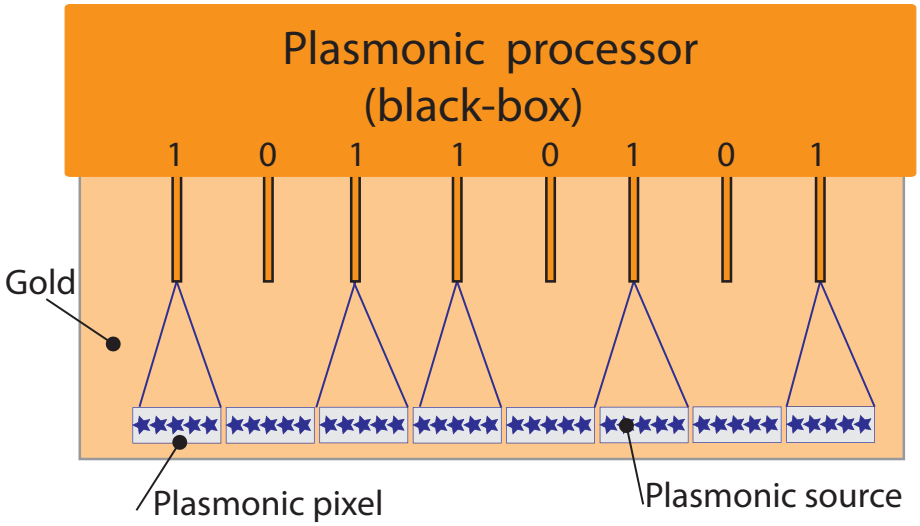

Figure 6.5: *Writing a plasmonic byte of information. Light incident on the gold structure will locally induce plasmonic sources (the stars). The phase of all the plasmonic sources as well as their amplitude is controlled via the incident optical wavefront. The optical wavefront is controlled via a computer. Five plasmonic sources are grouped into a SPP pixel which can either create a SPP focus or not. The foci positions coincide with the inputs (nanowires or nanogrooves) of the plasmonic processor. The processor is assumed to be a black box. By tuning the plasmonic pixels "on" or "off" it is possible to communicate a byte to the processor.*

6.3.3 Writing an plasmonic byte

Optical computing is the discipline that studies the possibility to use coherent light for computers. The calculating time of an optical computer, based on the principles of quantum optics, is exponentially faster that of the standard computer. The core of a standard computer is the processor. We The information to/from the processor is transmitted via electrical contacts (wires). The core of an optical computer is the optical chip. The information to/from the optical chip is transmitted via optical contacts (waveguides). An important category of optical computers is based on plasmonics nanostructures that benefit from the good waveguiding properties of surface plasmons (channel plasmons).

We do not propose an improvement of the plasmonic processor which we consider as a working black box. We propose one way to communicate

with a plasmonic chip using a computer. Thus we propose an interface between electronics, optics and plasmonics. The principle of writing one plasmonic byte is shown in Fig. 6.5. A plasmonic processor is connected to a gold platform via metallic nanowires (or grooves). Light incident on the gold platform will excite plasmons sources. These SPP sources can be tuned to create multiple foci (any desired configuration) in correspondence of the nanowire inputs of the processor. The plasmons propagate along the nanowire waveguide and communicate the information to the processor.

BIBLIOGRAPHY

[1] Archimedes, *Burning ray (translasion from lost greek manuscript)*, Tareq Rajab Museum. Kuwait (902 AD). — p.14.

[2] I. Newton, *Opticks or a treatise of the reflections, refractions, inflections and colours of light*, The Portsmouth Collection. — p.14.

[3] L. Novotny and B. Hecht, *Principles of Nano-Optics*, Cambridge University Press (2006). — p.14 and 68.

[4] M. Born, E. Wolf, and A. B. Bhatia, *Principles of Optics: Electromagnetic Theory of Propagation, Interference and Diffraction of Light*, Cambridge University Press (1999). — p.14.

[5] E. Yablonovitch, "Inhibited spontaneous emission in Solid-State physics and electronics", *Phys. Rev. Lett.* **58**, 2059 (1987). — p.14.

[6] J. E. G. J. Wijnhoven and W. L. Vos, "Preparation of photonic crystals made of air spheres in titania", *Science* **281**, 802 (1998). — p.14.

[7] S. John and J. Wang, "Quantum electrodynamics near a photonic band gap: Photon bound states and dressed atoms", *Phys. Rev. Lett.* **64**, 2418 (1990). — p.14.

[8] S. Noda, M. Fujita, and T. Asano, "Spontaneous-emission control by photonic crystals and nanocavities", *Nat Photon* **1**, 449 (2007). — p.14.

[9] M. Leistikow, A. P. Mosk, E. Yeganegi, S. R. Huisman, A. Lagendijk, and W. Vos, "Inhibited spontaneous emission of quantum dots observed in a 3d photonic band gap", *Phys. Rev. Lett.* **107**, 193903 (2011). — p.14.

[10] J. C. Knight, "Photonic crystal fibres", *Nature* **424**, 847 (2003). — p.14.

[11] S. I. Bozhevolnyi, V. S. Volkov, T. Sndergaard, A. Boltasseva, P. I. Borel, and M. Kristensen, "Near-field imaging of light propagation in photonic crystal waveguides: Explicit role of bloch harmonics", *Phys. Rev. B* **66**, 235204 (2002). — p.14.

[12] D. M. Beggs, T. F. Krauss, L. Kuipers, and T. Kampfrath, "Ultrafast tilting of the dispersion of a photonic crystal and adiabatic spectral compression of light pulses", *Phys. Rev. Lett.* **108**, 033902 (2012). — p.14.

[13] J. B. Pendry, A. J. Holden, D. J. Robbins, and W. J. Stewart, "Low frequency plasmons in thin-wire structures", *J. Phys. Conden. Matter* **10**, 4785 (1998). — p.14.

[14] J. B. Pendry, "Negative refraction makes a perfect lens", *Phys. Rev. Lett.* **85**, 3966 (2000). — p.14.

[15] D. R. Smith, J. B. Pendry, and M. C. K. Wiltshire, "Metamaterials and negative refractive index", *Science* **305**, 788 (2004). — p.14.

[16] V. G. Veselago, "The electrodynamics of substances with simultaneously negative ϵ and μ", *Sov. Phys. Uspekhi* **10**, 509 (1968). — p.14.

[17] D. L. Mills and E. Burstein, "Polaritons: the electromagnetic modes of media", *Rep. Prog. Phys.* **37**, 817 (1974). — p.14.

[18] D. R. Smith, W. J. Padilla, D. C. Vier, S. C. Nemat-Nasser, and S. Schultz, "Composite medium with simultaneously negative permeability and permittivity", *Phys. Rev. Lett.* **84**, 4184 (2000). — p.14.

[19] E. Verhagen, R. de Waele, L. Kuipers, and A. Polman, "Three-Dimensional negative index of refraction at optical frequencies by coupling plasmonic waveguides", *Phys. Rev. Lett.* **105**, 223901 (2010). — p.14.

[20] U. Leonhardt and T. Tyc, "Broadband invisibility by Non-Euclidean cloaking", *Science* **323**, 110 (2009). — p.14.

[21] U. Leonhardt, "Optical conformal mapping", *Science* **312**, 1777 (2006). — p.14.

[22] J. B. Pendry, D. Schurig, and D. R. Smith, "Controlling electromagnetic fields", *Science* **312**, 1780 (2006). — p.14.

[23] H. Chen, C. T. Chan, and P. Sheng, "Transformation optics and metamaterials", *Nat Mater* **9**, 387 (2010). — p.14.

[24] T. W. Ebbesen, H. J. Lezec, H. F. Ghaemi, T. Thio, and P. A. Wolff, "Extraordinary optical transmission through sub-wavelength

hole arrays", *Nature* **391**, 667 (1998). — p.14 and 57.
[25] W. L. Barnes, A. Dereux, and T. W. Ebbesen, "Surface plasmon subwavelength optics", *Nature* **424**, 824 (2003). — p.14, 42, and 54.
[26] S. A. Maier, *Plasmonics: Fundamentals and Applications*, Springer-Verlag (2007). — p.14.
[27] H. Raether, *Surface Plasmons on smooth and rough surfaces and on gratings*, Springer-Verlag (1988). — p.14.
[28] H. A. Atwater, "The promise of plasmonics", *Scientific American* **296**, 56 (2007). — p.15.
[29] T. W. Ebbesen, C. Genet, and S. I. Bozhevolnyi, "Surface-plasmon circuitry", *Phys Today* **61**, 44 (2008). — p.15 and 42.
[30] N. Engheta, "Circuits with light at nanoscales: Optical nanocircuits inspired by metamaterials", *Science* **317**, 1698 (2007). — p.15, 16, and 42.
[31] M. I. Stockman, "Nanofocusing of optical energy in tapered plasmonic waveguides", *Phys. Rev. Lett.* **93**, 137404 (2004). — p.15 and 54.
[32] S. Lal, S. Link, and N. J. Halas, "Nano-optics from sensing to waveguiding", *Nat Photon* **1**, 641 (2007). — p.15.
[33] E. Prodan, C. Radloff, N. J. Halas, and P. Nordlander, "A hybridization model for the plasmon response of complex nanostructures", *Science* **302**, 419 (2003). — p.15 and 42.
[34] H. Cang, A. Labno, C. Lu, X. Yin, M. Liu, C. Gladden, Y. Liu, and X. Zhang, "Probing the electromagnetic field of a 15-nanometre hotspot by single molecule imaging", *Nature* **469**, 385 (2011). — p.15.
[35] P. L. Stiles, J. A. Dieringer, N. C. Shah, and R. P. V. Duyne, "Surface-Enhanced raman spectroscopy", *Annu. Rev. Anal. Chem.* **1**, 601 (2008). — p.15.
[36] C. Loo, A. Lowery, N. Halas, J. West, and R. Drezek, "Immunotargeted nanoshells for integrated cancer imaging and therapy", *Nano Lett.* **5**, 709 (2012). — p.15.
[37] S. Kim, J. Jin, Y. Kim, I. Park, Y. Kim, and S. Kim, "High-harmonic generation by resonant plasmon field enhancement", *Nature* **453**, 757 (2008). — p.15.
[38] P. Spinelli, M. Verschuuren, and A. Polman, "Broadband omnidirectional antireflection coating based on subwavelength surface mie resonators", *Nat Commun* **3**, 692 (2012). — p.15.
[39] R. H. Ritchie, "Plasma losses by fast electrons in thin films", *Phys. Rev.* **106**, 874 (1957). — p.15.

[40] A. V. Zayats, I. I. Smolyaninov, and A. A. Maradudin, "Nano-optics of surface plasmon polaritons", *Phys. Rep.* **408**, 131 (2005). — p.15.

[41] E. N. Economou, "Surface plasmons in thin films", *Phys. Rev.* **182**, 539 (1969). — p.16 and 68.

[42] H. T. Miyazaki and Y. Kurokawa, "Squeezing visible light waves into a 3-nm-Thick and 55-nm-Long plasmon cavity", *Phys. Rev. Lett.* **96**, 097401 (2006). — p.16.

[43] J. A. Dionne, L. A. Sweatlock, H. A. Atwater, and A. Polman, "Plasmon slot waveguides: Towards chip-scale propagation with subwavelength-scale localization", *Phys. Rev. B* **73**, 035407 (2006). — p.16 and 68.

[44] E. Verhagen, J. A. Dionne, L. K. Kuipers, H. A. Atwater, and A. Polman, "Near-field visualization of strongly confined surface plasmon polaritons in metal-insulator-metal waveguides", *Nano Lett.* **8**, 2925 (2008). — p.16 and 68.

[45] K. Watanabe, K. Matsuura, F. Kawata, K. Nagata, J. Ning, and H. Kano, "Scanning and non-scanning surface plasmon microscopy to observe cell adhesion sites", *Biomed. Opt. Express* **3**, 354 (2012). — p.16.

[46] L. Pan, Y. Park, Y. Xiong, E. Ulin-Avila, Y. Wang, L. Zeng, S. Xiong, J. Rho, C. Sun, D. B. Bogy, and X. Zhang, "Maskless plasmonic lithography at 22 nm resolution", *Sci. Rep.* **1** (2011). — p.16.

[47] P. Zijlstra, J. W. M. Chon, and M. Gu, "Five-dimensional optical recording mediated by surface plasmons in gold nanorods", *Nature* **459**, 410 (2009). — p.16.

[48] D. E. Chang, A. S. Sorensen, E. A. Demler, and M. D. Lukin, "A single-photon transistor using nanoscale surface plasmons", *Nat Phys* **3**, 807 (2007). — p.16.

[49] J. A. Dionne, K. Diest, L. A. Sweatlock, and H. A. Atwater, "PlasMOStor: a Metal-Oxide-Si field effect plasmonic modulator", *Nano Lett.* **9**, 897 (2009). — p.16 and 42.

[50] Z. Jacob and V. M. Shalaev, "Plasmonics goes quantum", *Science* **334**, 463 (2011). — p.16.

[51] A. Vakil and N. Engheta, "Transformation optics using graphene", *Science* **332**, 1291 (2011). — p.16.

[52] G. Murgida and M. Castagnino, "A natural normalization for the eigenstates of a hamiltonian with continuous spectrum", *Physica A:*

Statistical Mechanics and its Applications **381**, 170 (2007). — p.18.

[53] P. B. Johnson and R. W. Christy, "Optical constants of the noble metals", *Phys. Rev. B* **6**, 4370 (1972). — p.20, 21, 26, 44, 57, and 71.

[54] M. A. A. Neil, R. Juskaitis, and T. Wilson, "Method of obtaining optical sectioning by using structured light in a conventional microscope", *Opt. Lett.* **22**, 1905 (1997). — p.29.

[55] M. G. L. Gustafsson, "Surpassing the lateral resolution limit by a factor of two using structured illumination microscopy", *Journal of Microscopy* **198**, 82 (2000). — p.29.

[56] M. G. L. Gustafsson, "Nonlinear structured-illumination microscopy: Wide-field fluorescence imaging with theoretically unlimited resolution", *Proc. Natl. Acad. Sci. USA* **102**, 13081 (2005). — p.33, 54, and 64.

[57] I. M. Vellekoop and A. P. Mosk, "Focusing coherent light through opaque strongly scattering media", *Opt. Lett.* **32**, 2309 (2007). — p.34 and 38.

[58] I. M. Vellekoop, E. G. van Putten, A. Lagendijk, and A. P. Mosk, "Demixing light paths inside disordered metamaterials", *Opt. Express* **16**, 67 (2008). — p.34 and 42.

[59] S. Popoff, G. Lerosey, M. Fink, A. C. Boccara, and S. Gigan, "Image transmission through an opaque material", *Nat Commun* **1**, 81 (2010). — p.34.

[60] J. Aulbach, B. Gjonaj, P. M. Johnson, A. P. Mosk, and A. Lagendijk, "Control of light transmission through opaque scattering media in space and time", *Phy. Rev. Lett.* **106**, 103901 (2011). — p.35.

[61] O. Katz, E. Small, Y. Bromberg, and Y. Silberberg, "Focusing and compression of ultrashort pulses through scattering media", *Nat Photon* **5**, 372 (2011). — p.35.

[62] D. J. McCabe, A. Tajalli, D. R. Austin, P. Bondareff, I. A. Walmsley, S. Gigan, and B. Chatel, "Spatio-temporal focusing of an ultrafast pulse through a multiply scattering medium", *Nat Commun* **2** (2011). — p.35.

[63] E. G. van Putten, D. Akbulut, J. Bertolotti, W. L. Vos, A. Lagendijk, and A. P. Mosk, "Scattering lens resolves sub-100 nm structures with visible light", *Phys. Rev. Lett.* **106**, 193905 (2011). — p.35.

[64] X. Xu, H. Liu, and L. V. Wang, "Time-reversed ultrasonically encoded optical focusing into scattering media", *Nat Photon* **5**, 154

(2011). — p.35.
[65] I. M. Vellekoop, A. Lagendijk, and A. P. Mosk, "Exploiting disorder for perfect focusing", *Nat Photon* **4**, 320 (2010). — p.35.
[66] S. M. Popoff, G. Lerosey, R. Carminati, M. Fink, A. C. Boccara, and S. Gigan, "Measuring the transmission matrix in optics: An approach to the study and control of light propagation in disordered media", *Phys. Rev. Lett.* **104**, 100601 (2010). — p.39 and 50.
[67] J. C. Dainty, *Laser speckle and related phenomena*, Springer-Verlag (1984). — p.42.
[68] T. Cizmar, M. Mazilu, and K. Dholakia, "In situ wavefront correction and its application to micromanipulation", *Nat Photon* **4**, 388 (2010). — p.42.
[69] E. Ozbay, "Plasmonics: Merging photonics and electronics at nanoscale dimensions", *Science* **311**, 189 (2006). — p.42 and 54.
[70] A. Polman, "APPLIED PHYSICS: plasmonics applied", *Science* **322**, 868 (2008). — p.42 and 54.
[71] J. A. Schuller, E. S. Barnard, W. Cai, Y. C. Jun, J. S. White, and M. L. Brongersma, "Plasmonics for extreme light concentration and manipulation", *Nat Mater* **9**, 193 (2010). — p.42 and 54.
[72] H. A. Atwater and A. Polman, "Plasmonics for improved photovoltaic devices", *Nat Mater* **9**, 205 (2010). — p.42.
[73] E. Altewischer, M. P. van Exter, and J. P. Woerdman, "Plasmon-assisted transmission of entangled photons", *Nature* **418**, 304 (2002). — p.42.
[74] A. V. Akimov, A. Mukherjee, C. L. Yu, D. E. Chang, A. S. Zibrov, P. R. Hemmer, H. Park, and M. D. Lukin, "Generation of single optical plasmons in metallic nanowires coupled to quantum dots", *Nature* **450**, 402 (2007). — p.42.
[75] N. Liu, L. Langguth, T. Weiss, J. Kastel, M. Fleischhauer, T. Pfau, and H. Giessen, "Plasmonic analogue of electromagnetically induced transparency at the drude damping limit", *Nat Mater* **8**, 758 (2009). — p.42.
[76] T. Ergin, N. Stenger, P. Brenner, J. B. Pendry, and M. Wegener, "Three-Dimensional invisibility cloak at optical wavelengths", *Science* **328**, 337 (2010). — p.42.
[77] N. Fang, H. Lee, C. Sun, and X. Zhang, "Sub-Diffraction-Limited optical imaging with a silver superlens", *Science* **308**, 534 (2005). — p.42 and 68.
[78] K. F. MacDonald, Z. L. Samson, M. I. Stockman, and N. I.

Zheludev, "Ultrafast active plasmonics", *Nat Photon* **3**, 55 (2009). — p.42.

[79] T. Utikal, M. I. Stockman, A. P. Heberle, M. Lippitz, and H. Giessen, "All-Optical control of the ultrafast dynamics of a hybrid plasmonic system", *Phys. Rev. Lett.* **104**, 113903 (2010). — p.42.

[80] V. V. Temnov, G. Armelles, U. Woggon, D. Guzatov, A. Cebollada, A. Garcia-Martin, J. Garcia-Martin, T. Thomay, A. Leitenstorfer, and R. Bratschitsch, "Active magneto-plasmonics in hybrid metal-ferromagnet structures", *Nat Photon* **4**, 107 (2010). — p.42.

[81] M. Durach, A. Rusina, M. I. Stockman, and K. Nelson, "Toward full spatiotemporal control on the nanoscale", *Nano Lett* **7**, 3145 (2007). — p.42.

[82] M. Aeschlimann, M. Bauer, D. Bayer, T. Brixner, F. J. G. de Abajo, W. Pfeiffer, M. Rohmer, C. Spindler, and F. Steeb, "Adaptive subwavelength control of nano-optical fields", *Nature* **446**, 301 (2007). — p.42 and 68.

[83] X. Li and M. I. Stockman, "Highly efficient spatiotemporal coherent control in nanoplasmonics on a nanometer-femtosecond scale by time reversal", *Phys. Rev. B* **77**, 195109 (2008). — p.42 and 68.

[84] G. Volpe, S. Cherukulappurath, R. J. Parramon, G. Molina-Terriza, and R. Quidant, "Controlling the optical near field of nanoantennas with spatial Phase-Shaped beams", *Nano Lett.* **9**, 3608 (2009). — p.42 and 68.

[85] F. J. Garcia-Vidal, L. Martin-Moreno, T. W. Ebbesen, and L. Kuipers, "Light passing through subwavelength apertures", *Rev. of Mod. Phys.* **82**, 729 (2010). — p.43 and 71.

[86] A. Sentenac and P. C. Chaumet, "Subdiffraction light focusing on a grating substrate", *Phys. Rev. Lett.* **101**, 013901 (2008). — p.43, 54, and 71.

[87] G. Bartal, G. Lerosey, and X. Zhang, "Subwavelength dynamic focusing in plasmonic nanostructures using time reversal", *Phys. Rev. B* **79**, 201103 (2009). — p.43, 54, 68, and 71.

[88] L. Aigouy, P. Lalanne, J. P. Hugonin, G. Julié, V. Mathet, and M. Mortier, "Near-field analysis of surface waves launched at nanoslit apertures", *Phys. Rev. Lett.* **98**, 153902 (2007). — p.43 and 71.

[89] F. Pincemin, A. Sentenac, and J. Greffct, "Near field scattered by a dielectric rod below a metallic surface", *JOSA A* **11**, 1117 (1994).

— p.43 and 71.

[90] P. Lalanne and J. P. Hugonin, "Interaction between optical nano-objects at metallo-dielectric interfaces", *Nat Phys* **2**, 551 (2006). — p.45.

[91] D. van Oosten, M. Spasenovic, and L. Kuipers, "Nanohole chains for directional and localized surface plasmon excitation", *Nano Lett* **10**, 286 (2010). — p.46 and 71.

[92] E. Devaux, T. W. Ebbesen, J. Weeber, and A. Dereux, "Launching and decoupling surface plasmons via micro-gratings", *Appl. Phys. Lett.* **83**, 4936 (2003). — p.46.

[93] I. Vellekoop and A. Mosk, "Phase control algorithms for focusing light through turbid media", *Opt. Commun.* **281**, 3071 (2008). — p.48 and 50.

[94] A. Derode, P. Roux, and M. Fink, "Robust acoustic time reversal with high-order multiple scattering", *Phys. Rev. Lett.* **75**, 4206 (1995). — p.50.

[95] P. J. Schuck, D. P. Fromm, A. Sundaramurthy, G. S. Kino, and W. E. Moerner, "Improving the mismatch between light and nanoscale objects with gold bowtie nanoantennas", *Phys. Rev. Lett.* **94**, 017402 (2005). — p.54.

[96] P. Mühlschlegel, H. J. Eisler, O. J. F. Martin, B. Hecht, and D. W. Pohl, "Resonant optical antennas", *Science* **308**, 1607 (2005). — p.54.

[97] L. Novotny and N. van Hulst, "Antennas for light", *Nat. Photon* **5**, 83 (2011). — p.54.

[98] T. Sndergaard, S. I. Bozhevolnyi, J. Beermann, S. M. Novikov, E. Devaux, and T. W. Ebbesen, "Resonant plasmon nanofocusing by closed tapered gaps", *Nano Lett.* **10**, 291 (2010). — p.54.

[99] J. R. Krenn, B. Lamprecht, H. Ditlbacher, G. Schider, M. Salerno, A. Leitner, and F. R. Aussenegg, "Nondiffraction-limited light transport by gold nanowires", *EPL (Europhys. Lett.)* **60**, 663 (2002). — p.54.

[100] E. Verhagen, M. Spasenović, A. Polman, and L. K. Kuipers, "Nanowire plasmon excitation by adiabatic mode transformation", *Phys. Rev. Lett.* **102**, 203904 (2009). — p.54.

[101] M. I. Benetou, B. C. Thomsen, P. Bayvel, W. Dickson, and A. V. Zayats, "Four-level polarization discriminator based on a surface plasmon polaritonic crystal", *Appl. Phys. Lett.* **98**, 111109 (2011).

— p.54.
[102] B. Stein, J. Laluet, E. Devaux, C. Genet, and T. W. Ebbesen, "Surface plasmon mode steering and negative refraction", *Phys. Rev. Lett.* **105**, 266804 (2010). — p.54.
[103] L. Feng, A. Mizrahi, S. Zamek, Z. Liu, V. Lomakin, and Y. Fainman, "Metamaterials for enhanced polarization conversion in plasmonic excitation", *ACS Nano* **5**, 5100 (2011). — p.54.
[104] G. Volpe, G. Molina-Terriza, and R. Quidant, "Deterministic subwavelength control of light confinement in nanostructures", *Phys. Rev. Lett.* **105**, 216802 (2010). — p.54 and 68.
[105] T. S. Kao, S. D. Jenkins, J. Ruostekoski, and N. I. Zheludev, "Coherent control of nanoscale light localization in metamaterial: Creating and positioning isolated subwavelength energy hot spots", *Phys. Rev. Lett.* **106**, 085501 (2011). — p.54 and 68.
[106] S. G. Rodrigo, O. Mahboub, A. Degiron, C. Genet, F. J. García-Vidal, L. Martín-Moreno, and T. W. Ebbesen, "Holes with very acute angles: a new paradigm of extraordinary optical transmission through strongly localized modes", *Opt. Express* **18**, 23691 (2010). — p.54.
[107] M. Ozaki, J. ichi Kato, and S. Kawata, "Surface-Plasmon holography with White-Light illumination", *Science* **332**, 218 (2011). — p.54.
[108] F. Wei and Z. Liu, "Plasmonic structured illumination microscopy", *Nano Lett.* **10**, 2531 (2010). — p.54 and 68.
[109] D. M. Koller, U. Hohenester, A. Hohenau, H. Ditlbacher, F. Reil, N. Galler, F. R. Aussenegg, A. Leitner, A. Trgler, and J. R. Krenn, "Superresolution moir mapping of particle plasmon modes", *Phys. Rev. Lett.* **104**, 143901 (2010). — p.54 and 68.
[110] A. Kravchenko, A. Shevchenko, V. Ovchinnikov, A. Priimagi, and M. Kaivola, "Optical interference lithography using azobenzene-functionalized polymers for micro- and nanopatterning of silicon", *Adv. Mater.* **23**, 4174 (2011). — p.54.
[111] B. Gjonaj, J. Aulbach, P. M. Johnson, A. P. Mosk, L. Kuipers., and A. Lagendijk, "Active spatial control of plasmonic fields", *Nat Photon* **5**, 360 (2011). — p.55 and 68.
[112] P. Zhang, S. Wang, Y. Liu, X. Yin, C. Lu, Z. Chen, and X. Zhang, "Plasmonic airy beams with dynamically controlled trajectories", *Opt. Lett.* **36**, 3191 (2011). — p.55 and 68.
[113] E. G. van Putten, I. M. Vellekoop, and A. P. Mosk, "Spatial amplitude and phase modulation using commercial twisted nematic

lcds", *Appl. Opt.* **47**, 2076 (2008). — p.56.

[114] D. S. Kim, S. C. Hohng, V. Malyarchuk, Y. C. Yoon, Y. H. Ahn, K. J. Yee, J. W. Park, J. Kim, Q. H. Park, and C. Lienau, "Microscopic origin of Surface-Plasmon radiation in plasmonic Band-Gap nanostructures", *Phys. Rev. Lett.* **91**, 143901 (2003). — p.61.

[115] A. Szameit, Y. Shechtman, E. Osherovich, E. Bullkich, P. Sidorenko, H. Dana, S. Steiner, E. B. Kley, S. Gazit, T. Cohen-Hyams, S. Shoham, M. Zibulevsky, I. Yavneh, Y. C. Eldar, O. Cohen, and M. Segev, "Sparsity-based single-shot sub-wavelength coherent diffractive imaging", *Nat Mater* **advance online publication** (2012). — p.68.

[116] E. T. F. Rogers, J. Lindberg, T. Roy, S. Savo, J. E. Chad, M. R. Dennis, and N. I. Zheludev, "A super-oscillatory lens optical microscope for subwavelength imaging", *Nat Mater* **advance online publication** (2012). — p.68.

[117] M. L. M. Balistreri, H. Gersen, J. P. Korterik, L. Kuipers, and N. F. van Hulst, "Tracking femtosecond laser pulses in space and time", *Science* **294**, 1080 (2001). — p.68.

[118] R. Hillenbrand, T. Taubner, and F. Keilmann, "Phonon-enhanced light-matter interaction at the nanometre scale", *Nature* **418**, 159 (2002). — p.68.

[119] E. BETZIG, J. K. TRAUTMAN, T. D. HARRIS, J. S. WEINER, and R. L. KOSTELAK, "Breaking the diffraction barrier: Optical microscopy on a nanometric scale", *Science* **251**, 1468 (1991). — p.68.

[120] S. W. Hell and J. Wichmann, "Breaking the diffraction resolution limit by stimulated emission: stimulated-emission-depletion fluorescence microscopy", *Opt. Lett.* **19**, 780 (1994). — p.68.

[121] M. Dyba and S. W. Hell, "Focal spots of size $\lambda/23$ open up far-field florescence microscopy at 33 nm axial resolution", *Phys. Rev. Lett.* **88**, 163901 (2002). — p.68.

[122] E. Betzig, G. H. Patterson, R. Sougrat, O. W. Lindwasser, S. Olenych, J. S. Bonifacino, M. W. Davidson, J. Lippincott-Schwartz, and H. F. Hess, "Imaging intracellular fluorescent proteins at nanometer resolution", *Science* **313**, 1642 (2006). — p.68.

[123] M. J. Rust, M. Bates, and X. Zhuang, "Sub-diffraction-limit imaging by stochastic optical reconstruction microscopy (STORM)", *Nat Meth* **3**, 793 (2006). — p.68.

[124] D. Axelrod, "Cell-substrate contacts illuminated by total internal

reflection fluorescence.", *J. Cell Biol.* **89**, 141 (1981). — p.68.

[125] T. Zentgraf, Y. Liu, M. H. Mikkelsen, J. Valentine, and X. Zhang, "Plasmonic Luneburg and Eaton lenses", *Nat Nano* **6**, 151 (2011). — p.68.

[126] B. Gjonaj, J. Aulbach, P. M. Johnson, A. P. Mosk, L. Kuipers, and A. Lagendijk, "Optical control of plasmonic bloch modes on periodic nanostructures", *Nano Lett.* **12**, 546 (2012). — p.70.

Overzicht (Nederlands)

Wat zijn Surface Plasmon Polaritons?
Surface Plasmon Polaritons zijn oppervlaktegolven die zich tussen een geleider (een metaal) en een isolator (een dilektrisch materiaal) bevinden. In een isolator zijn de elektronen sterk gebonden aan de atoomkern, waardoor de elektronen niet vrij kunnen bewegen door het materiaal. Een metaal, daarentegen, bevat elektronen die zich vrijuit kunnen bewegen. De gezamenlijke oscillaties van deze vrije elektronen worden plasmonen genoemd. De gezamenlijke oscillaties van de vrije elektronen die zich aan het oppervlak van het metaal bevinden, geeft een oppervlaktegolf: de Surface Plasmon. De intensiteit van deze golf neemt exponentieel af bij grotere afstanden van het oppervlak.

Een vergelijking kan gemaakt worden met een meer. Wanneer een blad in dit meer valt, zal er lokaal een golf gecreerd worden die zich over het oppervlak voortplant. Hier is het blad de bron van de verstoring die de golf creert. Wanneer de vrije elektronen "zee" in een metaal verstoord wordt, zal een ladingsdichtheidsgolf zich over het oppervlak (het vlak dat de isolator raakt) voortplanten. Deze verstoring van de elektronen kan gedaan worden met behulp van fotonen of elektronen.

Waarom zijn Surface Plasmon Polaritons belangrijk?
Met Surface Plasmon Polaritons is het mogelijk om elektromagnetische straling te focussen. De lengteschaal waarop een golf geconcentreerd kan worden is evenredig aan de golflengte. Hoe korter de golflengte, des te scherper de focus. Surface Plasmon Polaritons kunnen aangeslagen worden met behulp

van licht. De golflengte van een Surface Plasom is korter dan de golflengte van het licht dat gebruikt wordt om het aan te slaan. Dit betekent dat plasmonische focus beter is dan optische focus. De hogere concentratievermogen maakt Surface Plasmon Polaritons zeer geschikt voor microscopie.

Wat is Plasmonisch afbeelden of wat is een plasmonmicroscoop?
Wanneer een golf op een sample valt, zal het sample de golf reflecteren, absorberen of verstrooien. Deze golf die van het sample komt bevat allerlei informatie over het sample wat met behulp van een detector afgebeeld kan worden. Verschillende golven kunnen gebruikt worden voor verschillende afbeeldingstechnieken: Bijvoorbeeld, in radiografie wordt er gebruik gemaakt van Rntgengolven; in echografie wordt er gebruik gemaakt van ultrasone geluidsgolven; in optische microscopie wordt er gebruik gemaakt van lichtgolven; in elektronmicroscopie wordt er gebruik gemaakt van elektronengolven. De resolutie van de afbeeldingstechniek hangt af van de detectie van de verstrooide golf en de uiteindelijke resolutie wordt gegeven aan de hand van de golflengte van de te detecteren golf. In plasmonmicroscopie (als onderdeel van optische microscopie), wordt er gebruik gemaakt van plasmonische golven vanwege de kortere golflengten in vergelijking met licht.

Hoe kunnen de relatieve vertragingen voor het focusseren worden bepaald?
Het bepalen van het optische golffront dat vereist is om te kunnen focusseren, is het belangrijkste onderdeel van de plasmonische lens. Wij hebben gebruik gemaakt van twee methoden om het optische golffront te bepalen: (1) experimentele metingen en (2) theoretische berekeningen. In de experimentele methode worden alle mogelijke combinaties van vertragingen uitgeprobeerd en vervolgens wordt alleen die combinatie geselecteerd met de hoogste intensiteit in het gewenste focus. Deze methode kan op een slimme manier worden toegepast door gebruik te maken van een terugkoppelingsalgoritme dat de interferentie vanuit alle bronnen maximaliseert op het gewenste punt. Wanneer deze methode wordt toegepast hoeven geen aannames te worden gemaakt met betrekking tot de metallische nanostructuur. De theoretische berekening is alleen mogelijk wanneer de oppervlakteplasmonen propageren over een vlak metaaloppervlak. Als aan deze voorwaarde wordt voldaan dan wordt de benodigde vertraging voor elke bron eenvoudigweg bepaald door de afstand tussen de de bron en het gewenste focus.

Bovenstaande kunnen we ook intutief begrijpen. Wanneer bladeren in een meer vallen en er geen objecten zijn, zoals drijvende stukken hout, die de

propagatie van oppervlaktegolven verstoren, dan kunnen we ons voorstellen dat voor het focusseren op een bepaald punt de vertragingen alleen worden bepaald door de afstand tussen bron en focus. Als de golven daarentegen ook worden verstrooid door drijvende stukken hout, dan worden de vertragingen niet meer louter bepaald door de afstand tussen bron en focus. Er is dan een andere manier nodig om de optimale vertragingen te bepalen.

Aangezien we de metallische nanostructuur met elk gewenst patroon kunnen fabriceren, weten we van tevoren welke methode we dienen te gebruiken om de vertragingen te bepalen. Voor plasmonmicroscopie is een platte metallische film te verkiezen, omdat op een dergelijke structuur het focusseren op een snelle manier en met hoge resolutie plaats kan vinden.

Waarom zijn focusseren en scannen onmisbaar voor plasmonmicroscopie?
We hebben een plasmonische lens gemaakt die een kleiner focus kan maken dan een optische lens, omdat de plasmonische golflengte korter is dan de optische golflengte. Desalniettemin kan de plasmonische lens niet gebruikt worden als detectielens, omdat er geen plasmonische detectoren zijn: het uitlezen van een plasmonmicroscoop dient dan ook optisch te geschieden. Om een beeld te maken met plasmonische resolutie wordt het sample aangeslagen door het plasmonische focus. Wanneer we de oppervlakteplasmonen focusseren is het licht enkel afkomstig van een deel van het sample dat zo klein is als de grootte van het plasmonische focus. De totale intensiteit van het licht afkomstig van dit deel van het sample vormt n punt in het uiteindelijke beeld van de plasmonische microscoop (in overeenstemming met de positie van het plasmonische focus). Het aangrenzende punt wordt toegevoegd door plasmonen te focusseren op het aangrenzende deel van het sample en vervolgens wederom de totale intensiteit van het uitgaande licht afkomstig vanuit dit deel te meten. Door dus het plasmonische focus te scannen kunnen we een beeld construeren van een volledig sample waarbij de resolutie wordt bepaald door de grootte van het plasmonische focus.

Hoe goed doet de plasmonmicroscoop het?
Enkele van de belangrijkste eigenschappen van een microscoop zijn: 1. de resolutie, of het vermogen om nabij gelegen punten uit elkaar te halen, 2. het gezichtsveld, of het grooststo mogelijk object dat kan worden afgebeeld, en 3. de acquisitietijd of de tijd nodig om de afbeelding te maken. Wij hebben onze plasmonmicroscoop gebruikt om verstrooiers af te beelden die op een metallische nanostructuur zitten. De resolutie die wij bereiken met onze

plasmonmicroscoop is afhankelijk van de plasmonengolflengte en is $10-20\%$ beter dan bij conventionele microscopie. De resolutie toename komt door de kortere golflengte van een plasmon (in vergelijking met de golflengte van het inkomende licht). Het gezichtsveld en de acquisitietijd zijn omgekeerd evenredig ten opzichte van elkaar omdat we de afbeelding maken door te scannen: hoe verder je scant, hoe groter het gezichtsveld, maar ook hoe langer de acquisitietijd.

Kan de prestatie van de plasmonmicroscoop worden verbeterd?
Met de huidige microscoop hebben we met succes het principe van de plasmonmicroscoop aangetoond. De prestatie van de microscoop kan nog met een orde van grootte worden verbeterd. De resolutie kan worden verbeterd door betere nanostructuren te gebruiken: de golflengte van plasmonen dat experimenteel is vastgesteld voor de beste vlakke metalen nanostructuren is tien keer kleiner dan de golflengte van het inkomende licht, wat betekent dat het plasmonische brandpunt tien keer kleiner kan worden dan wat we nu bereiken. Het gezichtsveld kan worden verbeterd zonder de acquisitietijd te vergroten door parallele verwerking van meerdere plasmonische brandpunten, oftewel multiplexen. De acquisitietijd kan worden verbeterd door het gebruik van hoge snelheid ruimtelijke lichtmodulators waarmee er sneller gescand kan worden. De optimale prestatie van de plasmonmicroscoop wordt bereikt door de modernste ruimtelijke lichtmodulators te gebruiken in combinatie met een optimale nanostructuur in een multiplexe configuratie. Met deze goptimaliseerde plasmonmicroscoop kunnen we in de nabije toekomst bewegende beelden maken van objecten van een millimeter grootte met een resolutie van 50 nm.

Wie wordt de gebruiker van de plasmonmicroscoop?
Een plasmonmicroscoop maakt hoge resolutie afbeeldingen van een oppervlakte van een monster. Het oppervlak van de monster moet in contact staan met een metallische nanostructuur, dat tevens als plasmonische lens werkt. Voor biologen is het oppervlak van een cel waarschijnlijk het meest onderzochte deel van de cel. Alle uitwisselingen van materialen en informatie tussen de levende cel en de externe omgeving vindt plaats aan de celgrenslagen. Voor deze grote interessegebieden in de oppervlaktebiologie worden verscheidene optische microscopen gebruikt. Omdat onze plasmonmicroscoop betere afbeelding kan leveren van levende cellen zonder het gebruik van fluorescent labeling, denken wij dat biologen en artsen in hoge mate zullen profiteren van deze nieuwe vorm van microscopie.

Overview (English)

What are Surface Plasmon Polaritons?
Surface Plasmon Polaritons are surface waves at the interface between a conductor (metal) and an insulator (dielectric). In an insulator the electrons are strongly bound to the nuclei and they are not free to move around. In a metal, instead, the electrons are free to move around. The collective oscillations of the free electrons (the electron sea) are known as plasmons (bulk plasmons). The collective oscillation of only the free electrons adjacent to the surface of a metal give rise to a surface wave: the Surface Plasmon. Away from the surface, the intensity of this wave decreases exponentially with the distance from the surface.

Let us consider the unperturbed surface of a lake. When a leaf falls in the lake, it will locally generate a surface wave that propagates along the surface. In this intuitive picture the leaf is the source of the perturbation which creates the surface wave. Similarly, when the free electron sea of a metal is perturbed than a surface charge density wave is launched and propagates along the surface (the interface with the insulator). Typically the perturbation of the metallic electrons is done with photons or with electrons.

Why are Surface Plasmon Polaritons important?
Surface Plasmon Polaritons can tightly confine or focus electromagnetic energy. The length scale to which a wave can be focused is proportional to the wavelength. The shorter the wavelength the better the focusing. Surface Plasmons Polaritons can be excited via light. For a fixed light frequency, the wavelength of the excited Surface Plasmon is shorter than the wavelength

of the exciting light. Thus plasmonic confinement is better than optical confinement. One way to harvest the high confinement of Surface Plasmon Polaritons is by using these waves for imaging.

What is plasmonic imaging or a plasmonic microscope?
When a wave is incident on a sample, the wave is scattered, reflected or absorbed by the sample. The wave scattered (or reflected or absorbed) from the sample is recorded on a detector because it contains information regarding the sample and can be used to create an image of the sample. Different waves can be used for different imaging techniques: for example in radiography X-ray waves are used; in echography ultrasound waves are used; in optical microscopy light waves are used; in electron microscopy electron waves are used. The resolution of the imaging technique is determined by the way we detected the scattered wave and the ultimate resolution is given by the wavelength of the wave used to create the image. In plasmonic microscopy (part of optical microscopy) plasmonic waves are used because of their shorter wavelengths compared to light.

How does a plasmonic microscope work?
Surface Plasmons are surface waves propagating on a metallic surface and are excited from incident light. The sample to be imaged is placed on top of this metallic surface. Propagating Surface Plasmons are optically invisible (you cannot see them propagating), but when these waves encounter the sample plasmons are locally scattered by the sample into light emitted in all directions. This light scattered out of the metallic surface is recorded on an normal optical detector (a camera). The optical image recorded on the detector is the image of the sample which was excited by Surface plasmons. Because the image is created using light and standard lenses, the resolution does not depend on the plasmonic wavelength and is ultimately determined by the quality of the lens used and by the wavelength of detected light. Nevertheless, even by using the same light, the same lens and the same detection camera, there is a way to create an image of the sample which depends on the plasmonic wavelength (thus improved resolution): the plasmonic excitation of the sample has to be tightly focused. In other words, to improve the resolution, a plasmonic lens has to be used for focusing the plasmons and for scanting the focus.

How do you make a plasmonic lens?
Plasmonic lenses, as well as plasmonic sources and detectors are not avail-

able. The plasmonic lens is created by using synchronized light beams. We use many light beams to create as many plasmonic sources: this is similar with many leaves falling on the surface of the lake. The circular surface waves originating from every leave (source) will propagate and interfere with each other. If the leaves fall at the same exact time and next to each other in space to form a line, then the interference of the surface waves is a line wave similar to the ocean waves. If the leaves fall not all at the same time but each with a time delay, then the inference pattern of the surface waves can be tuned to create a focus at any desired location by controlling the relative time delays. The relative time delays are tuned so that at the exact desired locations all waves coming from each leave are in phase with each other and thus interfere constructively.

Similarly, we use many light beams incident on a metallic nanostructure to generate surface plasmon waves. The relative time delay of the light beams are tuned via a spatial light modulator. This pixelated device changes the phase (and the amplitude) of light passing through it. When light passing through this device impinges on the surface of the metallic structure it will originate many plasmonic circular waves, one for each pixel. The phase of the incident light (the incident wavefront) can be tuned to focus the plasmonic waves at any desired location on the metallic surface. This way a plasmonic lens is created which can focus Surface Plasmons and scan this focus.

How to determine the relative time delays for focusing?
Determining the required optical wavefront (the phase delays of the light beams) for focusing is the most important part of the plasmonic lens. We have used two methods to determine the optical wavefront: (1) experimental measurements and (2) theoretical calculations. The experimental method consist of trying all possible combinations of possible time delays and selecting among all these combination only the one which provides the largest intensity in the desired focal spot. This method can be applied in a smart way by using a feedback algorithm to maximize the resultant interference from all sources at the desired spot. In applying this experimental method no assumptions have to be made regarding the metallic nanostructure. The theoretical calculation is possible only when the Surface Plasmons propagate along a flat metallic surface (no corrugations). When this condition is satisfied then the time delay for each source is easily determined by the distance between the source and the desired focal point.

Intuitively when leaves fall in a lake and there is nothing to perturb the propagation of the surface waves (like floating wood), then it is predictable

that for focusing at a target the time delays are determined by the source-target distance. If the waves are also scattered by floating wood pieces, then the time delays are not determined by the source-target distance and another approach to determine the time delays has to be used.

Because we can fabricate the metallic nanostructure with any desired pattern, we know in advance which method to use for determining the time delays. For plasmonic microscopy, a flat metallic film is preferable because on such structure plasmonic focusing and scanning can be done faster and with high resolution.

Why are focusing and scanning needed for plasmonic microscopy? We have created the plasmonic lense which can create a smaller focus than an optical lens because the plasmonic wavelength is shorter than the optical wavelength. Nevertheless the plasmonic lens can not be used as a detection lens because there are no plasmonic detectors: the read out of the plasmonic microscope is optical (light detected). To create the image of the sample with plasmonic resolution the sample is excited by the plasmonic focus. When we focus Surface Plasmons on one point all the light comes only from a portion of the sample which is as small as the size of the plasmonic focus. The total intensity of the outgoing light from that portion of the sample constitutes one point of the final image of the plasmonic microscope(in correspondence of the position of the plasmonic focus). The adjacent point is added to the final image by: focusing plasmons to the adjacent spot to excite the adjacent portion of the sample and by integrating the intensity of the outgoing light from this new portion of the sample. Thus by scanning the plasmonic focus we can create an image of the entire sample and the resolution of this image is given by the size of the plasmonic focus.

What is the actual performance of the plasmon microscope? Some of the main characteristic of a microscope are: (1) the resolution or the ability to resolve nearby points, (2) the field-of-view or the largest size of the sample that can be imaged, and (3) the acquisition time or the time needed to create the image. We used our plasmonic microscope to image scatterers positioned on top of a metallic nanostructure. The actual imaging resolution achieved with our plasmonic microscope is dependent on the plasmonic wavelength and is $10 - 20\%$ better than conventional optical microscopy. This increase in resolution is due to a shorter plasmonic wavelength (as compared to the incident light wavelength). The field-of-view and the acquisition time are inversely proportional to each other because the image

is created via scanning: the further you scan the larger the field-of-view but also the longer the acquisition time.

Can the performance of the plasmon microscope be improved?
With the actual microscope we have successfully proved the principle of a plasmonic microscope. The performance of the microscope can be improved by nearly one order of magnitude. The resolution can be improved by using better nanostructures: the plasmonic wavelength experimentally reported for the best planar metal nanostructures is 10 times shorter than the wavelength of the incident light meaning that the plasmonic focus can be made 10 times smaller than the actual one. The field-of-view can be improved by without any increase in acquisition time via parallel processing of multiple plasmonic foci; thus multiplexing. The acquisition time can be improved by using high speed spatial light modulator devices for faster scanning.

The optimal performance of the plasmonic microscope is achieved by using the latest spatial light modulators in combination with an optimal nanostructure and a multiplexed configuration. With this optimized plasmonic microscope we can achieve in the near future video rate imaging of millimetric-size samples with a resolution of 50 nm.

Who is going to use the plasmon microscope?
A plasmonic microscope can provide high resolution imaging of the surface of a sample. The surface of the sample has to in contact with the metallic nanostructure which is also the plasmonic lens. For biologist the surface of a cell is probably the most investigated part of the cell. All the exchange of material and information between the living cell and the external environment happens at the cell boundaries. Due to this large interest in surface biology various optical microscopes have been used. Because our plasmonic microscope can provide better imaging of living cells without any fluorescent labeling, we think that biologist and medical doctors will largely benefit from this new microscopy.

Acknowledgments

This thesis is dedicated to my family: my younger sister Lorina, my mother Ardiana, and my father Marenglen Enrik. I will never stop thanking your continuous and sweet encouragement during my life.

First things first! I fought through this PhD as part of a team. Thank you Jochen, Patrick, Allard, Kobus and Ad. Gentlemen, it was a privilege fighting on your side. Hans, Gijs, Dimitri, what formidable weapons you crafted for me.

To the past and present members of Photon Scattering group: you bunch of marvelous individuals with unique personalities and shining minds. Thank you Bernard, Sanli, Paolo, Jochen, Patrick, Moma, Ramy, Ivert, Otto, Timmo, Ad and Rob. I cannot leave out the COPS people in Twente because we are the same group. Elbert, Merel, Alex, Bart, Willem, Simon, Ivo, Willem T., Jacopo, Georgios, Pepijn, Leon, Philip, Duygu, Rajesh, Darnang, Emre, Hasan, Bas, Elahe, Edwin, Frerik, Naser, Rob, Thomas, Cock, Marlon, and Hannie; I will remember you with great affection. The sailing trips in Friesland, among hundreds of other things, were very inspiring for me. Thank you for everything.

To the Center for Nanophothonics people: you are all doing great science and I deeply thank you for sharing your knowledge and your opinions with me and for teaching me how important communication is for science. To my colleagues at Amolf, thank you for the incredible working environment that surrounded me for 4 years, thank you for being always available, thank you

for all the support you gave in technical, scientific and personal challenges. With a smile I will remember our days together in the lovely green building.

To those who cheered my days in this Amsterdam expedition of mine, my friends: it was (and it will be) a lot of fun and joy. To Gianluca, Eralda, Teuta and Fabrice, the ones who took me by the hand in my first months and introduced me to spectacular places and people, I can only say that four years flew away pleasantly thanks to you. To Marko (aka Svetlana), Ivana (aka Boris), Jochen (aka Gertrude) and to Ronald (aka Your mother): with the things we have done together could be written a novel. To Katrin, Rajoy, Paolo, Gijs, Snezana, Magdalena, Felix, Idlir, Mathias, Anouk, Erka, Emi, Hege, Anne Willem and Davide: what an infinity of unforgettable memories we share. To all those friends that I cannot mention one-by-one: you completed me.

My final acknowledgments go to my supervisors: Ad you opened for me the doors of science, and led me through those doors with God-only-knows all the patience; Patrick, you put me into structure and showed me how to walk in science; Kobus, you taught me how various and metamorphic science can be. Thank you again!